

Scuola di Scienze
Dipartimento di Fisica e Astronomia
Corso di Laurea Magistrale in Fisica

Monte Carlo simulation of a neutron veto
for the XENONnT experiment

Relatore:

Prof.ssa Gabriella Sartorelli

Presentata da:

Maria Corasaniti

Correlatori:

Dott. Marco Selvi

Dott. Marco Garbini

Anno Accademico 2015/2016

Sommario

L'esperimento XENON1T, situato presso i Laboratori Nazionali del Gran Sasso, è attualmente il più grande esperimento dedicato alla ricerca diretta della materia oscura. Esso consiste di una Time Projection Chamber (TPC) contenente 2 t di xeno liquido ed ha completato la sua prima acquisizione dati nel gennaio 2017, ottenendo il miglior limite per sezioni d'urto WIMP-nucleone indipendenti dallo spin con un minimo di $7.7 \cdot 10^{-47} \text{ cm}^2$ per WIMP di massa $35\text{-GeV}/c^2$ al 90% di livello di confidenza. Attualmente l'esperimento è ancora in acquisizione dati ed ha come obiettivo una sensibilità pari a circa $1.6 \cdot 10^{-47} \text{ cm}^2$, per WIMP di massa $50 \text{ GeV}/c^2$, nell'esposizione totale di 2 t·y.

È già previsto dalla collaborazione il futuro upgrade dell'esperimento: XENONnT. Con una TPC più grande e un target di xeno maggiore (~ 6 t) si stima di poter migliorare la sensibilità di un altro ordine di grandezza. A tale scopo è fondamentale la riduzione di tutte le sorgenti di segnali di fondo. Il fondo atteso di neutroni per la nuova TPC è di ~ 5 eventi nel volume fiduciale di 4 t per un'esposizione nominale di 20 t · y. In questo lavoro presentiamo lo studio Monte Carlo di un veto di neutroni consistente di uno scintillatore liquido caricato con gadolinio per l'esperimento XENONnT, con l'obiettivo di taggare gli eventi di fondo prodotti da neutroni radiogenici. I risultati indicano che, per una miscela scintillante con 0.1% di gadolinio in peso e un'efficienza di collezione di luce di $\sim 7\%$, si ottiene una capacità di rigettare neutroni superiore all'80%. Ciò consente di ridurre il fondo di neutroni radiogenici di un fattore ~ 5 e di essere in pieno accordo con l'obiettivo dell'esperimento XENONnT: < 1 evento di fondo nell'esposizione totale.

Abstract

XENON1T, located at the Laboratori Nazionali del Gran Sasso, is currently the largest experiment for direct dark matter search. It consists of a dual phase TPC filled with 2 tonnes of xenon, and has completed the first science run in January 2017, obtaining the most stringent exclusion limits on the spin-independent WIMP- nucleon interaction cross section for WIMP masses above $10 \text{ GeV}/c^2$, with a minimum of $7.7 \cdot 10^{-47} \text{ cm}^2$ for $35\text{-GeV}/c^2$ WIMPs at 90% confidence level. Currently the experiment is still in data acquisition and aims at a sensitivity of $1.6 \cdot 10^{-47} \text{ cm}^2$ for WIMP masses of $50 \text{ GeV}/c^2$ in 2 t·y exposure.

A next generation detector, called XENONnT, is already foreseen by the collaboration. It will have a larger TPC with an increased xenon target ($\sim 6 \text{ t}$) which will improve the WIMP sensitivity by another order of magnitude. For this purpose, it also requires a very low background level. The expected neutron background for the new designed time projection chamber is ~ 5 events in the 4 t fiducial volume, in the nominal 20 ton-year exposure. In this work we present a Monte Carlo simulation study of a Gd-loaded liquid scintillator neutron veto for the XENONnT experiment, with the goal of tagging the background events from radiogenic neutrons. Results indicate that, for a scintillating mixture with 0.1% of gadolinium by weight, and a light collection efficiency of $\sim 7\%$, we obtain a neutron rejection factor higher than 80%. This allows to reduce the neutron background by a factor ~ 5 , in order to be in full agreement with the background goal of the XENONnT experiment: < 1 background event in the total exposure.

Contents

Sommario	ii
Abstract	iii
Introduction	1
1 The Dark Matter quest	3
1.1 Dark Matter evidences	4
1.1.1 Galaxy scale evidences	5
1.1.2 The Microlensing effect	6
1.1.3 Bullet Cluster	9
1.2 Cosmological scale evidences	10
1.3 Dark matter composition	12
1.3.1 Barionic Dark Matter	12
1.3.2 Non-barionic Dark Matter	13
1.3.3 The MOND Theory	13
1.4 Standard Model candidates	14
1.4.1 Relic Neutrinos	15
1.4.2 Axions	15
1.4.3 Weakly Interacting Massive Particles (WIMPs)	16
1.4.4 Neutralino	17
1.4.5 Sneutrino, Gravitino and Axino	19
1.4.6 Wimpzillas	19
1.4.7 Kaluza-Klein particle	20
1.5 Experiments searching for WIMPs	20
1.5.1 Direct detection experiments	21
DAMA/LIBRA	21
CoGeNT	22
EDELWEISS II	23
SuperCDMS	24
CRESST-CRESST II-CREST III	24
DarkSide	25
LUX	26
XENON	27

1.5.2	Indirect detection experiments	27
	General Antiparticle Spectrometer (GAPS)	27
	VERITAS	28
	Super-Kamiokande	29
	Large Area Telescope	30
	IceCube	30
	AMS-02	31
2	The XENON project	33
2.1	Detection principle of a dual phase TPC	34
2.1.1	Liquid xenon as target	34
2.1.2	Xenon scintillation light	34
2.1.3	Signals produced in the TPC	35
2.1.4	Discrimination of ER and NR	37
2.2	The XENON experiments	38
2.2.1	XENON10	38
2.2.2	XENON100	39
2.2.3	XENON1T	40
	2.2.3.1 The background	43
	2.2.3.2 Internal background	43
	2.2.3.3 Intrinsic background	43
	2.2.3.4 External background	44
3	Description of the Monte Carlo Simulation	47
3.1	The GEANT4 framework	48
3.2	XENONnT TPC geometry	51
	3.2.1 Event selection in the TPC	51
	3.2.2 Radiogenic Neutron background	52
3.3	Neutron Veto conceptual design	55
	3.3.1 Detector configurations	55
	3.3.2 Gadolinium-loaded liquid scintillator	57
	3.3.3 Gadolinium neutron-capture in GEANT4	59
3.4	Photomultiplier System	60
	3.4.1 Photomultiplier Tubes and reflective foil	62
	3.4.2 Optical photon simulation	62
4	Analysis and Results	65
4.1	Neutron thermalization and capture	65
	4.1.1 Energy spectra in LS	66
	4.1.2 Time and spatial distribution of neutron captures	67
4.2	Light Collection Efficiency	69
4.3	Veto system performance	72
	4.3.1 Photoelectron Yield	76
4.4	Neutron veto efficiency	77
4.5	NR Background prediction for XENONnT	80
	Conclusions	81

Bibliography

A mio nonno, Gerardo.

Introduction

The Dark Matter (DM) quest is today one of the most challenging and intriguing open questions in physics. During the last century, early as the measurements of unexpected rotational velocities of the Coma galaxy cluster, we became aware that with the known physics we are able to explain only a minimum part of the whole Universe composition. Nowadays, the scientific community agrees that the ordinary matter can not account for the total mass content of the Universe. Starting from this open question, remarkable efforts have been directed towards the search for the so-called Dark Matter (DM). Indeed the number of experiments aimed at detecting Dark Matter has continuously grown in the last decades. One interesting and promising candidate is the so-called **WIMP** (**W**eakly **I**nteraction **M**assive **P**article), a new particle interacting with ordinary matter only through gravitation and weak interaction.

In Chapter 1, we review the status of the search for Dark Matter, along with the present state-of-art of experimental and theoretical achievements. We describe the astrophysical evidences, from both galactic and cosmological scales, which led to the belief in the Dark Matter existence. The composition of Dark Matter is still quite uncertain, even though there are strong indications for DM to be non-baryonic; several candidate particles have been proposed within different theoretical frameworks: Standard Model (SM) and theories beyond SM, such as SUSY and Extra dimensions. The experimental research follows basically two detection techniques: direct and indirect. The former aims at detecting scatterings of Dark Matter particles off target nuclei, while the indirect strategy relies on searching DM annihilation products. We provide a general overview of the current Dark Matter experiments and of their main results.

Chapter 2 is dedicated to the experiments of the XENON project. The current experiment is XENON1T, in operation at the Laboratori Nazionali del Gran Sasso (LNGS). It is a dual phase Time Projection Chamber (TPC) filled with ultra-pure xenon in liquid phase (LXe), with a small gap of gaseous xenon (GXe) on the top of the TPC. Xenon is an excellent scintillator medium, ideal to detect rare scattering events; the scintillation light is collected by two arrays of Photo Multiplier Tubes (PMTs) placed at the top and

bottom of the TPC. The interactions of particles in xenon produce also ionization; by applying an electric field the electrons can be drifted towards the gas region on the top, and here be extracted and accelerated to produce a second signal through proportional scintillation. This kind of technology has been demonstrated to be the most powerful in the direct search for Dark Matter. The interaction of DM with ordinary matter is characterized by a very small cross section; hence an extremely low background level is mandatory as well as a large target mass. The XENON1T experiment has been designed to fulfill both these two requirements.

Recently, the collaboration has published the results of the first dark matter search of 34 days, obtaining the most stringent exclusion limits on the spin-independent WIMP-nucleon interaction cross section for WIMP masses above $10 \text{ GeV}/c^2$. Currently the experiment is still in data acquisition and aims at a sensitivity to spin-independent WIMP-nucleon cross sections of $1.6 \cdot 10^{-47} \text{ cm}^2$ for WIMP masses of $50 \text{ GeV}/c^2$, in 2 t.y. To further improve the sensitivity by an order of magnitude, an upgrade towards the next phase experiment, called XENONnT is already planned.

In the context of this upgrade, the Monte Carlo prediction of nuclear recoil (NR) backgrounds showed that the radiogenic NR background in XENONnT is no longer negligible of five events in the total 20 t.y exposure. In this thesis we present the conceptual design and simulations of a liquid scintillator (LS) neutron veto for the XENONnT experiment, with the goal of tagging the background events from radiogenic neutrons.

Chapter 3 is devoted to the description of the study performed to design the neutron veto system. A detailed Monte Carlo simulation was set up in order to optimize the working configuration. In the first section we introduce the XENONnT TPC, and the simulations of the contamination of the components contributing to the radiogenic NR background in XENONnT. Then a set of different geometrical configuration of the veto are presented along with an overview on the operational principle and the most relevant physical properties of the organic LS. In the last section we introduce possible arrangements of the PMTs, used to collect the scintillation light.

The results from these simulations are presented in Chapter 4. After a dedicated characterization of the main properties of the implemented neutron veto, the light collection efficiency (LCE) and the photoelectrons (PEs) yield of the LS are studied. The tagging efficiency of the neutron veto, expressed as number of detected events above threshold, is then estimated. Finally, the NR background expected in XENONnT is obtained, with and without the neutron veto, in the various configurations under study.

The results achieved in this work are gathered in the conclusive chapter and discussed in the context of the whole scenario of direct Dark Matter search.

Chapter 1

The Dark Matter quest

Dark matter is hypothesised to be an unidentified type of matter, representing, in the observable universe, approximately the 27% of the mass and energy that is not accounted for by dark energy, baryonic matter (ordinary matter), and neutrinos. The name refers to the fact that it doesn't emit or interact with electromagnetic radiation, such as light, and is thus invisible to the entire electromagnetic spectrum.

Although Dark Matter has not been directly observed, first evidences for the Dark Matter (DM) existence came from F. Zwicky observations of the Coma and Virgo clusters. He found that the velocity of the galaxies was about one order of magnitude higher than the expected one, as if there were non luminous mass acting on the gravitational field. Many hypotheses have been formulated about DM properties. Currently it seems that the most viable candidates for this kind of matter rise from extensions of the Standard Model (SM). Such candidates are grouped under the common name of Weakly Interacting Massive Particles (WIMPs) that already introduces some of their characteristics. Indeed, such matter has to have only gravitational and weak interactions, thus being 'Weakly Interacting', and it has to be massive, thus being made of "Massive Particles". The most quoted candidate as WIMP comes from Supersymmetry: the neutralino. Several experiments have been realized in the last years aiming at the discovery of the Dark Matter. They are based on two different techniques: direct (interaction of the WIMP with ordinary matter) and indirect detection (measurement of the products of the annihilation of two WIMPs), both allowing to search and test different values for the theoretical parameters which define the DM properties.



FIGURE 1.1: The Coma Cluster, which provided the first evidence for Dark Matter. This image combines data from the Spitzer Space Telescope with the Sloan Digital Sky Survey to show many of the thousands of galaxies in the Coma cluster.

1.1 Dark Matter evidences

During his studies on the Coma Cluster [1], Fig. 1.1, Zwicky faced gravitational problems while he was trying to measure the mass of the cluster. A cluster is a set of galaxies that move together inside their own gravitational field. The dynamics of such objects is very complex and usually there is not a real center around which the galaxies move. In order to measure the mass of the Coma cluster, Zwicky first determined the galaxy velocities inside it, by measuring the Doppler effect of their spectra. After that, using the Virial Theorem, he was able to extract the gravitational force acting on each one of them and, finally, to obtain the mass of the system. Then, he measured the total light output of the cluster to determine the light to mass ratio. Comparing this value to the one from the nearby Kapteyn stellar system, he found a value for the Coma cluster that was 100 times lower compared to a single Kapteyn star.

Since Zwicky's results, other experimental observations showed a discrepancy with respect to what expected from a universe without the Dark Matter:

- anomalies in the rotational curves of spiral galaxies;
- observations of the Bullet Cluster;
- gravitational lensing effects;
- anisotropies in the Cosmological Microwave Background (CMB);

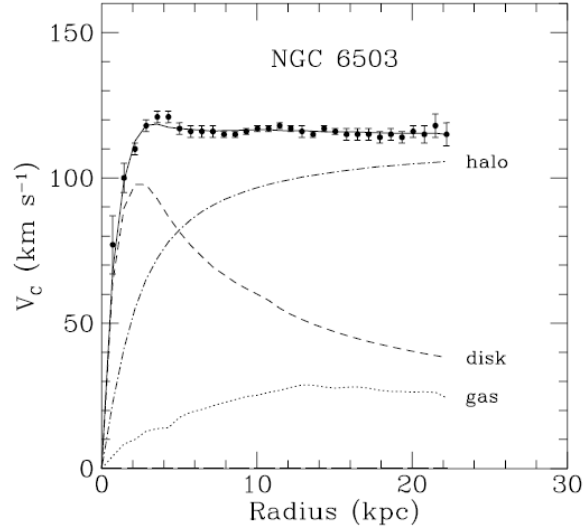


FIGURE 1.2: Velocity distribution of the dwarf spiral galaxy NGC 6503 [2], located in the region of space called the Local Void. The black dots are the observation results, while the dashed line is the expected shape from the only disk contribution. The contribution from the galaxy gas (dotted line) and halo (dash-dotted line) are also reported.

1.1.1 Galaxy scale evidences

Spiral galaxies, such as the Milky Way, are excellent probes to test the DM hypothesis. Such systems are said rotationally sustained since, for them, it is possible to define a clear rotational motion. To measure the velocity distribution until the edge of a galaxy, different techniques can be used depending on the used probe; for instance, the velocity of the hydrogen clouds is evaluated by measurements of the 21 cm line of the neutral hydrogen (HI), exploiting its low level of absorption in the interstellar medium. Usually, spiral galaxies are considered as made of a central core (disk+bulge), which is supposed to contain almost all the galaxy mass, and of an outer region. Their motion is described as a rigid body, hence, following the Newtonian gravitational law, the velocity distribution is given by

$$\frac{v^2(r)}{r} = G \frac{M(r)}{r^2} \quad \rightarrow \quad v(r) = \sqrt{G \frac{M(r)}{r}} \quad (1.1)$$

The mass can be obtained integrating the density in the sphere centered in the the center of the galaxy and of radius r

$$M(r) = 4\pi \int_0^r \rho(x) x^2 dx \quad (1.2)$$

where $\rho(x)$ is the density of visible matter in the galaxy. If we consider the mass as a function of the radius, $M(r)$, to be constant outside the core of the galaxy, we have

$$v(r) \propto \frac{1}{\sqrt{r}} \quad (1.3)$$

as predicted by the Newtonian theory. However, experimental data show that, outside the disk and much beyond, the velocity distribution no longer follows the expected behavior, but it remains constant (see Fig. 1.2). Such evidence points out the presence of matter (physical entity gravitationally interacting) characterized by a density that scales with the root square of the distance: $\rho \propto r^{1/2}$.

Such result is explained assuming that the spiral galaxies are enclosed in dark halos with a matter distribution that expands much beyond the distribution of the luminous matter and whose effect dominates in the outer region of the galaxies. One of the most popular density profile for the Dark Matter halos is the Navarro-Franck-White (NFW) profile :

$$\rho(r) = \frac{\rho_s}{(r/r_s)(1 + r/r_s)^2}, \quad (1.4)$$

where r_s is the halo scale radius and ρ_s is the characteristic density.

1.1.2 The Microlensing effect

Several studies on the Dark Matter abundance and composition have been based on the microlensing effect. Generally speaking, the lensing effect can take place whenever between a distant observed object and the observer there is a source of gravitational field (such as stars, galaxy clusters, etc.) intense enough to bend the light along the path from the source to the observer. According to the theory of general relativity, postulated by A. Einstein in 1915, the light is expected to follow exclusively the geodesics in curved spacetime. The matter distribution modifies the metric and consequently the path followed by the light varies in proximity of a mass. The mass which generates the gravitational field represents 'the lens'. As a result of the lensing effect, the observer can see multiple images or a distorted image of a unique source.

The microlensing effect was used to test the hypothesis that the DM was made of the so called Massive Compact Halo Objects (MACHOs) i.e. astronomical bodies, as brown dwarfs or black holes. Experiments for MACHOs' detection are based on the *gravitational microlensing* technique: if a MACHO interpones between the star and the observer, the star can be seen as brighter for a limited amount of time, from few days to few months for bigger bodies. Such an effect is observed for lenses with small masses ($10^{-6} \leq M/M_\odot \leq 10^6$) in systems that extent on the Kpc scale.

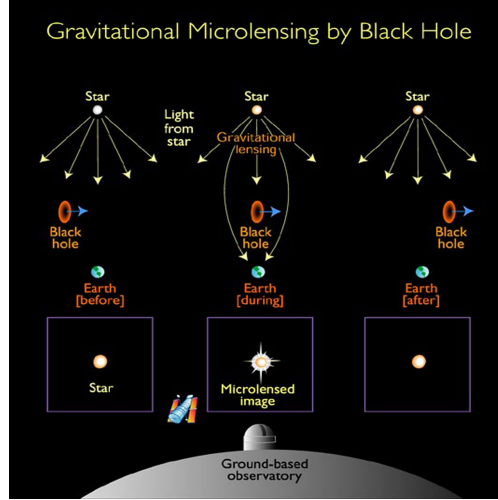


FIGURE 1.3: Illustration of the *microlensing* effect, i.e. the magnification of a light source due to astrophysical bodies acting as gravitational lens.

Unlike the Strong Lensing, where multiple images of the source are observed, in the microlensing what is observed is a time modulation of the luminosity curve of the source due to the relative motion between it and the lens (an illustration is given in Fig. 1.3). Hence, the observed luminosity is

$$\tau = \frac{1}{\delta\Omega} \int dV \cdot n(D_L) \cdot \pi \cdot \theta_E^2, \quad (1.5)$$

where $\delta\Omega$ is the observation solid angle, $n(D_L)$ is the micro-lens density as function of the lens distance D_L and $\pi\theta_E^2$ is the micro-lens cross section, $\theta_E = \sqrt{\frac{4GM}{c^2} \frac{D_LS}{D_LD_S}}$ is the so-called Einstein radius, where D_S is the distance of the source. Assuming a flat space-time and constant density along the line of sight, we have

$$\tau \approx \frac{2\pi}{3} \frac{G\rho}{c^2} D_S^2, \quad (1.6)$$

where D_S is the source distance. For a galaxy like the Milky Way one finds

$$v^2 \approx \frac{GM_g}{r} \rightarrow M_g = \frac{rv^2}{G} \quad (1.7)$$

and

$$\rho \approx \frac{3M_g}{4\pi r^3} \approx \frac{3}{4\pi G} \left(\frac{v}{r}\right)^2. \quad (1.8)$$

Thus, the optical depth is given by

$$\tau \approx \frac{1}{2} \left(\frac{v}{r}\right)^2. \quad (1.9)$$

For the Milky Way $\tau \approx 10^{-6}$. This means that roughly one out of a million stars in the

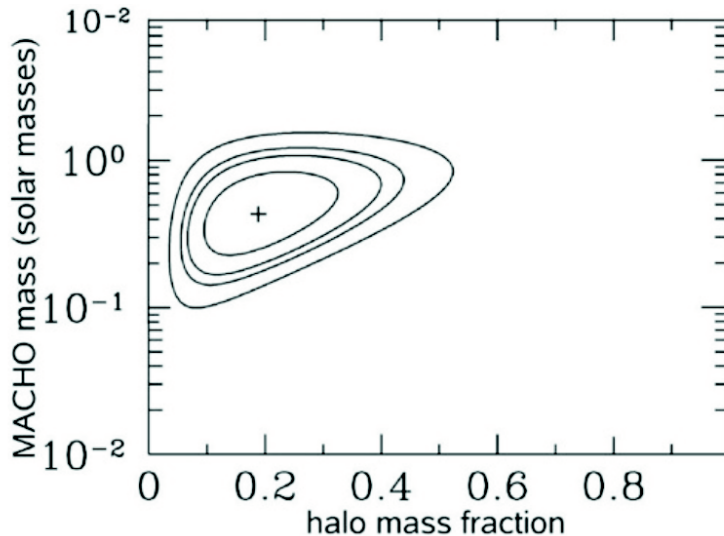


FIGURE 1.4: Likelihood contours obtained from the MACHO experiment [3]. The abscissa is the fraction of the halo mass contained in MACHOs, the ordinate is the MACHO mass. The contours shown correspond to the 60%, 90%, 95% and 99% confidence level.

nearby galaxies would be lensed. In this way, counting the micro-lenses in a particular direction it is possible to characterize the lens population. The possibility of detect such events depends on their duration (the Einstein crossing time). This is determined by the transverse velocity v_{\perp} and by the lens mass. For micro-lenses in the halo of the galaxy ($D_L \sim 10$ kpc) with velocity ~ 200 km/s, one has

$$t_E \approx 6 \cdot 10^6 \text{ s} \left(\frac{M}{M_{\odot}} \right)^{0.5} \approx 0.2 \text{ yr} \left(\frac{M}{M_{\odot}} \right)^{0.5} \quad (1.10)$$

If all events had the same time scale, then the number of expected events, N , in the monitoring time Δt is:

$$N = \frac{2}{\pi} n \tau \frac{\Delta t}{t_E}, \quad (1.11)$$

where n is the total number of considered sources.

Several research groups worked on the identification of lenses in the Milky Way's halo looking at sources in the Large and Small Magellanic Clouds (LMC and SMC). After the analysis of data collected during several years [3], few microlensing events were observed, leading to the conclusion that MACHOs can account only for less than 20% of the halo mass (Fig. 1.4).

New observation campaigns are currently ongoing aiming at the observation of microlensing events in the M31 galaxy (Andromeda galaxy). Due to its larger distance compared to the L/SMC galaxies, it is not possible to distinguish single stars and this drastically changes the observation strategy. In this case, the total luminosity of the



FIGURE 1.5: Image of the M31 galaxy.

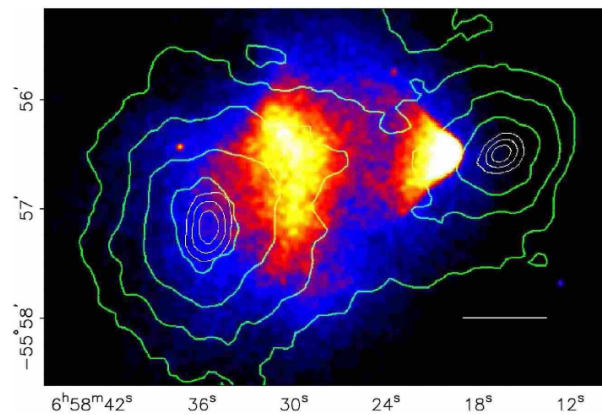


FIGURE 1.6: X-Ray image of the Bullet Cluster. The mass distribution from weak lensing measurements (green lines) is shown together with the baryonic matter distribution (red points). The Dark Matter distribution is drawn as the blue region.

galaxy should change and, consequently, only high magnification events gives appreciable signal. There are several advantages in looking at M31: due to its inclination along the line of sight (see Fig. 1.5), it is possible to accurately measure its rotation curve. Moreover, the lensing effects show an asymmetry that is not possible to explain only with the stars self-lensing.

1.1.3 Bullet Cluster

Other strong evidences for the DM existence come from the study of the Bullet Cluster (1E0657-558)[4]. It is defined as the collision of two clusters of galaxies (Fig. 1.6). Strictly speaking, the name Bullet Cluster refers to the smaller subcluster, moving away from the larger one. Both clusters have a stellar and gaseous component that interacts in different ways: the stellar component is slowed down by the gravitational field of the other cluster while the two gaseous components behave as a fluid. The gas interactions result in a X-ray emission that can be measured and used to trace the baryonic matter distribution.

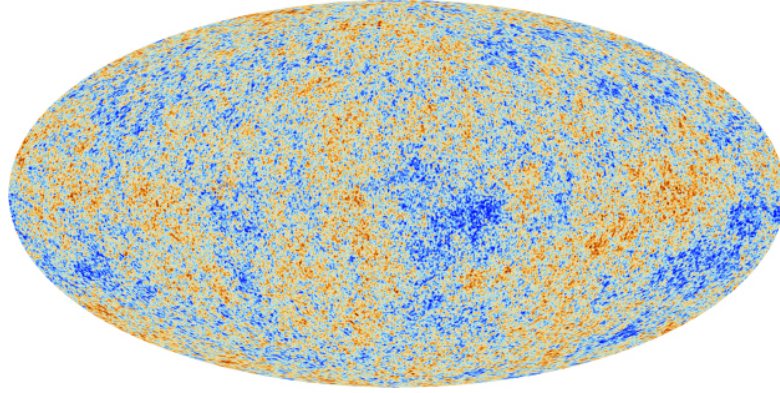


FIGURE 1.7: The anisotropies of the Cosmic Microwave Background (CMB) as observed by Planck. The CMB is a snapshot of the oldest light in our Universe, imprinted on the sky when the Universe was just 380 000 years old. It shows tiny temperature fluctuations that correspond to regions of slightly different densities, representing the seeds of all future structure: the stars and galaxies of today [6].

Experimental measurements show up a discrepancy between the baryonic matter distribution, measured from the X-ray emission (red points in Fig. 1.6), and the gravitational field distribution obtained from lensing measurements (green lines). The blue points in Fig. 1.6 represent the hypothetical Dark Matter distribution. It is based on its characteristics of weak interaction, which let DM particles pass through each other without being disturbed along their path. Conversely, this is not the case for the hot gas and stellar component. As the Dark Matter can continue to move on its trajectory, it is placed in the outer region of the Bullet Cluster.

1.2 Cosmological scale evidences

The lensing studies showed that, even if the Dark Matter exists, it is mainly composed by *non-baryonic* matter. Further convincing experimental evidences that sustain such a scenario come from the *Cosmic Microwave Background* (CMB) power spectrum analysis, but also from the Big Bang Nucleosynthesis (BBN).

The Cosmic Microwave Background, discovered by Arno Penzias and Robert Wilson in 1964 [5], provides important hints about the Dark Matter existence, composition and, in particular, about its abundance in the Universe. The CMB consists of relic photons from the early Universe stage at which the temperature dropped to about 3000 K, allowing electrons to recombine with protons. Hence, the Universe became transparent to the photons as they had not enough energy to ionize the hydrogen. The CMB almost perfectly follows an ideal black body spectrum with a temperature of $T = 2.726$ K. However, it shows temperature anisotropies (Fig. 1.7), at a level lower than 10^{-5} , that can give crucial information on the Universe composition.

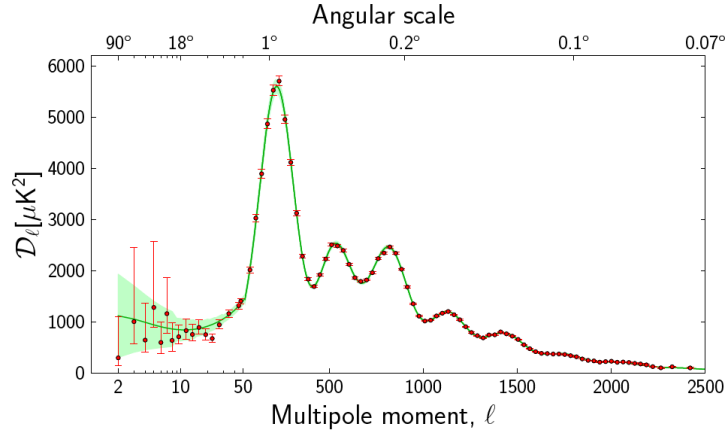


FIGURE 1.8: The 2013 Planck CMB temperature angular power spectrum [6]. The error bars include cosmic variance, whose magnitude is indicated by the green shaded area around the best fit model.

The CMB spectrum is characterized by a peak structure, shown in Fig. 1.8, as a consequence of two opposite effects: the gravitational force attracted the photons into the higher density regions, while the gas pressure pushed them apart. The angular power spectrum is obtained by decomposing the anisotropy map into spherical harmonics and taking into consideration various distortions such as emissions from galaxies. These anisotropies can be described as

$$\frac{\delta T}{T}(\theta, \phi) = \frac{T(\theta, \phi) - \langle T(\theta, \phi) \rangle}{\langle T(\theta, \phi) \rangle} = \sum_{l=2}^{+\infty} \sum_{m=-l}^{+l} a_{lm} Y_{lm}(\theta, \phi), \quad (1.12)$$

where $Y_{lm}(\theta, \phi)$ are the spherical harmonics.

The size and the position of the peaks of the CMB spectrum provide valuable information on cosmological parameters, such as the curvature and the energy-matter composition of the universe: Ω_{tot} , Ω_b and Ω_{DM} . From the CMB study [7, 8] it is then possible to extract an estimate of the non-baryonic Dark Matter abundance in the Universe:

$$\begin{aligned} \Omega_{\Lambda} &= 0.707 \pm 0.010; \\ \Omega_m &= 0.293_{\pm 0.010}^{+0.056}; \\ \Omega_b h^2 &= 0.02211 \pm 0.00034; \\ \Omega_{DM} h^2 &= 0.1162 \pm 0.0020. \end{aligned}$$

From the values of cosmological parameters results that the dark energy, Λ , accounts for about 70% of the Universe energy content, while the majority of the matter content is in the form of non-baryonic Dark Matter (see Fig. 1.9).

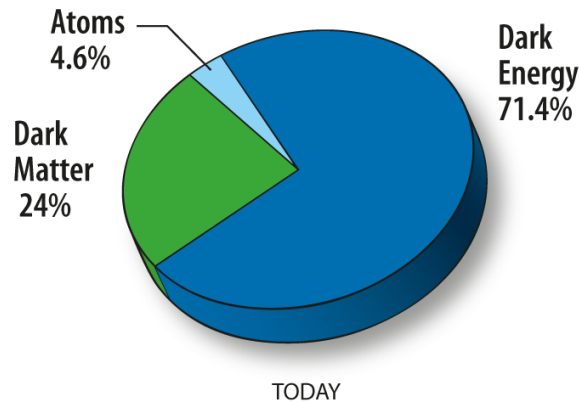


FIGURE 1.9: Representation of the contributions to the overall Universe content.

1.3 Dark matter composition

The Dark Matter identification is an open question still widely debated. There is a great variety of hypothesized DM candidates, none of them has been proved without a doubt, but one of the most studied is the WIMP. Nevertheless, it is worth recalling some of the main DM candidates that have been proposed to date. The Dark Matter can be divided in **barionic** Dark Matter and **non barionic**. The barionic Dark Matter is found in MACHOs (Massive astrophysical compact halo object), bodies that emits little or no radiation and drifts through interstellar space unassociated with any planetary system. The non-barionic Dark Matter instead is divided into Hot Dark Matter (*HDM*) and Cold Dark Matter (*CDM*), respectively composed by particles in relativistic motus or not and they represent a residual of the matter-radiation decoupling.

1.3.1 Barionic Dark Matter

The main characteristic of Dark Matter is the undetectability through direct observation. Since MACHOs are not luminous, they are hard to detect. MACHOs include black holes or neutron stars as well as brown dwarfs. This scenario predicts a diffuse γ -ray emission from the Milky Way's dark halo. A flux, whose properties are in a quite good agreement with the theoretical prediction, has been observed by the EGRET detector [9] mounted onto the CGRO satellite. Nonetheless, from microlensing studies and cosmological observations, we know that the majority of the Dark Matter is non-baryonic and MACHOs can account for not more than 20% of the total Dark Matter amount. The experiment EROS (*Experience pour la Recherche d'Objets Sombres*) at La Silla (Cile) observed for a time window of 5 years, about 30 million of stars belonging to the Magellanic Clouds individuating 8 possible MACHO. The data confirm a fraction of barionic Dark Matter, but, as already mentioned, not sufficient to explain totally the Dark Matter amount.

1.3.2 Non-barionic Dark Matter

About the non barionic Dark Matter there are two possible scenarios. The first one was hypothesized by Zeldovich, and it is named Hot Dark Matter, where the Dark Matter particles are relativistic. It implies a top-down structure formation history of the Universe where the big structures, such as galaxies, came first. However, the evolution of such systems were too slow if compared with the time scale of the primordial galaxy formation. Moreover, the high energy of the DM particles was in contrast with the formation of such big structures since relativistic particles would be dispersed in the space. The second scenario, which is also accepted and supported, is called Cold Dark Matter (CDM), in which Dark Matter is not relativistic. First evidences for the CDM came from the N-body simulations by Jeremiah Ostriker and James Peebles [10], in the 1970s. They simulated the interactions of a distribution of mass points, that represented stars moving in a galaxy, rotating around a central point. To get the correct interactions between the mass points, they used the Newton's law. They found that, in a time less than an orbital period, most of the mass points would have collapsed to a bar-shaped dense concentration, close to the center of the galaxy, with only few mass points at larger radii. This result is clearly in contrast with the elegant spiral or elliptical shape of the galaxies that we observe. But when they added a static and uniform distribution of mass, from 3 to 10 times the size of the total mass of the mass points, they found more recognizable structures. Thus, Ostriker and Peebles had solid numerical evidence that cold Dark Matter was necessary to form the types of galaxies we observe in the Universe.

In the following sections we outline the main proposals for CDM candidates arose so far. Candidate particles have been hypothesized in different theoretical frameworks, starting from the Standard Model but also in the Supersimmetry (SUSY) and in the Extra dimensions models context.

The present work will mainly concentrate on the WIMP Dark Matter candidate and its possible nature.

1.3.3 The MOND Theory

Before describing the possible WIMP candidate, there is also an alternative theory that must be mentioned. The MOND (*MOdified Newtonian Dynamics*) theory was proposed in 1981 by the israelian physicist Mordehai Milgrom. The theory's original motivation was to explain the fact that the velocities of stars in galaxies were observed to be larger than expected based on Newtonian mechanics. Milgrom noted that this discrepancy could be resolved if the gravitational force, experienced by a star in the outer regions

of a galaxy, was proportional to the square of its centripetal acceleration (as opposed to the centripetal acceleration itself, as in Newton's Second Law), or alternatively if gravitational force came to vary inversely with radius (as opposed to the inverse square of the radius, as in Newton's Law of Gravity). In MOND, violation of Newton's Laws occurs at extremely small accelerations, characteristic of galaxies yet far below anything typically encountered in the Solar System or on Earth. The Newton's second Law, modified according to the MOND theory, becomes:

$$F = ma\mu\left(\frac{a}{a_0}\right) \quad (1.13)$$

where for values of the acceleration not big it is possible to approximate as follow

$$\mu\left(\frac{a}{a_0}\right) \simeq \frac{a}{a_0}. \quad (1.14)$$

where a_0 is a constant and has a numerical value of 10^{-10}m/s^2 and $\mu(x) = 1$ if $|x| \gg 1$ and $\mu(x) = x$ if $|x| \ll 1$.

Using the Newton's law modified and the classical gravitational law it is possible to determine the acceleration acquired by stars as a function of the distance from the center of the galaxy. From this relation, is it possible to determine the evolution of the velocity for bigger distances (smaller accelerations):

$$\frac{GM}{r^2} = \frac{a^2}{a_0} \quad \rightarrow \quad a = \frac{\sqrt{GM}}{r} \quad \rightarrow \quad v = (GMa_0)^{1/4}.$$

The constant trend of the velocity corresponds thus to the what observed, and for this reason the MOND theory represent an alternative to the explanation of the rotational velocity trend of galaxies. This theory results unefficient in the attempt to explain phenomena such as the bullet cluster or the gravitational lensing, but it was the first competitive theory with the Dark Matter one.

1.4 Standard Model candidates

The Standard Model (SM) of particles offers some viable candidates in the framework of the HDM, while no SM particles seem to be able to account for the larger part of cold Dark Matter.

1.4.1 Relic Neutrinos

The cosmic neutrino background ($C\nu B$) is the Universe's background particle radiation composed of neutrinos, which are known as relic neutrinos. Like the cosmic microwave background radiation (CMB), the $C\nu B$ is a relic of the big bang; while the (CMB) dates from when the universe was $\sim 379 \cdot 10^3$ years old, the $C\nu B$ decoupled from matter when the universe was one second old. It is estimated that today, the $C\nu B$ has a temperature of roughly 1.95 K. Since low-energy neutrinos interact only very weakly with matter, they are notoriously difficult to detect, and the $C\nu B$ might never be observed directly. There is, however, compelling indirect evidence for its existence.

From the cosmology, we have that their relic density, under the hypothesis of massive and non relativistic neutrinos, is given by

$$\Omega_\nu h^2 = \sum_i^3 \frac{m_i}{93 \text{ eV}} \quad (1.15)$$

where h is the Hubble constant in units of 100 km/s/Mpc, the number 3 accounts for the neutrino's flavours and m_i is the mass of the i -th neutrino. Neutrinos as the main source of Dark Matter are experimentally excluded. The most stringent constraints on their masses come from the combination of PLANCK data with large scale structure information

$$\sum m_\nu < 0.18 \text{ eV} \quad (95\% \text{ C.L.}) \quad (1.16)$$

Given this upper bound on the neutrino mass, the resulting relic density is not enough to explain the Dark Matter as mainly composed by them.

1.4.2 Axions

Remaining in the SM scenario, the *axion* is another Dark Matter candidate. This particle is a Nambu-Goldstone boson which corresponds to the phase of a complex field, the Peccei-Quinn field, which breaks the $U(1)_{PQ}$ symmetry. The $U(1)_{PQ}$ field is a global $U(1)$ symmetry, which carries QCD anomalies, proposed by Peccei and Quinn as solution to the strong CP problem [11]. This symmetry is broken at the scale of f_a which is the axion decay constant, also called PQ scale. The relic abundance of the axions [12] can be expressed, using the QCD scale $\Lambda_{QCD} \sim 200 \text{ MeV}$, as

$$\Omega_a h^2 = \theta^2 \left(\frac{f_a}{10^{12} \text{ GeV}} \right)^{1.175}. \quad (1.17)$$

With $\theta \sim 0.1$ and $f_a \sim 10^{12}$ GeV axions can represent an important percentage of the CDM which might consist only of axions. They can be detected through the *Primakoff effect* [13] where an axion is converted into a photon under a proper magnetic field. The CERN Axion Solar Telescope (CAST) [14] and the PVLAS experiment [15] are searching these particles. While the former looks for solar axions, the latter fires polarized light through a long vacuum region with a 5.5 T magnetic field and searches for anomalous rotations of polarization; according to the theory, the vacuum becomes birefringent, thus photons with polarization aligned with the magnetic field are delayed as they are preferentially transformed into axions which travel slower than the speed of light.

The PVLAS collaboration initially claimed the detection of an irregular rotation corresponding to an axion mass of 1-1.5 meV, but retracted their results upon obtaining a null result after upgrades. The current strongest limits, on the axion mass, have been set by the XENON100 experiment [16].

1.4.3 Weakly Interacting Massive Particles (WIMPs)

Concerning SUSY, many interesting features make it attractive, including its role in understanding the fundamental distinction between bosons and fermions and the problems of hierarchy for neutrinos. In this framework, Dark Matter particles are identified with the general definition of: Weakly Interacting Massive Particles (WIMPs). They are stable, cold, non-baryonic and interact only through gravitational and weak forces. If WIMPs are stable, there is a cosmological relic abundance produced during the Big Bang. Assuming for such particles a mass m_χ , one has that for temperature $T > m_\chi$ they were in thermal equilibrium while at temperatures below m_χ they decoupled and their abundance started to lower. Finally, when the expansion rate of the Universe became larger than the annihilation rate ($\Gamma < h$), where h is the Hubble constant, the WIMP abundance "frozen out", resulting in the current relic abundance.

The annihilation cross section of a new particle interacting at the weak scale can be estimated as: $\langle\sigma\rangle \sim 10^{-25} \text{ cm}^3 \text{ s}^{-1}$. Such value is close to the one derived from cosmological arguments. This strongly suggests that if a stable particle associated with the electro-weak scale interactions exists, then it is likely to be the dark matter particle. This coincidence has provided strong motivation for finding WIMPs.

There are several WIMP candidates; the most promising is the Lightest Supersymmetric Particle (LSP), which is the *neutralino*.

1.4.4 Neutralino

The Minimal Supersymmetric Standard Model (MSSM) contains the smallest possible field content necessary to give rise to all the Standard Model (SM) fields. All of the SM particles have R-parity equal to 1 and all *sparticles*, their superpartners, have $R = -1$. Thus, from R-parity conservation (first introduced to suppress the rate of proton decay), *sparticles* can only decay into an odd number of *sparticles* (plus Standard Model particles). The Lightest Supersymmetric Particle is, therefore, stable and can only be destroyed via pair annihilation, making it an excellent Dark Matter candidate. Among few alternatives, the most promising LSP is the lightest neutralino, which is uncharged under electromagnetic and strong interactions. In the MSSM, binos (\tilde{B}), winos (\tilde{W}_3) and higgsinos ($\tilde{H}_1^0, \tilde{H}_2^0$) states mix into four Majorana fermionic mass eigenstates, called neutralinos. The four neutralinos are labeled as: $\tilde{\chi}_1^0, \tilde{\chi}_2^0, \tilde{\chi}_3^0$ and $\tilde{\chi}_4^0$. The first of them is the lightest one and it is referred as the neutralino, $\chi = \tilde{\chi}_1^0$. The most relevant neutralino interactions for Dark Matter searches are self annihilation and elastic scattering with nucleons. At low velocities, the leading channels for neutralino annihilations are into fermion-antifermion, gauge bosons pairs and final states containing Higgs bosons. All the possible annihilation processes are of interest for indirect Dark Matter searches, while direct detection techniques are based on the elastic scattering processes. The WIMP interaction with the matter can be divided into two types: spin-independent (SI) and spin-dependent (SD). A scalar interaction, i.e. SI, with quarks can be expressed as

$$\mathcal{L} = a_q \chi \bar{\chi} \bar{q} q \quad (1.18)$$

where a_q is the WIMP-quark coupling. The scattering cross section is given by

$$\sigma_{scalar} = \frac{4m_r^2}{\pi} f_{p,n}^2 \quad (1.19)$$

where m_r is the reduced mass of the nucleon and $f_{p,n}^2$ is the coupling to protons and neutrons. The total scalar cross section for interactions with a nucleus, in the case of zero transfer momentum, is given by the sum over all the nucleons:

$$\sigma = \frac{4m_r^2}{\pi} \left(Z f_p + (A - Z) f_n \right)^2. \quad (1.20)$$

A spin-dependent interaction, i.e. axial-vector interaction, between WIMPs and quarks can be expressed as

$$\mathcal{L}_{AV} = d_q \bar{\chi} \gamma^\mu \gamma_5 \chi \bar{q} \gamma^\mu \gamma_5 q, \quad (1.21)$$

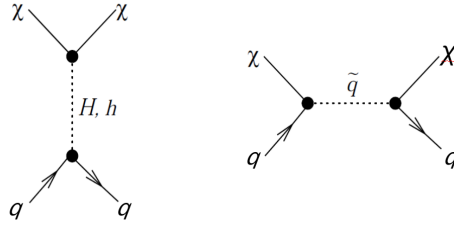


FIGURE 1.10: Feynman diagrams for neutralino-quark scalar (**spin-independent**) elastic scattering interactions [17].

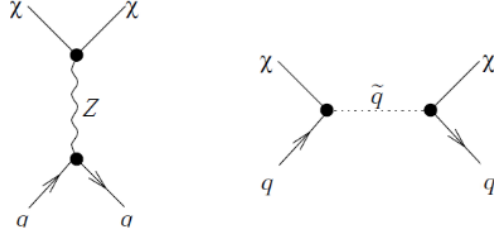


FIGURE 1.11: Feynman diagrams for neutralino (**spin-dependent**) axial-vector interactions [17].

where d_q is the generic coupling. The Feynman diagrams for both SI and SD neutralino interactions are shown in Fig.1.10 and 1.11.

The cross section for SD interactions is given by [18]

$$\frac{d\sigma}{d|\vec{v}|^2} = \frac{1}{2\pi v^2} \overline{|T(v^2)|^2}, \quad (1.22)$$

where v is the WIMP velocity relative to the target and $T(v^2)$ is the scattering matrix element. At zero transfer momentum, one has

$$\begin{aligned} \overline{|T(0)|^2} = & \frac{4(J+1)}{J} |(d_u \Delta_u^p + d_d \Delta_d^p + d_s \Delta_s^p) \langle S_p \rangle + \\ & + (d_u \Delta_u^n + d_d \Delta_d^n + d_s \Delta_s^n) \langle S_n \rangle|^2, \end{aligned} \quad (1.23)$$

where J is the total nuclear spin of the target nucleus, $\Delta_{u,d,s}^{n,p}$ are the fractions of the nucleon spin carried by a given quark and $\langle S_{p,n} \rangle$ are the expectation values of the total spin of protons and neutrons, respectively. For target nuclei with even numbers of protons and neutrons, the total spin is equal to 0. Thus, for such nuclei, the spin-dependent cross section vanishes.

Another kind of interaction to be considered is the WIMP-quark vector interaction:

$$\mathcal{L}_V = b_q \bar{\chi} \gamma_\mu \chi \bar{q} \gamma_\mu q \quad (1.24)$$

where b_q is the WIMP-quark vector coupling. The zero transfer momentum cross section can be expressed as [19],

$$\sigma = \frac{m_\chi^2 m_N^2 [2Zb_p + (A - Z)b_n]^2}{64\pi(m_\chi + m_N)^2}, \quad (1.25)$$

with $b_q = G_F(T_q^3 - 2e_q \sin^2 \theta_W)/\sqrt{2}$, where G_F is the Fermi constant, T_q^3 and e_q are the weak isospin and electric charge of the quark q , respectively, and θ_W is the Weinberg angle.

1.4.5 Sneutrino, Gravitino and Axino

In the SUSY context the sneutrino and gravitino, the superpartners of the SM neutrino and graviton, have been considered as DM candidate. The **sneutrino** is a viable candidate if its mass were in the range [550, 2300] GeV/c². Despite this possibility, it has been rejected since its cross section would be higher than the current found limits. The **gravitino** interacts only through the gravitational force and this makes it very hard to detect. Gravitinos can be produced in $2 \rightarrow 2$ processes such as scalar-fermion-gravitino or gaugino-gauge boson-gravitino vertices [20].

The Axino, \tilde{a} , is the superpartner of the axion and it is a Majorana chiral fermion. Its mass is strongly model-dependent meaning that it could be the lightest particle, thus stable, in SUSY models. A production channel for \tilde{a} is the decay of nonthermal particles. An example of this process is the decay of the lightest *stau* mass eigenstate $\tilde{\tau}_2$.

1.4.6 Wimpzillas

The Super heavy Dark Matter, also named wimpzillas, has been proposed as a non-thermal Dark Matter candidate. The masses of this kind of particles range from 10^{12} up to 10^{16} GeV/c². In the early Universe there were different available channels to produce such particles as the gravitational production at the end of inflation, resulting from the expansion of the background space-time. The interaction cross section of such particles with ordinary matter, covers a wide range of hypotheses, from very weak to strong coupling (in the latter case super-massive particles are sometimes called simpzillas). The wimpzillas have been proposed as a first explanation for the observed ultra high energy cosmic rays, above the GZK cut-off ($\sim 5 \cdot 10^{19}$ eV). Above this energy the Universe, on cosmological scale (≥ 50 Mpc), is opaque to protons. Since sources for such energetic protons have not been observed yet, a possible explanation for their existence is that they are produced in the decay or annihilation of super heavy Dark Matter particles. (top-down cosmic-ray models [21]).

1.4.7 Kaluza-Klein particle

In the **Extra dimensions model**, the space is considered to have four dimensions needed to include electromagnetism into a 'geometric' theory of gravitation. Also in this scenario, the lightest particle, called **Kaluza-Klein** (KK) particle, is a viable candidate for the Dark Matter. If Standard Model particles propagate in such Extra dimensions and the KK parity is conserved, the lightest KK particle is stable, becoming an excellent candidate for DM. The mass of the first stable KK particle ranges from several hundreds of GeV up to few TeV, and can be detected via elastic scattering in the Dark Matter direct search experiments, or indirectly via annihilation products, such as positrons from the galactic halo, gamma rays from the galactic center, high energy neutrinos from the core of the Sun or the Earth, and antiproton. Due to their characteristics, a tonne-scale detector is required to detect their interactions that makes suitable experiments as XENON1T.

1.5 Experiments searching for WIMPs

In the last few decades the Dark Matter search has been one of the most active and interesting field in physics, and a great variety of experiments were constructed for Dark Matter detection. The DM experiments can be divided in two main classes: **direct detection**, based on DM scatterings off target nuclei, and **indirect detection**, searching for DM particles annihilation products inside and outside the galaxy. Different choices of the detection technique and target material allow to scan different ranges of the parameter space of DM models. The indirect detection looks for the products of the interactions among Dark Matter itself. According to the type of the particle produced, the detector technology is different and specific to that particle detection, as, for instance, the observation of the gamma radiation must be done outside the terrestrial atmosphere, which is opaque to. This kind of observation is made with Čerenkov telescopes. Neutrinos and antineutrinos, produced by the annihilation of the Dark Matter inside massive bodies, are observed with large area telescope such as the submarine telescope KM3NeT in Sicily or ICECUBE at the south pole. It is also possible to observe the radio waves produced by the charged particles as a result of the annihilation. A measurements of Dark Matter through the listening of these radio waves could be done only if we know the distribution of Dark Matter in the galaxy questioned.

Lastly, it is particularly interesting the analysis of the production of particle-antiparticle, such as $p\bar{p}$ and e^-e^+ : the **AMS-02** experiment on the satellite of the International Space Station ISS observed an unexpected abundance of antimatter that can be attributed to Dark Matter annihilation. Unfortunately the origin of these particle is still unknown

because the charged particles are deflected by the galactic electromagnetic fields.

The most recent story of the best results for WIMP masses above $8 \text{ GeV}/c^2$ sees at first what has been obtained in 2012 by **XENON100** [22], reaching the best spin-independent (SI) limit of $2 \cdot 10^{-45} \text{ cm}^2$ at $55 \text{ GeV}/c^2$ mass. In 2013 LUX [23] improved the limit to $7.6 \cdot 10^{-46} \text{ cm}^2$ for $33 \text{ GeV}/c^2$ WIMPs and then an update of the result stated a WIMP-nucleon SI cross sections above $2.2 \cdot 10^{-46} \text{ cm}^2$ at 90% confidence level (C.L.). When combined with the previously reported LUX exposure, this exclusion has been strengthened to $1.1 \cdot 10^{-46} \text{ cm}^2$ at $50 \text{ GeV}/c^2$ [24]. Finally, in spring 2017 **XENON1T** [25] has obtained the most stringent exclusion limits on the spin-independent WIMP-nucleon interaction cross section for WIMP masses above $10 \text{ GeV}/c^2$, with a minimum of $7.7 \cdot 10^{-47} \text{ cm}^2$ for $35\text{-GeV}/c^2$ WIMPs at 90% confidence level.

At lower masses, other experiments, as **CoGeNT** and **CDMS** that use a different detector, are more sensitive.

In the next sections we browse through the main Dark Matter experiments based on both direct and indirect detection techniques.

1.5.1 Direct detection experiments

Dark Matter interactions with ordinary nuclei are characterized by very small cross sections. The direct detection of WIMP-nucleon scatterings requires very large target masses and an extremely low level of radioactivity. Hence, an ultrapure detector is mandatory as well as its placement into underground laboratories in order to properly reduce the background. The detection technique aims to the observation of WIMP with velocity lower than the escape velocity from the Milky Way, thus the particles trapped inside the galactic halo. The collisions between WIMPs and nuclei are both elastic and not-elastic and there might be a spin dependance. Due to the very small cross section, the exposure times are very long: according to some theoretical model, a sample of 2 kg ($\sim 10^{25}$ atoms) undergoes an interaction with a WIMP only once in a year through elastic diffusion [26].

In the next part of this chapter we go through the variuos experiment for the direct Dark Matter detection.

DAMA/LIBRA The DAMA/LIBRA detector, placed in the **LNGS** (**L**aboratori **N**azionali del **G**ran **S**asso) underground laboratory, is the upgrade of the previous DAMA/NaI detector. The experiment aims to find an annual variation of the number of detected events, caused by the variation of the velocity of the detector relative to the Dark Matter halo as the Earth orbits the Sun. Its sensitive part is made of 25 highly radio-pure NaI(Tl) crystals, each one of 9.70 kg , arranged in a 5×5 matrix. For

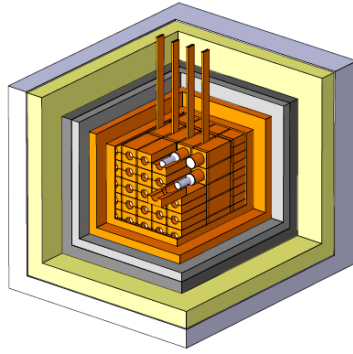


FIGURE 1.12: DAMA/LIBRA detector: schematic view of the 25 highly radio-pure NaI(Tl) scintillator crystals within the passive shield. It is made of a sealed copper box flushed with highly pure nitrogen; to reduce the natural environmental background the copper box is surrounded by a low background multi-ton shield. In addition, 1 m of concrete, made from the Gran Sasso rock material, almost fully surrounds this passive shield. The installation has a 3-level sealing system which prevents environmental air reaching the detectors.

the Dark Matter search, the modularity of DAMA/LIBRA is very useful since WIMPs are expected to give only one interaction in the entire stack of detectors. Moreover, the characteristics of the scintillators allow to reject noise events. With the exception of the noise rejection, in DAMA/LIBRA it is not possible to distinguish between nuclear and electromagnetic recoils.

DAMA/LIBRA has observed a signal modulation that could be explained as due to the modulation of the Dark Matter flux [27]. Several explanations for the modulation signal have been proposed to investigate a possible background as source of this signal. For example, since DAMA/LIBRA does not have a muon veto, it was hypothesized that it was the modulation of the muon flux to generate the signal [28]. However, recently it was shown that the muon flux is too low to explain the observed signal [29].

CoGeNT The CoGeNT Dark Matter Experiment (Fig. 1.13) is a direct search for signals from interactions of Dark Matter particles in a low-background germanium detector located at the *Soudan Underground Laboratory* in Minnesota, USA. The experiment uses a single, 440 g, high-purity germanium crystal cooled to liquid nitrogen temperatures in its measurements. The CoGeNT detector has the advantage of a very low energy threshold (~ 0.5 keV) which allows it to search for nuclear recoil events due to Dark Matter particles of relatively low mass (> 5 GeV/ c^2). In addition to a low-background configuration, the detector is capable of distinguishing and rejecting background events from the surface through measurement of the risetime of the detector's signals. The CoGeNT detector senses only ionization charge from nuclear recoils and places limits on the mass and interaction cross-section of Dark Matter particles by excluding any candidate mass and cross-section pair that would result in a signal above the background

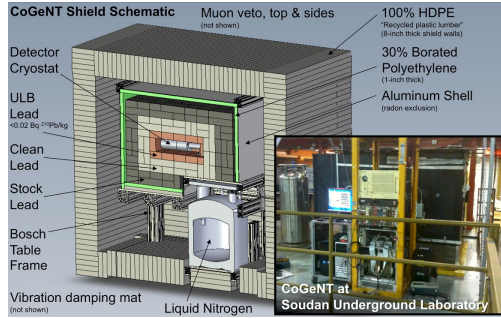


FIGURE 1.13: Schematic view of the CoGeNT structure with its passive shield.

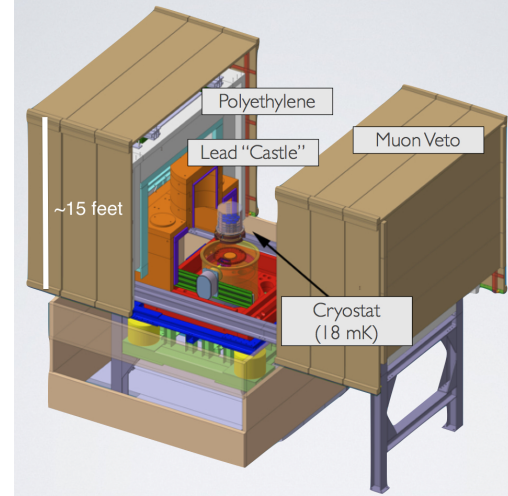


FIGURE 1.14: Schematic view of the EDELWEISS-II experiment.

of the detector. In 2010 CoGeNT observed an excess of events at low energies, in the bulk of the Ge crystal [30]. Several analyses have been performed to explain this excess as due to Dark Matter interactions. Assuming a Maxwellian velocity distribution with $v_0 = 230 \text{ km/s}^{-1}$, and $v_{esc} = 500 \text{ km/s}^{-1}$ for a spin-independent model, with equal coupling to protons and neutrons and without any unknown background, the WIMP hypothesis gives a nice agreement, especially in the very low energy region, with the observed data. The best results were obtained for $m_\chi = 9.4 \text{ GeV}$ and $\sigma = 0.84 \cdot 10^{-40} \text{ cm}^2$. However, such results are excluded by other experiments such as CDMS-Si.

EDELWEISS II The EDELWEISS-II detector (Fig. 1.14), at the *Laboratoire Souterrain de Modane* under 4800 m.w.e., is enclosed in a passive shield, covered by a muon veto system for throughgoing muons. The core of the detector is based on ten bolometers of hyper-pure Ge crystals of cylindrical shapes with a diameter of 70 mm and a height of 20 mm, all inside a cryostat. For each event, two signals are recorded: one from the temperature increase, measured using neutron transmutation doped (NTD)-Ge thermometric sensors glued on each detector, and one from the charges produced in the interaction that are recorded by proper electrode wires on both side of the Ge bolometers. In 2012, the collaboration carried out an analysis on low-energy ($E < 20 \text{ keV}$) WIMP-induced nuclear recoils [31]. For a WIMP mass of $30 \text{ GeV}/c^2$, three events have been found as possible candidates. The data indicated no evidence for an exponential distribution of low-energy nuclear recoils that could be attributed to WIMP elastic scattering after an exposure of $113 \text{ kg} \cdot \text{days}$. For WIMPs of mass $10 \text{ GeV}/c^2$, the observation of one event in the WIMP search region results in a 90% CL limit of $1.0 \cdot 10^{-41} \text{ cm}^2$ on the spin-independent WIMP-nucleon scattering cross section [31].

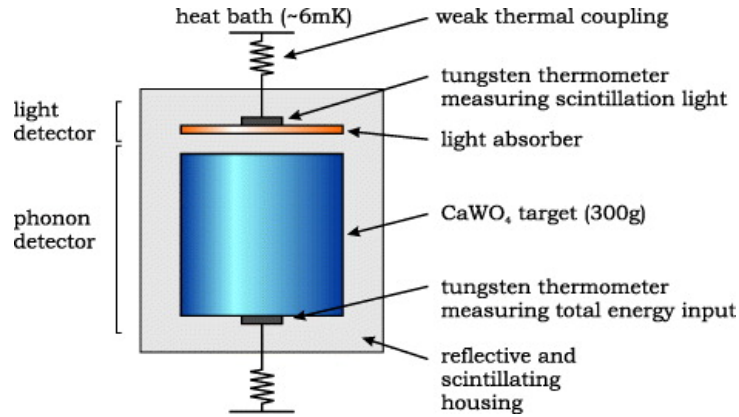


FIGURE 1.15: Scheme of the CRESST-II module.

SuperCDMS The SuperCDMS detector is a bolometer at the Soudan Underground Laboratory. To operate, a cryogenic system based on He_3/He_4 dilution refrigerator has been realized. The core of the detector is made of 15 Ge crystals (600 g each) from which it is possible to extract the phonon and the charge signals. The crystals have cylindrical shape with a diameter of 76 mm and height of 25 mm. The phonon sensor is a superconducting 174 W film held in the transition state from the superconducting to the normal state (therefore called Transition Edge Sensor or TES). A small change in the temperature leads to a large variation in the measured resistance. In 2016 the collaboration carried out the analysis of a run characterized by an exposure of 612 kg·days [32]. This yielded minimum WIMP-nucleon spin-independent scattering cross-section limits of $1.8 \cdot 10^{-44}$ and $1.8 \cdot 10^{-41} \text{ cm}^2$ at 90% confidence for 60 and 8.6 GeV/c^2 WIMPs, respectively.

CRESST-CRESST II-CREST III The CRESST experiment searches directly for Dark Matter particles via their elastic scattering off nuclei. The nuclei are in the absorber of a cryogenic detector, capable of detecting the small energy of the recoiling nucleus which has been hit by an incoming Dark Matter particle. CRESST-II is the upgrade that includes a new neutron shield and a muon veto. CRESST uses simultaneously two independent detectors for revealing heat/phonon and light. The core of the detector is made of modules that consist of a CaWO_4 300 g crystal, the target, and a silicon-on-sapphire (SOS) wafer used for measuring the scintillation light. In their interaction inside the crystals, WIMPs lose energy producing phonons and a small amount of scintillation light. The reading of signals from crystals and SOS is obtained by a Transition Edge Sensor (TES) attached to them. All these elements are enclosed in a reflective and scintillating case (Fig. 1.15).

The use of two detectors allows for precise measurements of the deposited energy and background discrimination. For example, the electromagnetic background rejection can

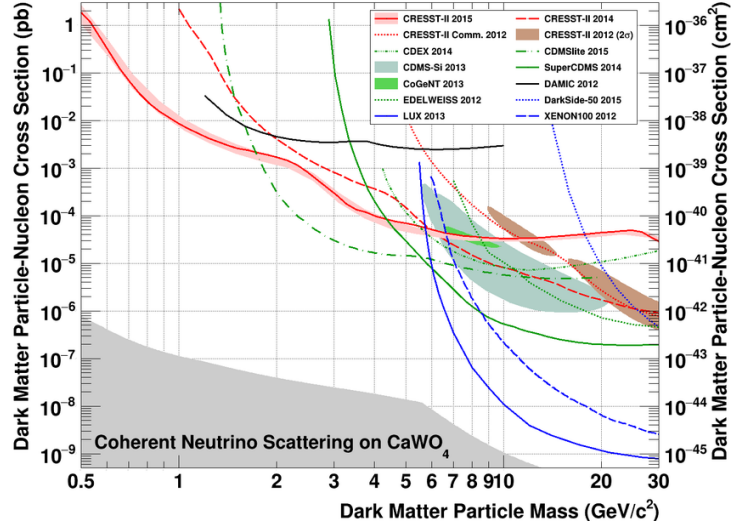


FIGURE 1.16: Parameter space for elastic spin-independent Dark Matter-nucleon scattering. The result from a blind analysis is drawn in solid red together with the expected sensitivity (1σ confidence level (C.L.)) from the data-driven background-only model (light red band). The remaining red lines correspond to previous CRESST-II limits [34]. The favored parameter space reported by CRESST-II phase 1, CDMS-Si[35] and CoGeNT [36] are drawn as shaded regions. For comparison, exclusion limits (90 % C.L.) of the liquid noble gas experiments are depicted in blue, from germanium and silicon based experiments in green and black. In the gray area coherent neutrino nucleus scattering, dominantly from solar neutrinos, will be an irreducible background for a CaWO_4 -based[37] Dark Matter search experiment WIMP parameter space for spin-independent WIMP-nucleon scattering.

be achieved using the scintillation to phonon signals ratio. In 2016, the CRESST-II collaboration has published results from the analysis of a $52 \text{ kg} \cdot \text{days}$ run, exploring masses down to $0.5 \text{ GeV}/c^2$, a novelty in the field of direct Dark Matter searches [33]. In Fig. 1.16 the exclusion limits from several DM experiments in the low WIMP mass region are shown.

DarkSide The DarkSide experiment is looking for WIMP dark matter using a 50 kg liquid argon target in a dual-phase time projection chamber (TPC) located deep underground at Gran Sasso National Laboratory (LNGS). Liquid argon is a bright scintillator with excellent particle identification properties. The TPC, as shown in Fig.1.17, is enclosed first by a 4 m diameter spherical organic liquid scintillator detector, designed to veto neutrons and gamma rays, and next by a 11 m diameter by 10 m high cylindrical water Cherenkov detector, for vetoing the residual cosmic ray flux and passively shielding neutrons and gammas from natural radioactivity. The entire underground facility is shielded by 3600 meter water equivalent of rock, where the muon flux is suppressed by six orders of magnitude with respect to sea level.

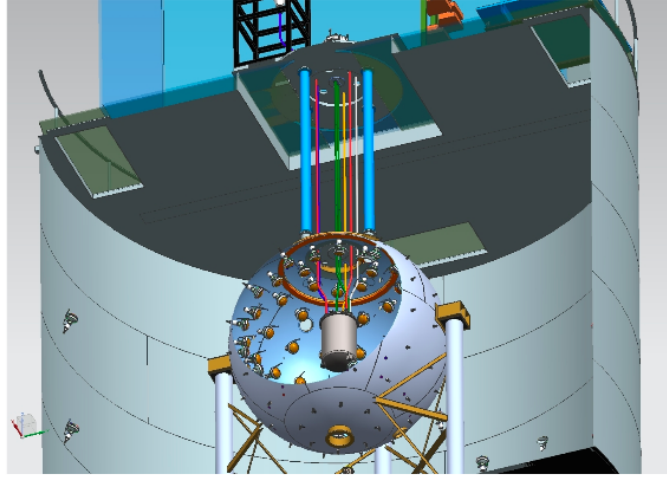


FIGURE 1.17: The nested detector system of DarkSide-50. The outermost gray cylinder is the water Cherenkov detector, the sphere is the liquid scintillator veto, and the gray cylinder at the center of the sphere is the LAr TPC cryostat.

A first dark matter search performed with atmospheric argon has shown a large light yield of ~ 8 photoelectrons (PE) per keV which results in a very good separation of signal from background ($> 1.7 \cdot 10^7$) using the information contained in the pulse shape. In the next run, the TPC was emptied and refilled with underground argon which is depleted in ^{39}Ar by a factor 1400. Combining the null results of these two runs, in 2015, an exclusion limit is placed which is at $2.0 \cdot 10^{-44} \text{ cm}^2$ at the 90% confidence level for a WIMP mass of $100 \text{ GeV}/c^2$ [38]. On long-term, DarkSide plans on a multi-ton detector featuring 3.6 tons with an upgrade to 20 tons LAr in the target volume [39].

LUX The Large Underground Experiment (LUX) is based on a double phase Time Projection Chamber (TPC) which contains Xe in liquid and gaseous phases. The TPC, which contains an active volume of LXe of about 300 kg, is hosted in a double vessel structure that guarantees thermal isolation (Fig. 1.18). The detector is placed at the Stanford Underground Research Facility (SURF) at a depth of ~ 1500 m and it is surrounded by a water tank that acts as muon veto. The TPC has a diameter of 47 cm and a height of 48 cm.

LUX published its last results in 2016. After a $3.35 \cdot 10^4$ kg-day exposure, there was no evidence of WIMP nuclear recoils. At a WIMP mass of $50 \text{ GeV } c^2$, WIMP-nucleon spin-independent cross sections above $2.2 \cdot 10^{-46} \text{ cm}^2$ are excluded at the 90% confidence level. When combined with the previously reported LUX exposure, this exclusion strengthens to $1.1 \cdot 10^{-46} \text{ cm}^2$ at $50 \text{ GeV } c^{-2}$. After the selection of a 118.3 kg fiducial volume for the analysis, 160 events have been observed in the WIMP search region. From the

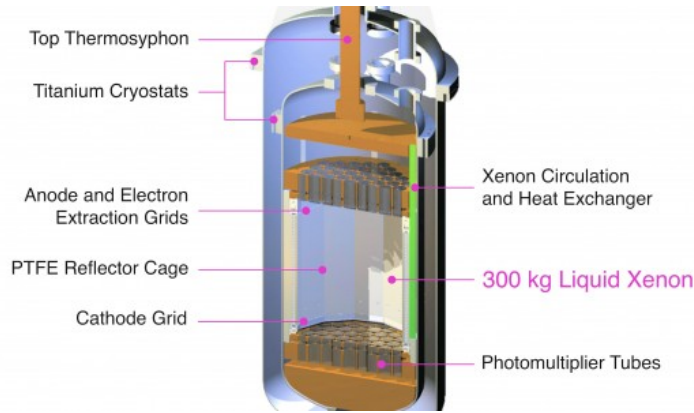


FIGURE 1.18: LUX cryostats and TPC structures.

likelihood analysis, all the events have been found to be compatible with the background-only hypothesis resulting in an upper limits for the DM spin-independent cross section, whose minimum has been found at $7.6 \cdot 10^{-46} \text{ cm}^2$ for a WIMP mass of $33 \text{ GeV}/c^2$ [24].

XENON The XENON Collaboration faces the direct search for WIMPs through a scalable LXe detector arranged in a double-phase TPC. The first stage was the XENON10 experiment, successively upgraded to XENON100. The further extension is represented by the XENON1T experiment. In spring of 2017, the collaboration has reported the first dark matter search result from XENON1T [25], which improves the limit reached by LUX, Fig. 1.19. Currently, XENON1T is again in data acquisition phase and we expect to reach a sensitivity of $1.6 \times 10^{-47} \text{ cm}^2$ in the full nominal $2 \text{ ton} \times \text{year}$ exposure [40]. The future upgrade of the detector, XENONnT, is already under development to achieve another order of magnitude improvement in sensitivity by 2023. We describe in detail this experiment in the next chapter.

1.5.2 Indirect detection experiments

Indirect techniques aim to detect DM decay or annihilation products. It is usually assumed that WIMPs can annihilate in SM particles. Viable signatures for such kind of processes are thus the production of neutrinos, γ -ray, positrons, anti-protons and anti-deuterons.

General Antiparticle Spectrometer (GAPS) GAPS (General Antiparticle Spectrometer) is a proposed experiment to search for the anti-deuteron particle in the cosmic rays. Astrophysically produced anti-deuterons have never been detected and so the unambiguous detection of even a single event would be very significant. Antideuterons may also be a telltale signature of Dark Matter annihilations. Secondary antideuterons

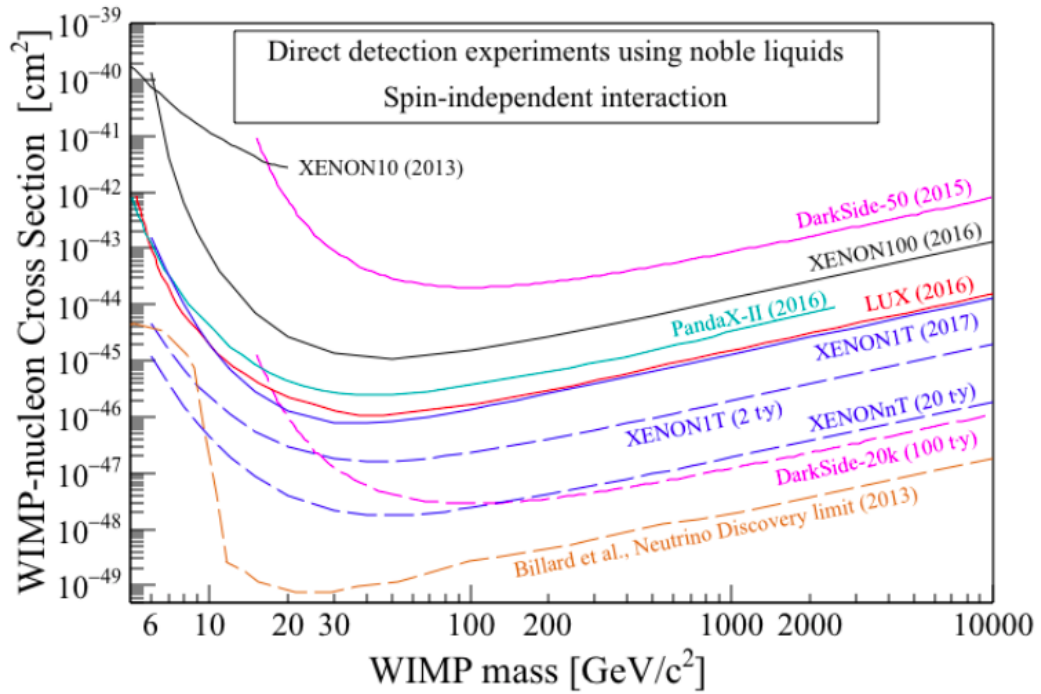


FIGURE 1.19: Comparison between sensitivities and upper limits at 90% CL from different experiment: DarkSide (purple), PandaX (green), XENON100 (black), LUX (red), XENON1T (blue), XENONnT (blue dashed) and the neutrino bound (orange dashed).

can be produced in collisions of cosmic rays (CR) with the interstellar medium (IM). Due to the mass of such nuclei, low energy productions are quite disadvantaged leading to a reduced background in the search for low energy nuclei.

GAPS will detect anti-deuterons with an effectively background-free method. Anti-deuterons, produced by the annihilation of weakly interacting massive particles (WIMPs), will be captured in the GAPS target material, resulting in an exotic atom in an excited state. This exotic atom will then quickly decay, producing X-rays of precisely defined energies and a correlated pion signature from nuclear annihilation. The GAPS method has already been successfully tested in an accelerator environment at KEK in 2004 and 2005. A balloon prototype experiment with a TOF system and 6 Si(Li) detectors was successfully flown in June 2012. The first data acquisition is planned for 2017.

VERITAS The VERITAS telescope consists of four, 12 m diameter Davies-Cotton optical reflectors (Fig. 1.20). They focus the light from γ ray air showers, in the energy range 100 GeV-50 TeV, onto four 499 pixel PMT cameras. Its observations are mainly directed to dSph galaxies (dwarf spheroidal galaxy), they are gravitational-bound objects and are believed to contain up to $\mathcal{O}(10^3)$ times more mass as Dark Matter than as visible matter, making them widely discussed as potential targets for indirect Dark



FIGURE 1.20: View of the VERITAS telescope array.

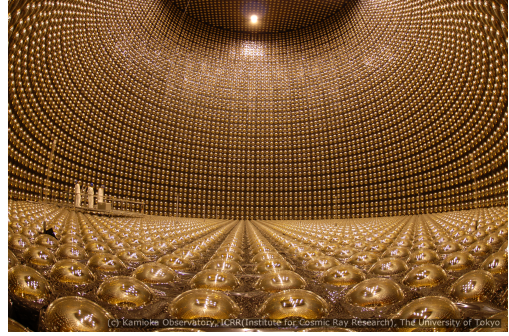


FIGURE 1.21: Internal view of the Super-Kamiokande detector.

Matter observations. One of the most important results from VERITAS comes from the observation of the gamma-ray flux, perhaps originated by annihilation or decay of Dark Matter [41]. Since no signal above the background has been observed, only upper limits on the gamma-ray flux have been set considering different annihilation channels.

Super-Kamiokande The Super-Kamiokande (SK) detector, Fig. 1.21, is a kton water Čerenkov detector of cylindrical shape with height of 36.2 m and radius of 16.9 m. It is located in the Kamioka-Mozumi mine in Japan under about 1000 m rock. It consists of a inner detector with 11146 inward-facing 50 cm diameter PMTs and an outer detector equipped with 1885 outward-facing 20 cm diameter PMTs, serving as a cosmic ray veto counter. This detector is able to search for Dark Matter through the detection of an excess of upward-going muons (upmu). These muons are generated by the muon neutrinos (generated in DM annihilations in the Sun) which interacts with rocks that surround the detector. Muon events in the detector have been divided into three categories: **stopping**, i.e. muons with the lowest energy that stop in the detector ($E_\nu \ll 10$ GeV); **showering**, i.e. muons that produce showers in the detector and **non-showering**, which don't produce any shower. For their last results, the collaboration used data acquired in 3903 days to search for the contribution of neutrinos from WIMP annihilation in the Sun. No significant excess over expected atmospheric-neutrino background has been found and the result is interpreted in terms of upper limits on WIMP-nucleon elastic scattering cross sections under different assumptions about the annihilation channel. The current best limits on the spin-dependent (SD) WIMP-proton cross section for WIMP masses below 200 GeV/ c^2 is $1.49 \cdot 10^{-39}$ cm² for $\chi\chi \rightarrow b\bar{b}$ and $1.31 \cdot 10^{-40}$ cm² for $\chi\chi \rightarrow \tau^+\tau^-$ annihilation channels, also ruling out some fraction of WIMP candidates with spin-independent (SI) coupling in the few-GeV/ c^2 mass range [42].

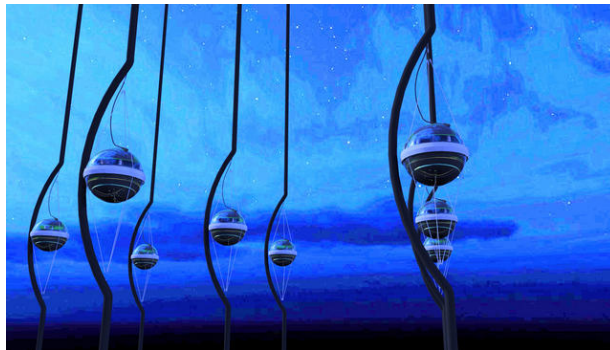


FIGURE 1.22: Representations of IceCube's DOMs.

Large Area Telescope The Fermi-Large Area Telescope (Fermi-LAT) is a γ -ray telescope, placed on board the Fermi Observatory, sensitive to energies from 20 MeV up to over 300 GeV. One of the goals of this telescope is to find a DM signature in the diffuse γ -ray emission. At galactic level, it is believed that the signal comes from annihilation of WIMPs in a smooth halo around the galaxy while the extragalactic signal arises from DM annihilation processes throughout the Universe. For the galactic halo study, the Fermi-LAT collaboration explored the energy range [1, 400] GeV. Limits were set both for annihilation and decay of DM particles [43].

IceCube IceCube is a neutrino telescope placed at the south pole that aims at the detection of the Čerenkov light emitted by muons, created by neutrinos interacting with the Antarctica ice. The neutrinos of interest are generated by Dark Matter annihilations in the Earth and in the Sun. The telescope consists of 86 vertical strings equipped with Digital Optical Modules (DOMs), Fig. 1.22, that contain a digitizer board and a PMT. Part of these strings (78) carry 60 DOMs, placed at intervals of 17 m from a depth of 1450 m up to 2450 m below the ice surface. The other 8 strings are infill-specialized for a sub-array dubbed DeepCore, placed in the central region of the telescope.

IceCube is sensitive to neutrinos in the energy range from 100 GeV up to 1 TeV, while DeepCore can reach sensitivity down to 10 GeV neutrinos. This means that the entire telescope is sensitive to neutralinos down to masses of about 50 GeV.

The main background of the telescope is due to muons and neutrinos produced by cosmic rays interacting in the atmosphere. To take into account all the possible background variations, the dataset used in the last analysis was divided into three parts: summer season, focused on low energy neutrinos, and winter season which is, in turn, divided into a low and high energy sample. After all the cuts and track selection criteria, the observed distributions of the event directions have been compared with the expected background distributions from atmospheric muons and neutrinos [44] finding compatibility with the only-background hypothesis. The obtained upper limits on the expected number of

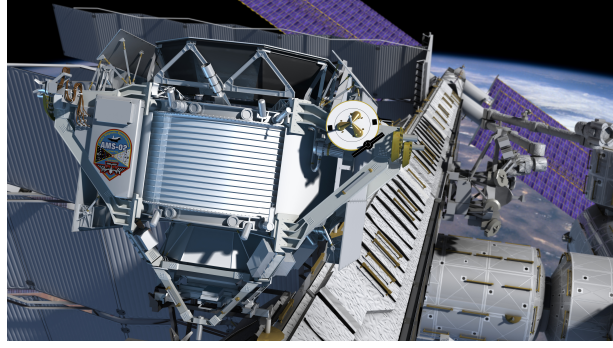


FIGURE 1.23: AMS-02 experiment on the International Space Station.

signal events, μ_s^{90} , can be translated into upper limits for the annihilation rate, Γ_a , of WIMPs in the Sun that, in turn, can be converted into limits on the spin-dependent, $\sigma_{SD,p}$ and spin-independent, $\sigma_{SI,p}$, WIMP-proton scattering cross-sections. For Dark Matter masses between 200 GeV and 10 TeV, the upper limits on the velocity-averaged self-annihilation cross-section reaches a level of $10^{-23} \text{ cm}^3\text{s}^{-1}$. The IceCube data have been also used to infer information and set limits on the super heavy Dark Matter, i.e. for $m_\chi > 100 \text{ TeV}/c^2$ [45]. These values of masses imply a much lower density of Dark Matter which results in a reduced sensitivity for direct detection experiments. Due to the low density, this kind of search is based on the detection of the decay products such as high energy neutrinos. Considering Dark Matter with $m_\chi \approx 100 \text{ TeV}$ that decays into two neutrinos, IceCube already set limits on the lifetime giving the strongest limit: $\tau > 10^{27} \text{ y}$ [46].

AMS-02 The Alpha Magnetic Spectrometer (AMS), currently in its second phase AMS-02, is an antimatter search experiment placed on the International Space Station (ISS), (Fig. 1.23). In its latest results [47], the AMS collaboration found an excess in the positron fraction, at energies $> 8 \text{ GeV}$, above the expected background due to secondary positrons originate in the spallation of cosmic rays on the interstellar medium. The positron fraction excess stops at $\sim 275 \text{ GeV}$ and this excess seems to be isotropic within 3%, suggesting that the energetic positrons may not be coming from a preferred direction in space.

Considering also the antiproton results from PAMELA [48], where the antiproton flux is compatible with the expected background, a scenario that consider a leptophilic Dark Matter, as possible source of positrons, is viable [49].

This kind of candidates annihilates predominately into leptons producing a large amount of energetic positrons while the antiproton flux remains suppressed. Using this kind of WIMP and considering masses above $500 \text{ GeV}/c^2$, the AMS-02 collaboration has evaluated the annihilation cross section for leptophilic channels that can explain the

observed positron fraction [49]; the value for the annihilation cross section is of the order $10^{-23} \div 10^{-22} \text{ cm}^3\text{s}^{-1}$ that is about 10^3 times larger than the thermal cross section.

Chapter 2

The XENON project

Among the various experimental strategies for the direct detection of Dark Matter (DM) particles, detectors using liquid xenon have demonstrated the highest sensitivities. This is the case of the dark matter experiments realized by the *XENON Collaboration*.

The first detector of the XENON project was XENON10 [50]. The main goal of this experiment was to test the possibility to realize a dual phase, LXe/GXe, detector on the kg scale to detect DM interactions. The results obtained in 2007 pushed towards the realization of a new and larger detector, XENON100 [51], based on the same detection and working principles. Both detectors, have been placed in the interferometer tunnel at the Laboratori Nazionali del Gran Sasso (LNGS), Italy, at an average depth of 3600 m water equivalent.

The XENON collaboration is now focusing on the XENON1T experiment [52]: the detector, built between 2013 and 2016, has 30 times larger target mass, and a background reduction of a factor hundred with respect to the XENON100.

At the time of this thesis, the collaboration has presented the results from a first 30 day run acquired between November 2016 and January 2017 to the scientific community. A profile likelihood analysis has shown that the data are consistent with the background-only hypothesis. The most stringent exclusion limits on the spin-independent WIMP-nucleon interaction cross section for WIMP masses above 10 GeV/c² has been set, with a minimum of 7.7×10^{-47} cm² for 35-GeV/c² WIMPs at 90% confidence level [25].

To improve experimental sensitivities or probe with higher statistics a potential signal seen by XENON1T, the collaboration is working on the next stage of the project, XENONnT, with increased active mass and lower background.

2.1 Detection principle of a dual phase TPC

The detectors of the XENON project are based on a dual phase *Time Projection Chamber* (TPC), containing xenon in the liquid phase (LXe) and gaseous xenon (GXe). In this section we review the main properties of xenon as target and detection medium together with the xenon dual phase TPC working principles.

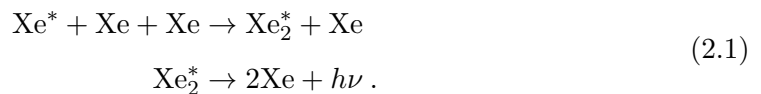
2.1.1 Liquid xenon as target

The choice of LXe as active target for the DM direct detection implies several advantages:

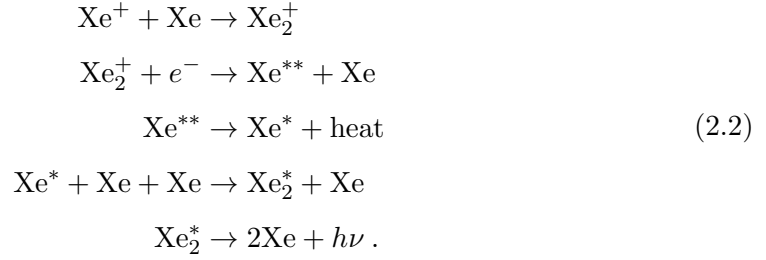
- Self-shielding power against external background sources, due to its high density, equal to 2.96 g/cm^3 ;
- Xenon is not extremely demanding from the cryogenic point of view (-100°C);
- The large atomic number of Xenon ($A = 131$) increases the expected WIMP interaction rate, since the WIMP-nucleus cross section scales with A^2 (see eq.1.25);
- Xenon has about ten stable isotopes, while unstable ones are very short-lived. Hence, it is a rather pure material, which is a mandatory requirement for a search of very rare events like WIMP scatterings. There are two isotopes with nonzero spin: ^{129}Xe (spin 1/2) and ^{131}Xe (spin 3/2). This allows to study also the dependence of the WIMP-nucleus cross section on the spin, thus providing more information about the Dark Matter nature;
- Xenon is an excellent scintillator, since emits about $5 \cdot 10^4$ photons per MeV deposited, ($\lambda = 177.6 \text{ nm}$, i.e. VUV photons) and has also a good ionization yield ($6 \cdot 10^4$ electron-ion pairs per MeV). Therefore, an interaction produces both a large amount of both charges and photons.

2.1.2 Xenon scintillation light

The xenon scintillation is ruled by de-excitation of excimers, i.e. excited xenon dimeric molecules (Xe_2^*), which are formed after recoil events through direct excitation or recombination of ionization products. In the direct excitation process an excited state Xe^* is promptly formed, leading to scintillation through the following reaction chain:



After ionization in the xenon target, the Xe^+ ions can form a molecular state and a freed electron can recombine, producing scintillation at the end of the chain:



Due to the different configuration of the energy levels of dimers and atoms, the photons emitted by dimers are not re-absorbed by the atoms making LXe transparent to its own scintillation light. The scintillation light in LXe has two decay components characterized by two different decay times: the singlet (S) and triplet (T) states of the excited dimers Xe_2^* . The fast scintillation component is due to the S state and its decay time can vary under intense electric fields. For instance, with a 4 kV/cm electric field, the decay times after the interaction of relativistic electrons with xenon atoms are: (2.2 ± 0.3) ns from the singlet states decays and (27 ± 1) ns from triplet states [53].

2.1.3 Signals produced in the TPC

A schematic view of the TPC structure is shown in Fig. 2.1 left; starting from the bottom the TPC is closed by the Cathode (at negative voltage) while on its top it is closed by the Gate mesh (grounded). This structure encloses the LXe active region, called *sensitive volume*, that represents the volume used to detect the interactions and which is available for the electron drift. Along the vertical axis equally spaced thin copper rings are properly distributed, together with the Cathode and the Gate mesh, to generate a uniform electric field.

Above the Gate mesh there is the Anode and the LXe/GXe interface is set between them. Gate mesh and Anode produce the extraction field which has a strength of $\mathcal{O}(10)$ electrons kV/cm, that guarantees an extraction efficiency close to 100%.

Particles interacting in LXe produce a prompt scintillation signal, called **S1**, through excitation, and ionization electrons. The electrons can recombine, participating to the S1 signal, or can be drifted by an appropriate electric field towards the liquid-gas interface where they are extracted by the strong extraction field, and a light signal, named **S2**, is generated by proportional scintillation in the gas. The S2 signal is delayed by the electron drift time from the interaction site to the liquid/gas interface.

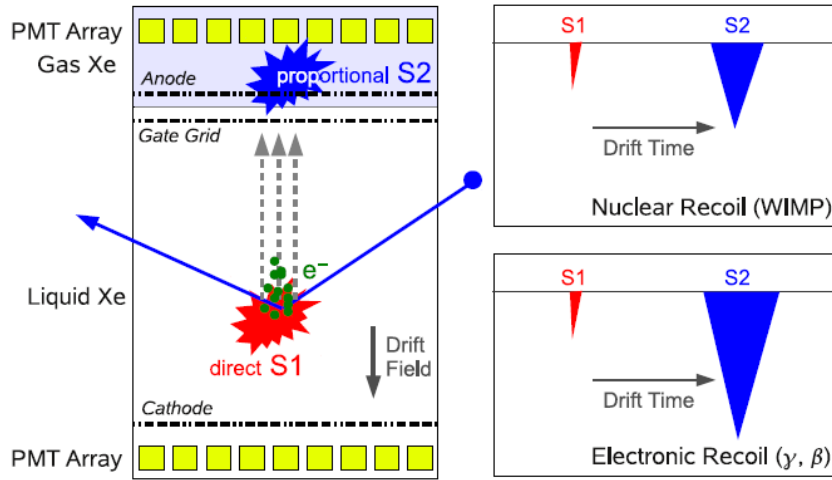


FIGURE 2.1: (Left) Schematic view of the XENON TPC along with its working principle. (Right) Illustration of characteristic wave forms due to different kinds of events, NR and ER.

Two PMT arrays, one on top of the TPC inside the GXe and one at its bottom below the cathode, in LXe, are used to detect the scintillation light. From the pattern of the hit PMTs in the S2 signal, the (x, y) position of the events is determined, while from the time difference between S1 and S2 signals it is possible to infer the z coordinate. Combining all these informations, a 3D vertex reconstruction can be achieved. The knowledge of the interaction point allows the selection of those events located in the inner part of the LXe, usually called *fiducial volume* (FV). Since the majority of background events are expected to be found in the outermost part of the TPC, using the most external volume as shield, the background from external sources can be remarkably reduced.

The S1 and S2 signals are also used to lower the background, thanks to their different distribution in case of either electronic (ER) or nuclear recoils (NR). From the measured S1 and S2 it is possible to achieve a satisfying discrimination power between ER and NR events. Moreover, single scatter interaction (expected from WIMPs) can be distinguished from multiple scatters thanks to the presence of more than one S2 signal in the latter case.

The scintillation efficiency, i.e. the light output per unit energy deposited, for ER and NR is significantly different; therefore it is usual to define two energy scales: keV_{ee} (or keV_e) for ER events and keV_{nr} (or keV_r) for NR events. They are defined so as to avoid misinterpretation of the event energy in the case it is an ER or NR.

An example of the S_1 and S_2 signals pattern from NR and ER is shown in Fig. 2.1 (right).

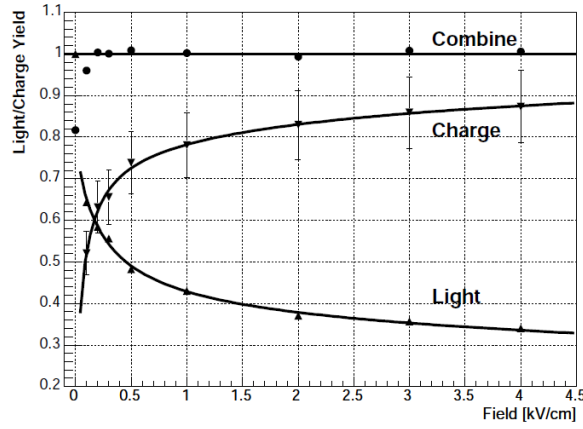


FIGURE 2.2: Light and charge yield as a function of drift field for 662 keV_{ee} γ -rays from ^{137}Cs [54].

2.1.4 Discrimination of ER and NR

The ability to discriminate among different particles is essential for a Dark Matter experiment. WIMPs are expected to produce NR while most of the background radiation produces ER. Particles with different Linear Energy Transfer (LET), dE/dx , have different S2/S1 ratio and this allows to discriminate among them. Indeed, a NR has a higher recombination rate, due to its higher LET, than an ER. A higher recombination gives a lower S2 and a higher S1 and ultimately a lower S2/S1 ratio. This characteristic of the signals implies the anti-correlation between ionization and scintillation signals, which is experimentally observed (Fig. 2.2).

Hence, using the ratio of the signals S1 and S2 as discrimination parameter, it is possible to distinguish between the two types of recoil. Having such a separation between the ER and NR bands, in the S2/S1 parameter, it is possible to set a discrimination level for the ER which allows to reach the desired background level.

The detector response to ER and NR events is studied through calibration with sources of photons (for ER) or neutrons (for NR). As example, the XENON100 performance is shown in Fig. 2.3 [22], where the ER band (blue) is clearly distinguished from the NR band (red).

With the separation achieved by XENON100, it is found that a 99.5% ER discrimination corresponds to a 50% acceptance of NR events, while 99.75% ER discrimination gives 40% NR acceptance [22].

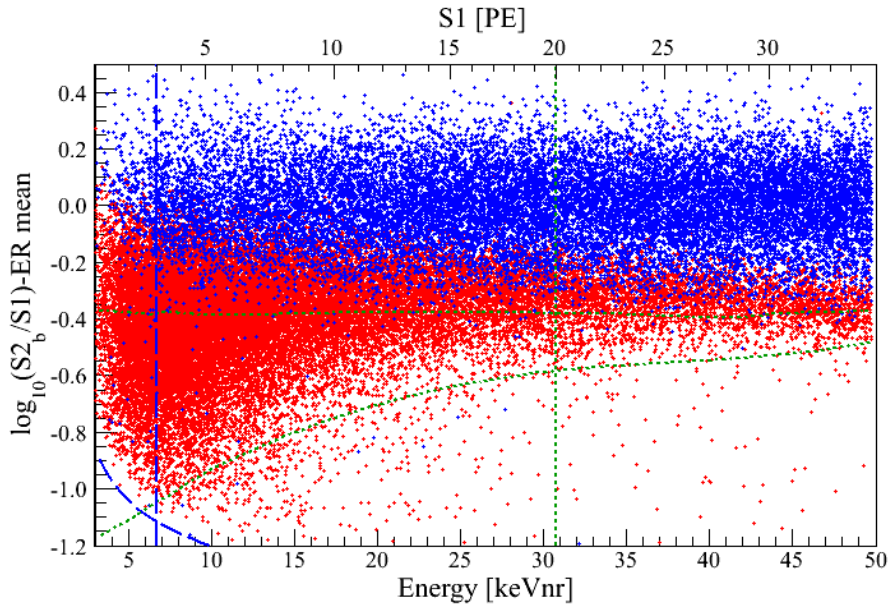


FIGURE 2.3: Distribution of the flattened discrimination parameter, $\log_{10}(S_2/S_1)$, as function of the recoil energy achieved with the XENON100 experiment [22]. The ER band (blue points), obtained from ^{60}C and ^{232}Th calibration data, is showed together with the NR band (red points), from the $^{241}\text{AmBe}$ calibration.

2.2 The XENON experiments

The XENON project started with the XENON10 experiment, with a target mass of the order of 10 kg.

The XENON10 experiment has been followed by XENON100, whose xenon mass is about 170 kg. The mass of the XENON1T experiment has been increased of a further factor 10. Finally, an upgrade to a xenon mass to about 7 tonnes, named XENONnT is already foreseen by the Collaboration.

In the following, we briefly review the main results of XENON10 and XENON100. A more detailed discussion is dedicated to XENON1T. The upgraded phase of the project, XENONnT, that represents the framework of this thesis, will be described in Chapter 3.

2.2.1 XENON10

The XENON10 experiment [50], installed in 2005, has been in operation until October 2007. The TPC was made of a PTFE cylinder with an inner diameter of 20 cm and a height of 15 cm. The amount of LXe contained inside the TPC was 15 kg, with 5.4 kg used as fiducial volume. In 2008, the Collaboration published the results of the 58.6 days run, setting upper limits on both SI and SD WIMP-nucleon cross section. XENON10

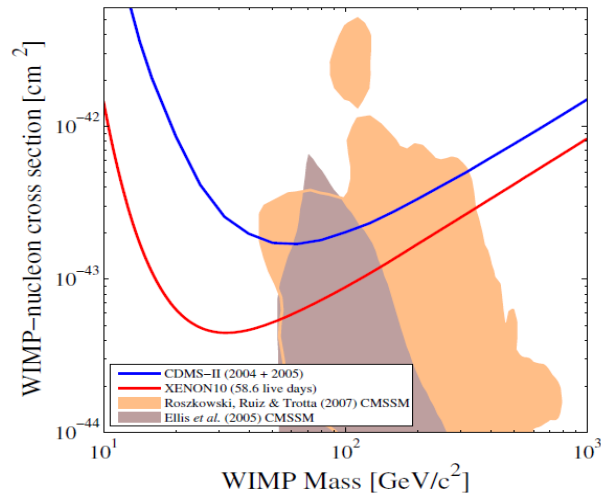


FIGURE 2.4: Cross section limit, 90% CL, on spin-independent WIMP interactions (red line), from the XENON10 58.6 live-days dataset [55]. The blue line is the best limit from CDMS experiment [56]. The shaded areas represent the allowed parameter region in the constrained minimal supersymmetric models.

reached a sensitivity at 90% confidence level to SI cross sections of $8.8 \times 10^{-44} \text{ cm}^2$ for a $100 \text{ GeV}/c^2$ WIMP mass and $4.5 \times 10^{-44} \text{ cm}^2$ for $m_\chi = 30 \text{ GeV}/c^2$ [55] (see Fig. 2.4). Concerning the SD case, a limit for neutron couplings of $5 \times 10^{-39} \text{ cm}^2$ was set for $30 \text{ GeV}/c^2$ WIMP mass [57]. The XENON10 sensitivity plot for SD WIMP interactions is shown together with the result of XENON100 in fig. 2.6.

2.2.2 XENON100

The XENON100 experiment [51] started in 2008. The TPC has a radius of 15.3 cm and a height of about 30.5 cm. The LXe amount was increased to 161 kg, with 62 kg used as active volume in the TPC and the remaining as an outer active veto; In order to be sensitive to a DM interaction, one of the goals of this experiment was to lower the sensitivity by two orders of magnitude with respect to XENON10. Such result has been achieved thanks to a larger target, but also thanks to a factor 100 of background reduction through an accurate screening and selection program for all detector construction materials.

One of the most important results has been obtain with a run of 225 live days [22]. The analysis showed no evidences for Dark Matter. Two events have been found in the energy region of interest for the WIMP search, but this number is compatible with the expected background (1.0 ± 0.2) events. A second data analysis was carried on combining three runs summing up to 477 live days from January 2010 to January 2014. A blind analysis was applied to all the runs prior to combining the results. A profile likelihood analysis using an energy range of $(6.6 - 43.3) \text{ keV}_{nr}$ sets a limit on the elastic,

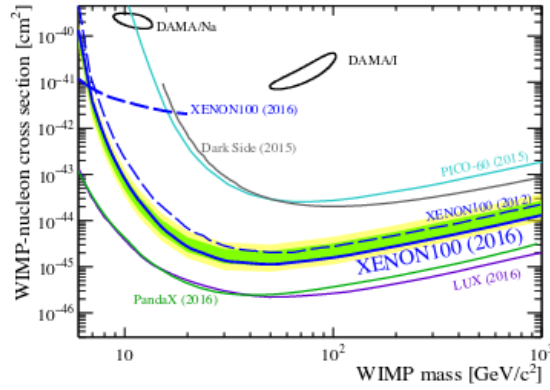


FIGURE 2.5: Spin-independent cross section limit (blue line) and 1σ (green band) and 2σ (yellow band) expected sensitivity regions at 90 % C.L. from the combined analysis of the three XENON100 science runs. For comparison, a subset of other experimental limits (90 % C.L.) and detection claims (2σ) are also shown.[58].

spin-independent WIMP-nucleon scattering cross section for WIMP masses above 8 GeV/c^2 , with a minimum of $1.1 \cdot 10^{-45} \text{ cm}^2$ at $50 \text{ GeV}/c^2$ and 90% confidence level. The constraints on the elastic, spin-dependent WIMP-nucleon cross sections were obtained with the same data set upper limits on the WIMP-neutron (proton) cross section with a minimum of $2.0 \cdot 10^{-40} \text{ cm}^2$ ($53 \cdot 10^{-40} \text{ cm}^2$) at a WIMP mass of $50 \text{ GeV}/c^2$ at 90 % confidence level [61]. The exclusion limits as function of the WIMP mass are shown in Fig. 2.5 and 2.6.

2.2.3 XENON1T

The XENON1T experiment [52] is located in the Hall B, shown in Fig. 2.7, of the Gran Sasso Underground Laboratory (LNGS). The construction of the experiment started in 2013 and has been terminated in 2016.

The total amount of about 3 tonnes of LXe is contained in a double vessel vacuum insulated cryostat made of low activity stainless steel (SS), 5 mm thick. The dimensions of the inner cryostat are chosen to host the XENON1T TPC (Fig. 2.7), while the outer one is increased in order to host also the future enlarged version of the experiment, XENONnT. Both vessels are composed by a cylindrical part and two domes; the top dome is connected to the central part through a flange whose thickness is 50 mm. The upper domes have a central port from which the cryostat is connected to the XENON1T cryogenics system, via a long double-wall vacuum insulated tube.

The target consists of about 2 tonnes of LXe, defined laterally by an almost cylindrical structure of 24 polytetrafluoroethylene (PTFE) interlocking panels: the radius of the TPC is 479 mm. The target volume is viewed by two arrays of PMTs: one made of 121 PMTs in a compact hexagonal structure directly immersed in LXe in the bottom,

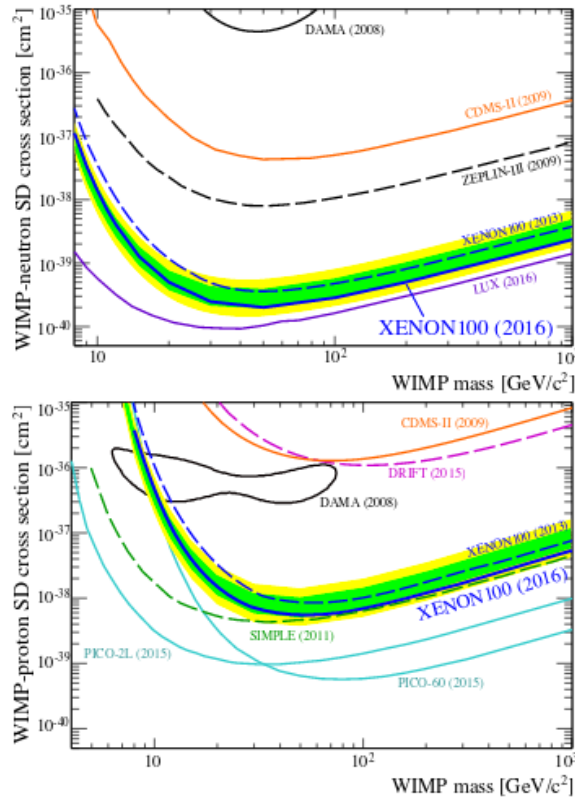


FIGURE 2.6: Spin-dependent cross section limit (blue line) and 1σ (green band) and 2σ (yellow band) expected sensitivity regions at 90 % C.L. from the combined analysis of the three XENON100 science runs. The top (bottom) panel shows the individual neutron (proton) only cross sections. For comparison, other experimental limits (90 % C.L.) and detection claims (2σ) are also shown. CDMS [59], ZEPLIN-III [60].

and one made of 127 PMTs placed in concentric rings in the gas phase above the target volume.

The radius of the bottom array is the same as the TPC, while the top one is slightly larger to guarantee a good position reconstruction even at the edge of the TPC. The space among the PMTs is covered with PTFE to reflect the UV light and ensure a good light collection efficiency. The structure of the TPC is reinforced on the outside region through PTFE pillars and copper rings. Additional PTFE and copper disks support the two PMT arrays.

The electric fields in the TPC are generated through electrodes made of SS meshes welded onto SS rings. There are two electrodes on the bottom of the TPC: the cathode and a second one to screen the bottom PMT array. At the liquid gas interface there is a stack of two electrodes, ground and anode, separated by 5 mm; another mesh is used to protect the top PMTs. The distance between the cathode and the ground meshes, which defines the active region, where both the light and charge signals can be generated, is 967 mm. A stack of 74 field shaping rings, made of copper and placed just outside the PTFE lateral panels, assures the uniformity of the electric field along the TPC.

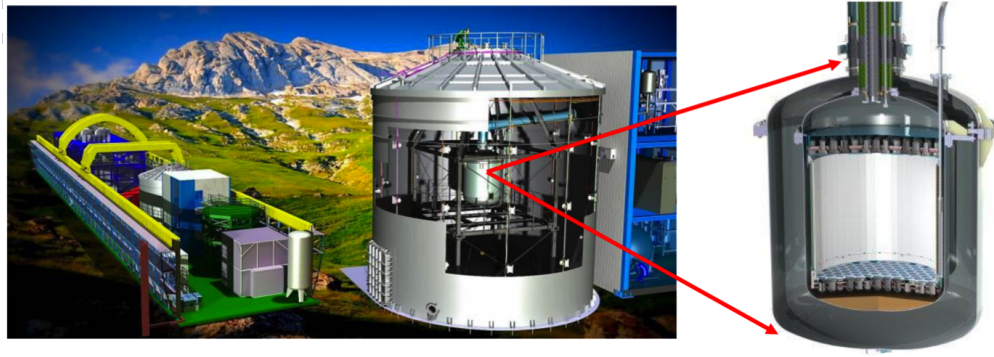


FIGURE 2.7: Picture of the XENON1T TPC and cryostat inside the Muon Veto System.

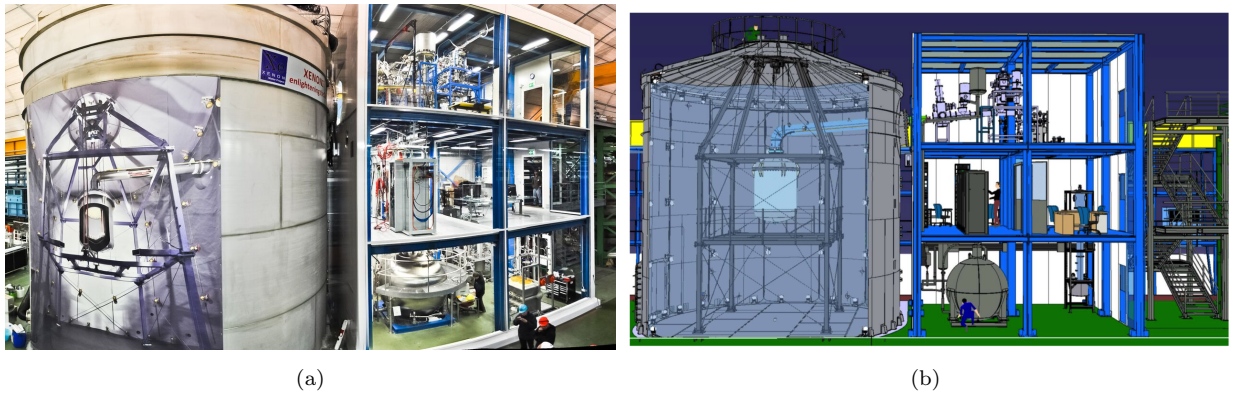


FIGURE 2.8: (a) and (b) picture and drawing of the XENON1T detector: the Muon Veto water tank containing the TPC, the Service Building which hosts the cryogenic and purification system, the DAQ equipment, the distillation column, and the emergency recovery system.

The liquid level in the proportional amplification region is adjusted between the gate and the anode electrode, and kept constant, by using the concept of a diving bell with an adjustable overflow tube coupled to a linear motion feedthrough [51]. The bell closing the gas phase region is made of SS, 5 mm thick on the top and 3 mm in the lateral part. This solution has the advantage that the LXe outside the bell can rise above the top PMT array.

In this way we have a layer of LXe, about 5 cm thick, above the Bell and all around the TPC (outside of the field cage, between the rings and the cryostat wall); a 3 cm LXe layer is kept below the bottom PMT array. In the initial operation phase of the experiment this LXe layer will act as a passive shield to reduce the background from outside; in a second phase it can be instrumented with 1" PMTs and PTFE panels to be operated as an active veto.

2.2.3.1 The background

In order to increase the sensitivity of WIMP-nucleus cross section it is necessary to reduce the background sources.

The principal sources of background signals are:

- Internal background
- Intrinsic background
- External background

2.2.3.2 Internal background

The internal background is due to the radioactivity of materials constituting the detector. For the construction of XENON1T a screening campaign was carried on, the materials with the lowest contaminations from radioactive nuclei were chosen.

The most dangerous electromagnetic backgrounds comes from the γ emitted in the ^{238}U and ^{232}Th chains and from the decay of ^{60}Co , ^{40}K and ^{137}Cs . The γ emitted might cause electron recoil. An optimized choice of the fiducial volume of xenon used in the TPC using its external part as a shield, allows the reduction of the internal background. From Monte Carlo simulations it was estimated that, using part of the xenon as a shielding, the number of background events expected is 0.07 ev/ton/yr [62].

The nuclear recoil due to reactions of the type (α, n) are another source of background. These reactions are produced by the decay chain of U and Th, which are present in the material of the detector. Neutrons produce multiple interactions, a detailed Monte Carlo simulation shows a number of expected events of 0.6 ev/ton/yr.

The total expected internal background is lower than the number of events, ~ 20 ev/ton/yr, expected for a WIMP of mass 100 GeV and cross section 10^{-47} cm².

2.2.3.3 Intrinsic background

The intrinsic background is another source of dangerous events. It is due to some radioactive isotopes that are uniformly distributed in LXe: ^{85}Kr and ^{222}Rn .

Kr decays β with an end point of 687 keV and half life of 10.76 years. To achieve the desired background level XENON1T requires a Kr contamination lower than 1 ppt. The commercial xenon has a contamination of 1 ppm thus a purification through a dedicated distillation column is needed.

Also Rn can be a potential source of intrinsic background since it is mixed inside the

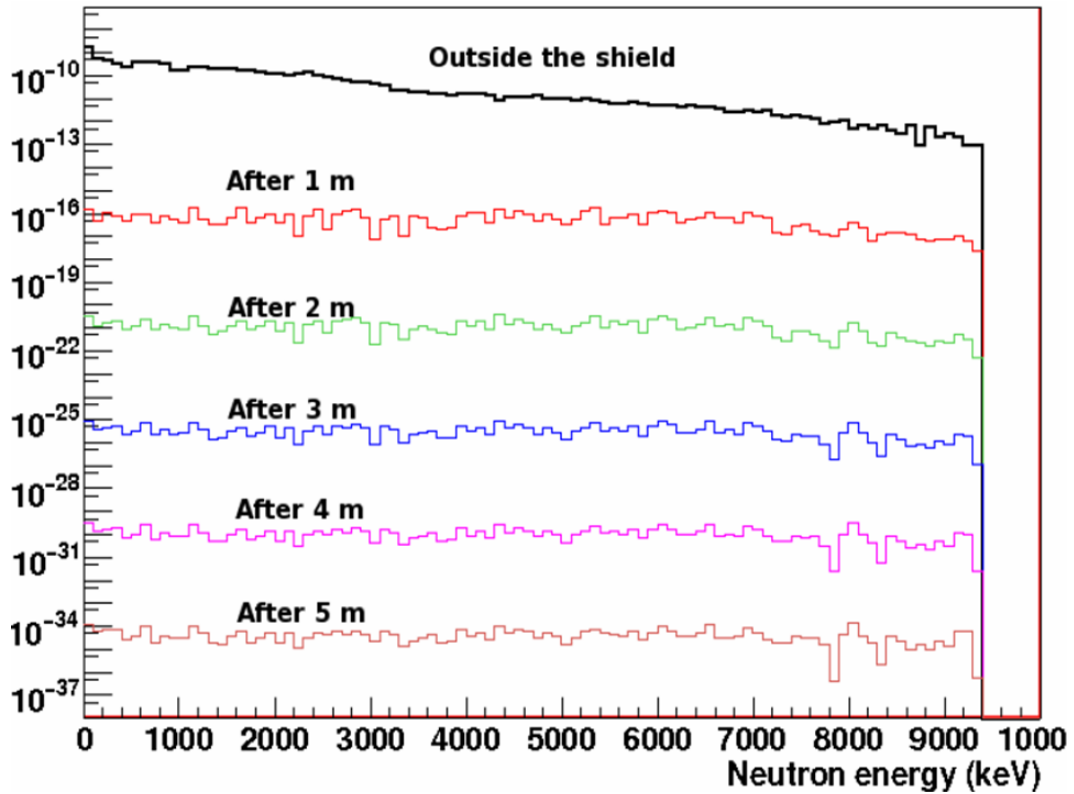


FIGURE 2.9: Flux of neutrons coming from the concrete measured in the HallB at LNGS (black line) and MonteCarlo simulation of the energetic spectrum of neutron for different thickness of the layer of water. [63].

LXe and among its daughters there is ^{214}Pb , a beta emitter. We require to have a Rn contamination inside the LXe less than $10 \mu\text{Bq/kg}$.

2.2.3.4 External background

The external background is due to different factors:

- Natural radioactivity: low energy ($< 10 \text{ MeV}$) γ and neutrons from the rock;
- Neutrons at high energy (up to the order of tens GeV) induced by the cosmic muons.

Both can be reduced surrounding the detector with a thick water layer, contained in the so called *Water Tank*. The layer of water is about four meters thick in each direction around the detector and, for gammas, it is equivalent to the shielding of 20 cm of lead. The presence of water allows a reduction of the γ flux of a factor 10^5 and makes negligible the contribution of neutrons produced in the (α, n) reaction induced by ^{238}U and ^{232}Th decay in the rock and concrete of the experimental hall (Fig. 2.9). As an example, one

meter of water is enough to lower the value of the neutron flux with energy in the scale of MeV of a factor 10^6 .

Neutrons induced by cosmic muons have an energy up to tens of GeV and they might cross the Water Tank, enter the TPC and mimic a WIMP-like interaction. This is the reason why the TPC is surrounded by a Water Tank instrumented with photo multipliers (PMTs): during their path in water muons emit light through Čerenkov effect. If a muon-like event is seen, a trigger is sent to the TPC, in this way it is possible to veto that specific event. This system is called Muon Veto.

A Monte Carlo simulation [62] showed that with 4 meters of water, up to the 99.5% of neutrons are moderated and stopped.

The last categories of neutrons are the ones produced by the interactions of muons with the materials of the detector. These neutrons, if the corresponding muons aren't detected in the Water Tank, are extremely dangerous. From the simulation it was also shown that the biggest part of this kind of neutrons is generated in the cryostat.

The total background expected from the Monte Carlo simulation is about 4 event in the 1 tonne fiducial volume in 2 years of exposure, mostly coming from the intrinsic Rn contamination [40].

The first Dark Matter search result, Fig. 2.10, demonstrates that XENON1T has the lowest low-energy background level ever achieved by a dark matter experiment, and currently the experiment continues to record data. The foreseen sensitivity, in $2 \text{ t} \times \text{y}$, is $1.6 \cdot 10^{-47} \text{ cm}^2$. After that the upgrade towards the XENONnT experiment is already planned. The goal is to achieve an order of magnitude in sensitivity, in 20 t.y. Preliminary studies have shown that while ER background from materials can be kept under control, the background from radiogenic neutron is not negligible in a large fiducial volume, as for the time of exposure of its predecessor (see next chapter). In this scenario, we have studied the impact of a Neutron Veto able to tag these background events.

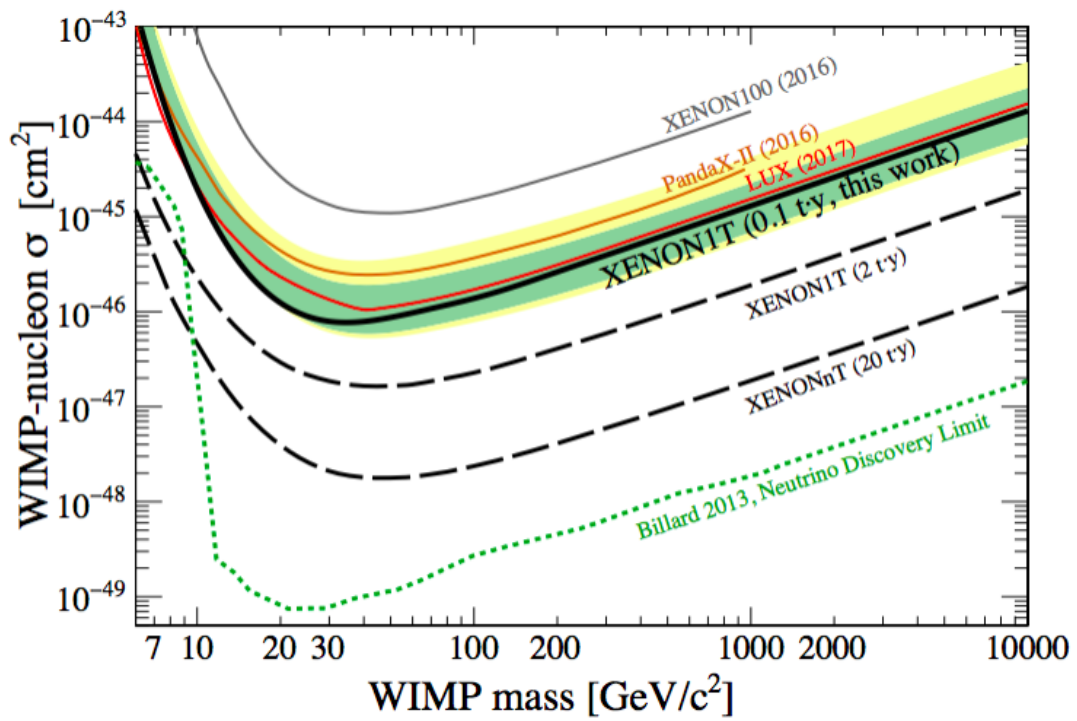


FIGURE 2.10: The spin-independent WIMP-nucleon cross section limits as a function of WIMP mass at 90% confidence level (black) for the first run of XENON1T. In green and yellow are the 1- and 2 σ sensitivity bands. Results from LUX (red), PandaX-II (brown), and XENON100 (gray) are shown for reference. The dotted lines represent the predictions for XENON1T in its complete exposure and for XENONnT.

Chapter 3

Description of the Monte Carlo Simulation

XENON1T has already achieved excellent results in its first science run [25]. In the nominal exposure of $2 \text{ t} \cdot \text{y}$ we expect to reach a sensitivity of $1.6 \cdot 10^{-47} \text{ cm}^2$. At the same time, it is already foreseen the next stage of the project. To achieve another order of magnitude in sensitivity, the XENON collaboration plans to build and install inside the same XENON1T outer cryostat a new detector, named XENONnT with about three times the active LXe mass and with even lower background. All other systems in XENON1T can handle a larger detector with a target mass of up to 10 t: cryogenics, purification, recovery, support structure, DAQ and Slow Control system, and the Muon Veto. Their established performance will enable the operation of XENONnT on a fast timescale.

With a LXe target mass of ~ 6 tons, compared to the current 2 tons, the sensitivity to spin-independent WIMP-nucleon elastic scattering cross sections can reach the value of $\sigma_{SI} = 1.6 \cdot 10^{-48} \text{ cm}^2$ in a $20 \text{ t} \cdot \text{y}$ exposure [64].

XENONnT will not only increase the WIMP sensitivity by an order of magnitude, but it will also probe with higher statistics a potential signal seen by XENON1T. Furthermore, it will open the possibility to probe other physics channels, such as the detection of solar ^8B neutrinos via coherent neutrino scattering or the search for the neutrinoless double beta decay in ^{136}Xe .

For the achievement of this upgrade, an intense *R&D* is carried out.

This thesis focuses on designing a Monte Carlo (MC) simulation to study the performances of a neutron veto for the future operation of the experiment. The MC simulation has been developed using **GEANT4** (**GE**ometry and **T**racking) version 9.5-patch01, a toolkit to simulate the effect of the passage of particles through matter [65].

Components of the framework relevant in the scope of this work are summarized in the next section. In the following sections the main part of the simulation are described. We first introduce the geometry of XENONnT and the study of radiogenic neutron background, which justifies the need of an active neutron veto. For this study, we have chosen to implement a neutron veto based on a Gd-loaded liquid scintillator (Gd-LS). The major advantage of this loading option is in increase of the neutron capture cross section and high energy yield. Finally, to complete the neutron veto system design, several arrangements of a dedicated array of PMTs and reflective foils are presented.

3.1 The GEANT4 framework

GEANT4 is an object-orientated toolkit, written in C++, that simulates the passage of particles through matter and their interactions. GEANT4 also uses the most up to date particle data such as nuclear cross sections, to provide accurate information for particle interactions within a system. It was selected in the present study because of its versatile geometry, material definition packages and graphic routines which enable on-line monitoring of the geometric details of the volumes and of the particle tracks.

A GEANT4 simulation process usually includes the following aspects:

- the geometry of the system;
- the materials involved;
- the fundamental particles of interest;
- the generation of primary particles for events;
- the tracking of particles through materials and external electromagnetic fields;
- the physics processes governing particle interactions;
- the response of sensitive detector components;
- the generation of event data;
- the storage of events and tracks;
- the visualization of the detector and particle trajectories;
- the capture for subsequent analysis of simulation data at different levels of detail and refinement;

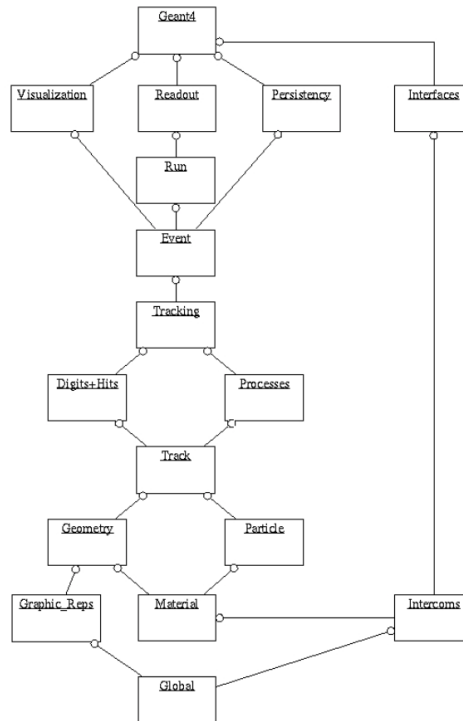


FIGURE 3.1: GEANT4 class categories.

To cover these aspects, there exist 17 class categories, that are used to create logical units. They are presented by a class category diagram, Fig. 3.1, in which each box represents a class category, and a “uses” relation by a straight line.

The main unit of simulation is the *event*, which represents the whole process of an incident particle from its emission from the particle source, through interactions with the target particles if applicable, to rest or leaving the detector system. A sequence of events which share the same detector conditions defines a *run*. It represents performing the simulation once. Within a run, users can not change the detector geometry and settings of physical processes. A *track* is a snapshot of a particle. It represents a temporary state of a particle at an instance within an event and includes information for position and physical quantities of the current state of the particle. An event consists of thousands of tracks.

When making a simulation using GEANT4, the user does not need to care about the details of every aspect shown above. There are interfaces for eight user classes provided by the framework, three of which are mandatory:

- **G4UserDetectorConstruction** defines detector material and geometry, including details about the chemical composition and the optical properties. Here a specific volume can be declared as a *SensitiveDetector* in order to create hits, or collections of the particle properties at every track.

- **G4VUserPhysicsList** provides information to register the particle type and their associated physics processes, and to set the production cuts of secondary particles, e.g., whether an optical photon shall be generated or not.
- **G4VUserPrimaryGeneratorAction** specifies the energy, direction, source dimensions, and type of the primary particles.

The other five base classes are not mandatory but necessary for user control. These classes contain methods that can be invoked at various stages of the simulation process (see Table 3.1). Users can write their own implementations of these methods to perform various actions, such as defining a histogram, analyzing the results, setting priority control to a track, storing particle trajectories, and terminating a track.

Optional class	User action	Time of invocation
<i>G4UserRunAction</i>	Define and store histograms	at the beginning and end of each simulation
<i>G4UserEventAction</i>	Event selection and analysis of simulation data	at the beginning and end of particle history
<i>G4UserStackingAction</i>	Customize priority of tracks	at the start of each history
<i>G4UserTrackingAction</i>	Decide whether a trajectory should be stored or not	at the beginning and end of each particle trajectory
<i>G4UserSteppingAction</i>	Kill, suspend, postpone a track	at the end of each step

TABLE 3.1: User action base classes and times of invocation of their associated class methods.

In GEANT4, there is also the possibility to call for the initialization of a *geantino*, a virtual particle which is used as a geometrical probe. It is only transported through the detector and does not interact with it, what makes the corresponding runs very “light” in terms of computing power. They have been used in this work to illustrate the simulated veto geometry.

3.2 XENONnT TPC geometry

XENONnT is conceived as a fast upgrade of XENON1T: infrastructure has been designed for a rapid deployment of an upgraded detector. The muon veto for XENONnT will be the same one currently used, furthermore the support structure and levelling system of XENON1T were designed to accommodate also an enlarged detector and the cryogenic system is able to handle an additional heat load. The GXe purification system is modular and scalable, and the Kr distillation column can fulfill XENONnT ^{85}Kr requirement (see section 2.2.3.3). Currently the LXe storage capacity is of 7.6 tons, which is enough for the $\sim 6 - 7$ tons hypothesized for XENONnT.

At the time of this thesis, the collaboration has fixed the final geometry for the XENONnT proposal (see Fig. 3.2). This geometry maximizes the dimensions of the TPC, with the constrain to fit the current external cryostat. The main geometrical characteristics are reported in Table 3.2.

	Draft-Design
TPC diameter (mm)	~ 1368
TPC height (mm)	1446
Active LXe (t)	~ 6
Total LXe (t)	~ 7
Cryostat (kg)	1600
PTFE (kg)	170
Total number of PMTs	476 (top 223, bottom 253)

TABLE 3.2: Reference dimensions of XENONnT detector.

3.2.1 Event selection in the TPC

A WIMP is expected to scatter only once in the central volume of LXe TPC, depositing a few keV with no simultaneous energy deposit in surrounding materials. Neutrons from material radioactivity, which can fake WIMP interactions when they scatter elastically, are likely to interact again either within the TPC or nearby, due to their short path (~ 15 cm). This can be used as handle to flag them as background events.

The criteria applied to select background events for this study are:

- single scatter nuclear recoils in the LXe or multiple scatters but with the second largest S2 signal being smaller than 100 PE (about 5 drifted electrons);
- energy deposits in TPC between 4 and 50 keV;
- 4t fiducial volume, as the minimum assumed volume for XENONnT operation;

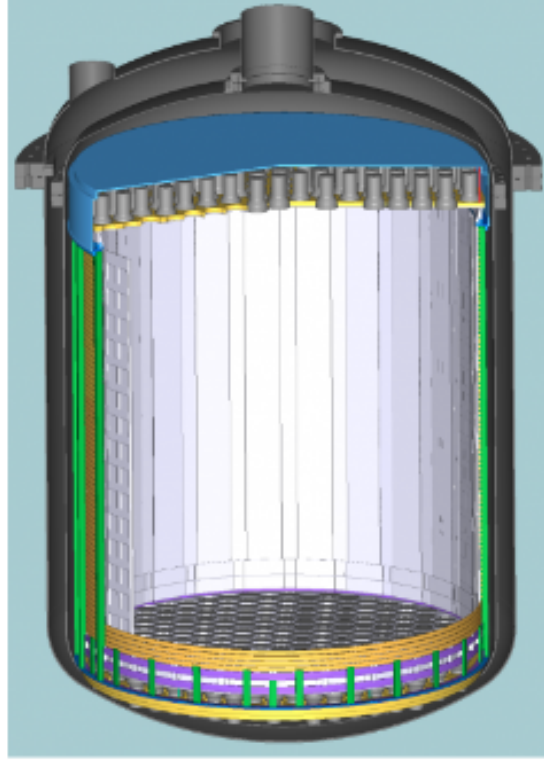


FIGURE 3.2: View of the XENONnT TPC inside the cryostat.

The first cut is based on the performances of XENON100 and XENON1T: the spatial reconstruction of an event allows to distinguish single and multiple scatters with a separation larger than ~ 3 mm along the Z direction [51]. Indeed, when two scatters take place with a separation in $z < 3$ mm, the S2 signal obtained is the superimposition of two S2s, so can not be distinguished. In addition, if the second largest S2 is smaller than a fixed threshold (corresponding to 5 extracted electrons), the event is considered as a single scatter.

In the next section we are going to introduce the radiogenic neutron background predicted with these selection cuts.

3.2.2 Radiogenic Neutron background

In XENON1T, the main contribution to NR backgrounds is due to radiogenic neutrons which produce a background rate of $(0.6 \pm 0.1) \text{ y}^{-1}$ in 1 t FV [40]. The presence of isotopes of the primordial decay chains ^{235}U , ^{238}U and ^{232}Th in the materials of the detector generates radiogenic neutrons in the MeV range through spontaneous fission (SF), mainly from ^{238}U , and (α, n) reactions induced by various α particle emitted along the

decay chains. These neutrons will be present regardless of the amount of shielding used, but they can be reduced, though not completely eliminated, through careful material selection. In Fig. 3.3, the contamination of the materials considered for the XENONnT NR background estimations is reported.

Component	Material	Quantity	Unit	Contamination [mBq/unit]				
				^{238}U	^{235}U	^{226}Ra	^{232}Th	^{228}Th
Cryostat shells	SS	1060	kg	2.4 (7)	$1.1 (3) \cdot 10^{-1}$	$< 6.4 \cdot 10^{-1}$	$2.1 (6) \cdot 10^{-1}$	$< 3.6 \cdot 10^{-1}$
Cryostat flanges	SS	540	kg	1.4 (4)	$6 (2) \cdot 10^{-2}$	< 4.0	$2.1 (6) \cdot 10^{-1}$	4.5 (6)
TPC panels ¹	PTFE	170	kg	$< 2.5 \cdot 10^{-1}$	$< 1.1 \cdot 10^{-2}$	$< 1.2 \cdot 10^{-1}$	$< 4.1 \cdot 10^{-2}$	$< 6.5 \cdot 10^{-2}$
TPC plates	Cu	448	kg	< 1.2	$< 5.5 \cdot 10^{-1}$	$< 3.3 \cdot 10^{-2}$	$< 4.3 \cdot 10^{-2}$	$< 3.4 \cdot 10^{-2}$
PMT stem	Al_2O_3	476	PMT	2.4 (4)	$1.1 (2) \cdot 10^{-1}$	$2.6 (2) \cdot 10^{-1}$	$2.3 (3) \cdot 10^{-1}$	$1.1 (2) \cdot 10^{-1}$
PMT window	Quartz	476	PMT	< 1.2	$< 2.4 \cdot 10^{-2}$	$6.5 (7) \cdot 10^{-2}$	$< 2.9 \cdot 10^{-2}$	$< 2.5 \cdot 10^{-2}$
PMT SS	SS	476	PMT	$2.6 (8) \cdot 10^{-1}$	$1.1 (4) \cdot 10^{-2}$	$< 6.5 \cdot 10^{-2}$	$< 3.9 \cdot 10^{-2}$	$< 5.0 \cdot 10^{-2}$
PMT body	Kovar	476	PMT	$< 1.4 \cdot 10^{-1}$	$< 6.4 \cdot 10^{-3}$	$< 3.1 \cdot 10^{-1}$	$< 4.9 \cdot 10^{-2}$	$< 3.7 \cdot 10^{-1}$
PMT bases	Cirlex	476	PMT	$8.2 (3) \cdot 10^{-1}$	$7.1 (16) \cdot 10^{-2}$	$3.2 (2) \cdot 10^{-1}$	$2.0 (3) \cdot 10^{-1}$	$1.53 (13) \cdot 10^{-1}$

FIGURE 3.3: Contamination of the materials considered in this work for the XENONnT NR background simulations.

Simulating 10^7 neutrons produced from each of the neutron source listed, applying the above-mentioned criteria of event selection in the TPC, and then scaling the results by the neutron yield of the material and the contamination of the component, the total XENONnT NR radiogenic background rate obtained is 1.1 ev/y in 4 t FV, as shown in Fig. 3.4 in the case of [4-50] keV deposited energy range in the TPC.

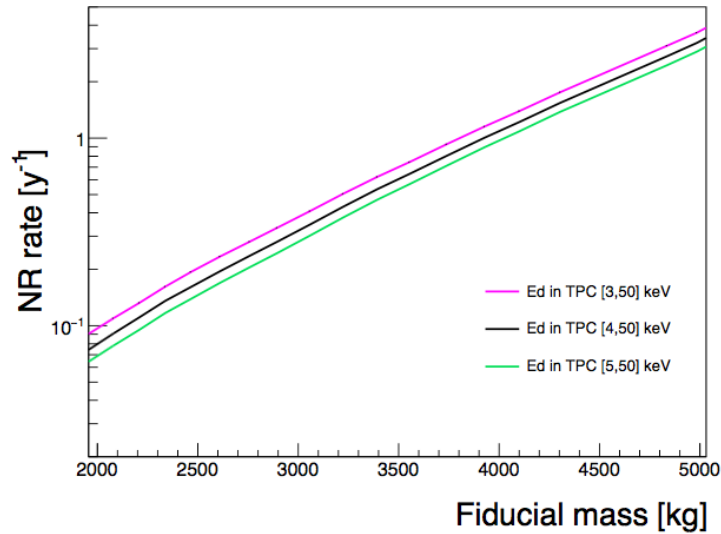


FIGURE 3.4: Radiogenic neutron background rate (ev/y) as function of the fiducial mass.

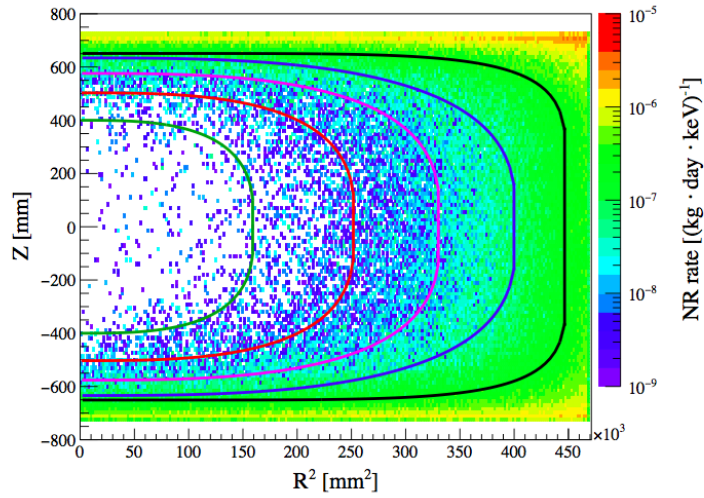


FIGURE 3.5: Distribution of the radiogenic neutron background events inside the active volume $[(\text{kg day keV})^{-1}]$. The 1 to 5 t FVs are drawn as enclosed by a superellipsoid.

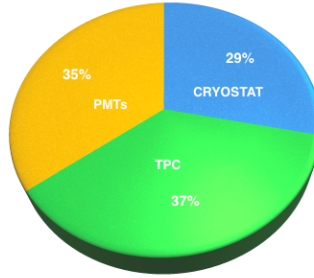


FIGURE 3.6: Contributions from the different simulated components to the NR background.

Figure 3.5 shows the spatial distribution of background events for three different energy ranges of recoiling deposits over the whole sensitive LXe volume.

The largest fraction of neutron background events comes from the PTFE of the TPC panels (30.2%), followed by the cryostat shells (20.4%) and the PMTs (mostly from the ceramic steam (20.9%)). The global contributions from PMTs, Cryostat and TPC are represented in Fig. 3.6.

Hence, in the whole 20 t·y exposure foreseen for the XENONnT, we expect about 5 background events from radiogenic neutrons. This opens the need to study the reduction of this source of background. One possibility is a neutron veto that would be able to detect these neutrons when they leave the detector and efficiently reduce this background.

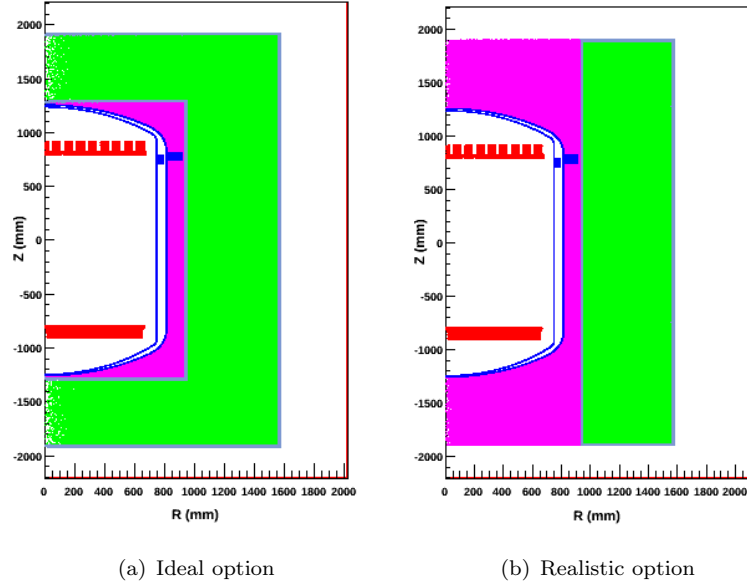


FIGURE 3.7: Sketch of the components of the *ideal* and *realistic* options for the XENONnT neutron veto geometry. In blue the Cryostat, in red the PMTs, in purple the “displacer” volume, in green the Gd-LS, in gray the acrylic vessel.

3.3 Neutron Veto conceptual design

This section describes the implementation and the design optimization of three configurations of the XENONnT neutron veto named *ideal*, *realistic* and *modular* option. The veto simulation has been incorporated with the existing XENON1T detector simulation, and adapted for the XENONnT geometry. As the detector medium, a gadolinium-loaded linear-alkylbenzene (LAB) has been chosen. LAB is an organic LS solvent that has become very popular in the past years, mainly due to its superior safety features, good material compatibility and high transparency. The conceptualization of the simulated XENONnT neutron veto mixture has followed the references of operative neutrino experiments employing Gd-LS with LAB as a solvent, like, e. g., Daya Bay [66] and RENO [67].

3.3.1 Detector configurations

Figure 3.7 shows a schematic view of the neutron veto ideal (a) and realistic (b) design.

The *ideal* option consists of a hermetic non-segmented cylinder of LS around the outer cryostat, within the water tank. The veto thickness is the same in all the walls and values from 40 to 60 cm have been tested, determined by the γ scattering length (~ 25 cm) and the mechanical constraints of the already existing XENON1T support structure. This option is impossible to achieve in practice because of the penetration of the main

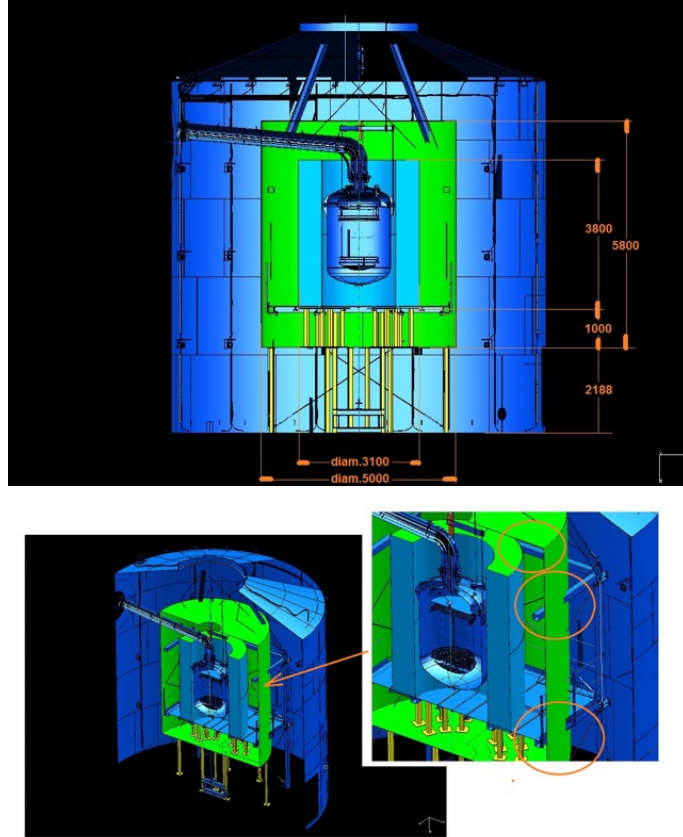


FIGURE 3.8: CAD view of the XENONnT neutron veto for the *realistic* option.

pipe connected to the cryostat, and the feedthrough aimed for the operation of the anti-buoyancy system attaching the outer cryostat to the bottom of the water tank as well as the calibration belts. To get a more realistic geometry, in the second configuration only side vessels are taken into account while top and bottom vessels are completely eliminated. This configuration is described in the CAD drawing shown in Fig. 3.8.

A different approach, mainly suggested from mechanical considerations, is the *modular* option consisting of 32 identical $0.8(\text{H}) \times 1.5(\text{W}) \times 0.7(\text{D}) \text{ m}^3$ stainless steel boxes, containing water and an acrylic vessel filled with $0.8 \times 0.6 \times 0.6 \text{ m}^3$ of LS, see Fig. 3.9.

In each option, acrylic vessels are chosen to contain the liquid scintillator, as used in the reference experiments for the veto design [66][67]. Their main advantages are a high UV transparency and an excellent compatibility with LAB. To ensure pressure stability between the vessels and the surrounding water volume, a wall thickness of the vessels of 2.54 cm has been implemented. This thickness as well as acrylic vessels have been implemented in all the configurations. To fill in the gaps between the outer cryostat and the acrylic vessel, a low-density “displacer” has been implemented: studies have been performed with three different material such as water, a closed-cell polyurethane foam ($\text{C}_{25}\text{H}_{42}\text{N}_2\text{O}_6$) and vacuum.

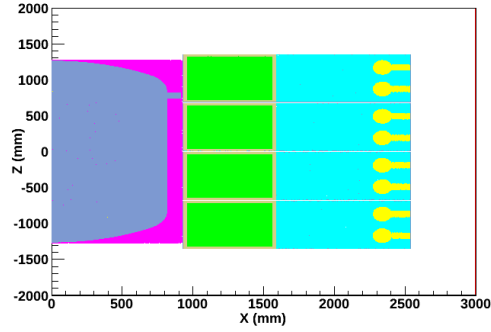


FIGURE 3.9: Sketch of the components of the *modular* options for the XENONnT neutron veto geometry. In grey the Cryostat; in purple the “displacer” volume; in green the Gd-LS; in ochre the acrylic vessel.

In the simulation, the LS volume operate as a sensitive detector, together with the LXe, through dedicated GEANT4 classes. Every track in a sensitive detector is recorded in the simulation output, hence for a single event variables such as the energy deposit and the position of every interaction are recorded and correlations between the sensitive volume of the TPC and the neutron veto can be established.

3.3.2 Gadolinium-loaded liquid scintillator

The baseline mixture for the simulation purpose consists of a 0.1% Gd-loaded liquid scintillator (Gd-LS), with a proportion of 3 g/l of 2,5-diphenyloxazole (PPO) as a primary fluor and 15 mg/l of 1,4-bis(2-methylstyryl)benzol (bis-MSB) as the secondary one¹. As a solvent, we have chosen the linear-alkylbenzene (LAB), a hydrocarbon chain with one benzene ring attached (Fig.3.10). LAB is preferable as detection medium with respect to other scintillator due to its high flash point, low chemical reactivity, and light-yield comparable with e.g. pseudocumene.

Gadolinium is not found as a free element in nature, but it is contained in many rare minerals. It reacts slowly with water and dissolves in acids, and can form stable organometallic complexes. It is generally difficult to dissolve inorganic Gd salt in organic solvent. As reported by the Daya Bay and RENO experiments among others, 3,5,5-trimethylhexansaeure (TMHA) is a very favoured candidate to enhance LAB with Gd, with proven stability of the doped mixture for several years.

When a neutron enters the LS from the LXe TPC, there are two signals that can be used to detect and veto the neutron. The first signal is the prompt thermalization signal produced by the neutron slowing down in the LS. Neutrons lose energy by scattering off the nuclei in the scintillator, mostly on hydrogen and carbon. Monte Carlo simulations

¹This type of mixture was used and described by CHOOZ [68], Palo Verde [69], and Daya Bay [66]

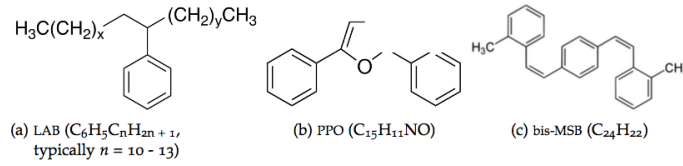


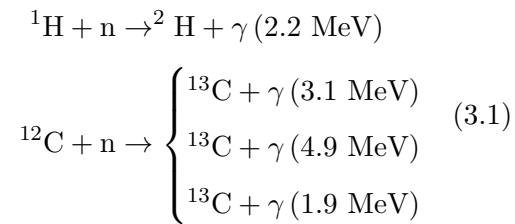
FIGURE 3.10: Structural formulas for the organic components of the implemented LS mixture.

have shown that the thermalization signal follows the signal in the LXe TPC very quickly, in the order of ns. The second signal is the delayed signal from the neutron capture: after a diffusion time of the few μs , the thermalized neutron can be captured on various isotopes in the scintillator mixture, typically on a time scale on the order of 1-100 μs . In Table 3.3, the neutron capture cross sections for the nuclei present in the Gd-LS mixture are listed.

Isotope	Natural abundance [%]	σ_{capture} [barn]	B [keV]
^1H	99.99	$3.33 \cdot 10^{-1}$	2224.58
^2H	0.01	$4.92 \cdot 10^{-4}$	6257.25
^{12}C	98.93	$3.89 \cdot 10^{-3}$	4946.31
^{13}C	1.07	$1.22 \cdot 10^{-3}$	8176.61
^{152}Gd	0.20	$7.35 \cdot 10^2$	6247.48
^{154}Gd	2.18	85	6435.29
^{155}Gd	14.80	$5.17 \cdot 10^4$	8536.04
^{156}Gd	20.47	1.8	6360.05
^{157}Gd	15.65	$2.15 \cdot 10^5$	7937.39
^{158}Gd	24.84	2.2	5943.29
^{160}Gd	21.86	1.4	5635.4

TABLE 3.3: Neutron capture cross section, natural abundance and neutron binding energy for the nuclei of Gd-LS.

The neutron capture reaction can occur on hydrogen or carbon present in the LS, through the following reactions



The cross sections of these reaction are small and the γ -ray is in (or close) the energy range of natural radioactivity, which extends to 2.6 MeV. Adding gadolinium to the scintillator, the process follows the reaction



This has two important advantages. First, the (n,γ) cross-section for natural Gd is 49000 barn (with major contributions from the $^{155,157}\text{Gd}$ isotopes), thus only a small concentration of Gd is necessary. Secondly, a release of a high-energy (8 MeV) gamma cascade after thermal neutron capture on Gd results in a neutron capture signal well above the radioactivity backgrounds. Furthermore, the neutron capture time is significantly shortened in a Gd-loaded LS, with respect to that in a pure hydrocarbon-based scintillator.

To detect the low-neutron background with high efficiency, the Gd-LS must have the following key properties:

- Long optical attenuation length, > 10 m at 430 nm
- High light yield, 9000 photons/MeV;
- Ultralow impurity content, mainly of the natural radioactive contaminants, such as U and Th;
- Long-term chemical stability, over the lifetime of the experiment.

All of these properties have been achieved on a large scale for the Daya Bay experiment. In Table 3.4 are summarized the assumption adopted in this work on the optical properties of Gd-LS in the simulations.

The mixture has been defined following the GEANT4 procedures i.e. providing the density, the number of materials with the corresponding mass fraction and the state of the compound in natural conditions.

	Scintillator	Acrylic
Density (g/cm^3)	0.863	1.18
Refractive index	1.50	1.51
Absorption length at 430 nm (m)	30	1
Scattering length (m)	27	1

TABLE 3.4: Some properties of scintillator and acrylic implemented in the simulation.

3.3.3 Gadolinium neutron-capture in GEANT4

As reported in [70], for the default final state model of GEANT4, the MC modeling of the multiplicity and the energy of Gd de-excitation gamma rays does not match the data available on the measured process. When a ^{155}Gd or a ^{157}Gd absorb a neutron they are excited into the continuum energy levels of the nucleus, and the decay from there to the discrete energy levels seems difficult to be modeled. For the *final state* model Gd

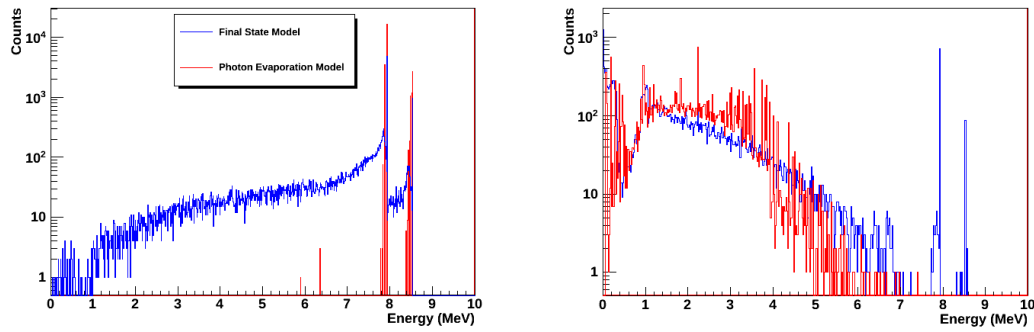


FIGURE 3.11: (Left) Total capture energy spectrum produced in a Gd de-excitation for the final state and the evaporation model. (Right) Individual gamma capture energy spectrum for the evaporation (red) and final state (blue) models.

de-excitations is inadequate, since they often liberate an amount of energy far from the expected Q-value. As an alternative to solve this issue GEANT4 offers the *evaporation model*, which does conserve energy and can be enabled by simply activating a particular flag before initializing the run.

In order to compare the performances of both models, for each of them a set of 10^6 neutrons has been generated from the PMTs of the TPC, distributed in a flat energy spectrum from 0 to 10 MeV. In Fig. 3.11 (Left) the total capture energy spectrum produced in a Gd de-excitation for the final state and the evaporation models is shown; the evaporation model correctly reproduces the Q-value of the reaction. In Fig. 3.11 (Right), for the same set of events also the energy of the single gammas for a neutron capture on Gd have been visualized.

While the final state model predicts an excess of gamma rays in some cases, the prediction for the evaporation model also seems slightly incorrect, since more single gamma ray de-excitations are expected. However, our detector should be large enough to hold both captures and secondary particles thus should be more sensitive to the total energy deposited, i.e. the Q-value. For this reason the evaporation model has been chosen.

3.4 Photomultiplier System

The scintillation light is detected by extra arrays of PMTs (in addition to those of the water tank) that complete the conceptual design of the veto system. A dedicated structure contains the veto PMTs and the water where they are immersed. Different arrangement models have been tested with the goal of enhancing the photocoverage of the neutron veto. For the *ideal* and *realistic* option, three geometric models of the PMTs array have been explored, by varying the number of PMTs and reflective foils. In

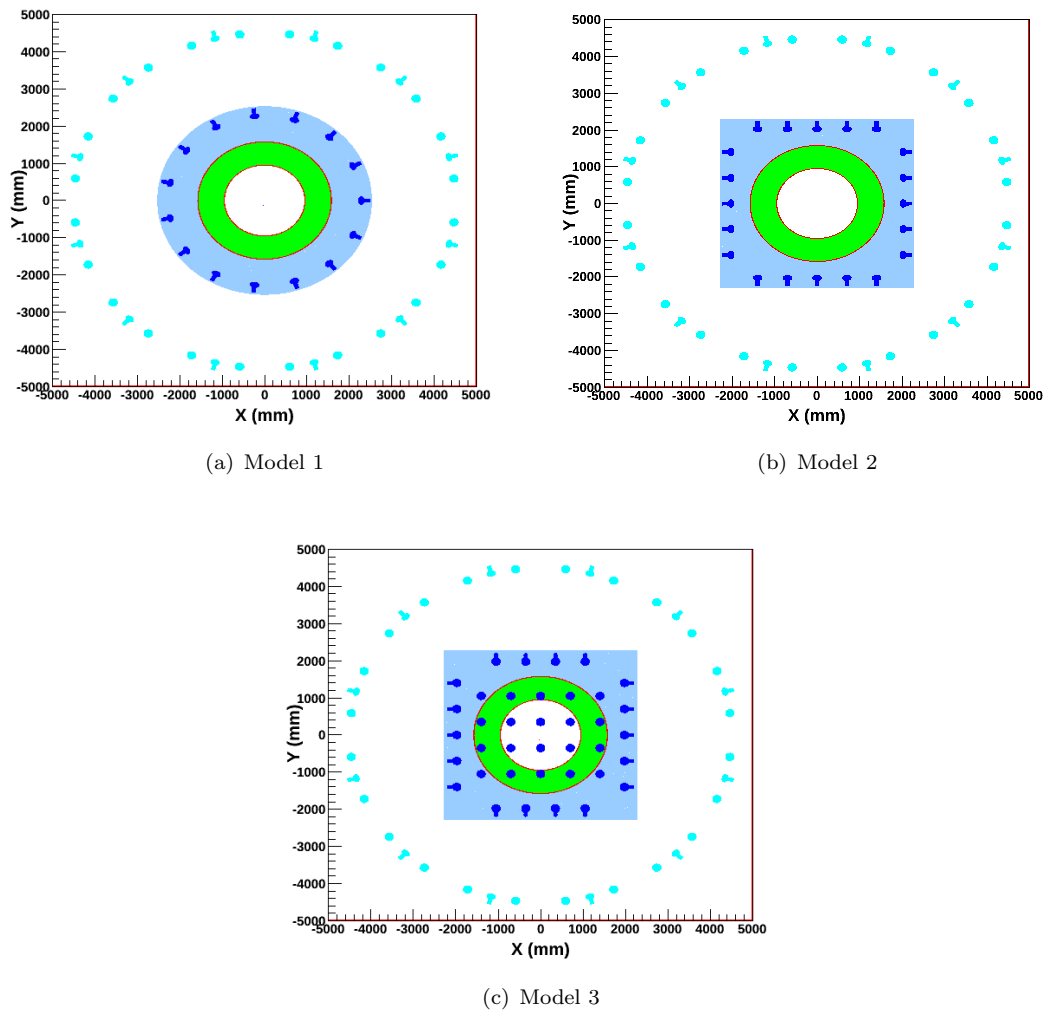
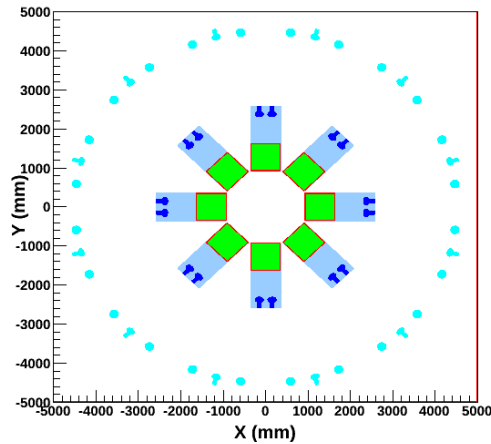


FIGURE 3.12: The xy placement of the muon veto PMTs in the tank (light blue), along with a planar section of 60 cm thick LS in the *ideal* option geometry (green), and the acrylic vessels (red) at around $z = 0$ (center of the TPC). The position of an extra veto PMT array (dark blue) 70 cm away from the veto vessels is also shown.

Fig. 3.12, obtained by generating geantinos from the represented volumes in GEANT4, the xy placement of the muon veto PMTs in the tank is shown (in light blue) along with the neutron veto PMTs (in blue). The figure also shows the position of the implemented reflective foils. The possibility to use reflective surface was investigated in order to enhance the amount of light that the PMTs of the neutron veto can collect. Studies have been done with one reflective foil covering the acrylic surface of LS in contact with the displacer, or adding a second reflective foil on the inner surface of the PMTs support structure.

Concerning the *modular* option, we have studied a configuration with four PMTs in each box, Fig. 3.13, that is the maximum number that the designed box structure can contain. Also here, the PMT faces are positioned 70 cm from the LS wall. In the next

FIGURE 3.13: The xy view of the *modular* option.

chapter will be presented the results of the light collection efficiency simulations for these configurations.

3.4.1 Photomultiplier Tubes and reflective foil

The simulated PMTs are the same used in the XENON1T muon veto system: the high quantum efficiency (HQE) 8" Hamamatsu R5912ASSY, which have already demonstrated excellent performances.

These PMTs have a bialkali photocathode and borosilicate glass window. Ten dynodes provide a typical gain of 10^7 at a working voltage of ~ 1500 V. The quantum efficiency (QE) is about 30% in the range [300-600] nm (Fig.3.14 left), and the collection efficiency (CE) is 85%, as declared by the manufacturer [71].

As reflective foil, the DF2000MA daylighting film has been implemented in GEANT4 code: this type of foil is already present on the inner walls of the water tank. It provides a very good reflectivity (more than 99% between ~ 400 and ~ 1000 nm, as we can see in Fig.3.14 (right)).

In the simulations a 30% QE and a 85% CE for the 8" PMTs and a conservative value of 95% of reflectivity are assumed.

3.4.2 Optical photon simulation

In GEANT4, optical photons (including also UV photons) are treated as a class of particle distinct from their higher energy gamma cousins. This implementation allows the wave-like properties of electromagnetic radiation to be incorporated into the optical

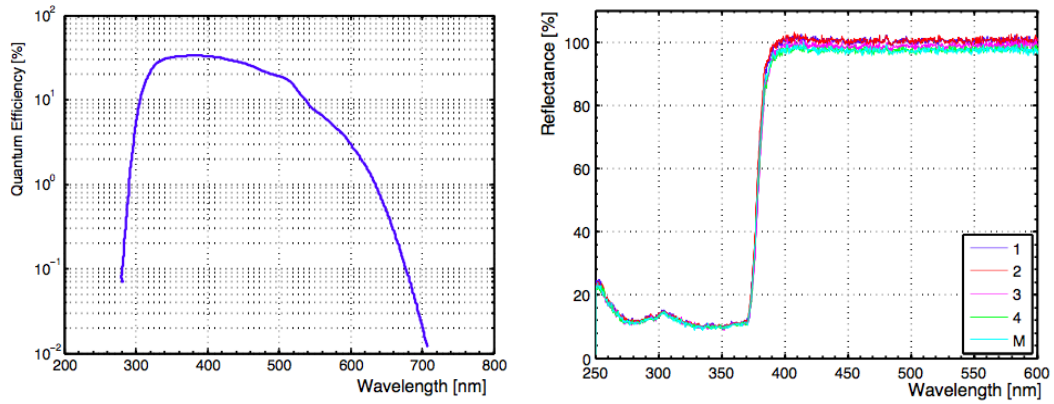


FIGURE 3.14: (Left) Quantum efficiency of one of the HQE Hamamatsu PMTs R5912ASSY. (Right) Specular reflectivity measurements of DF2000MA in different positions on the surface of a square shaped foil sample (Edges: 1-4, Middle: M).

photon process. The GEANT4 catalogue of processes at optical wavelengths includes refraction and reflection at medium boundaries, bulk absorption and Rayleigh scattering. We briefly recall each process and how it is coded in GEANT4:

Reflection The most frequent process inside the TPC for optical photons is the reflection. In GEANT4, reflection at an interface between two adjacent media is treated differently according to the materials. For the simple case of a perfectly smooth interface between two dielectric materials, all the user needs to provide are the refractive indices of the two materials stored in their respective *G4MaterialPropertiesTable*. In all other cases, the optical boundary process relies on the concept of *surfaces*. The information is split into two classes. One class, in the material category, keeps information about the physical properties of the surface itself, and a second class, in the geometry category, holds pointers to the relevant physical and logical volumes involved and has an association to the physical class. The former is called a **border surface** while the latter is referred to as the **skin surface**. This second type of surface is useful when a volume is coded with a reflector and is placed into many different mother volumes [65].

Rayleigh Scattering The Rayleigh scattering is the elastic scattering of light by particles much smaller than the wavelength of the radiation. Rayleigh scattering results from the electric polarizability of the particles. The oscillating electric field of a light wave acts on the charges within a particle, causing them to move at the same frequency. The particle therefore becomes a small radiating dipole. We see the radiation as scattered light [65].

Absorption An other important process for optical photon is the absorption. It determines the lower limit in the window of transparency of the radiator. The implementation in the code of bulk absorption, *G4OpAbsorption*, is trivial. The process merely kills the particle. The procedure requires the user to fill the relevant *G4MaterialPropertiesTable* with empirical data for the absorption length, which is the average distance traveled by a photon before being absorbed by the medium.

To enable these processes one needs to assign values for the absorption length, the Rayleigh scattering length and the refractive index of all the involved materials at different wavelengths. The water properties are already well defined in the code because they are the same of the existing muon veto system. For the acrylic and the Gd-LS, the optical values implemented in the simulation are summarized in Table 3.4.

Chapter 4

Analysis and Results

This chapter is dedicated to describe the performances of a neutron veto and its efficiency to reject radiogenic neutron background events.

The first section shows the main features of thermalization and capture of neutrons in the scintillator. In the second section we evaluate the light collection efficiency of the veto using the arrangements of PMTs arrays shown in the previous chapter. Then the veto response to neutron background events is studied and the photoelectrons (PEs) yield of the scintillator for the three proposed geometries is derived.

Using these results we obtained the efficiency of the veto system for the three different configurations. The last section of this chapter is dedicated to the evaluation of the impact of a neutron veto on the radiogenic neutron background rate of XENONnT.

4.1 Neutron thermalization and capture

Before being captured, the neutron needs to be thermalized in the surrounding detector medium. In the thermalization process, multiple inelastic and elastic neutron scatters can take place in rapid succession. After the neutron has lost most of its energy through multiple scatters, it diffuses within the scintillator until it is captured by Gd or H, or escapes from the detector. After capture on Gd, a total energy of about 8 MeV is emitted as a burst of several gamma rays, which then interact in the LS.

In this first analysis, 10^7 neutrons from a flat energy spectrum (1-10 MeV) were generated isotropically starting from TPC PMTs. The results are shown only for the *ideal* option with a 60 cm veto thickness, varying the displacer materials (vacuum, foam and water).

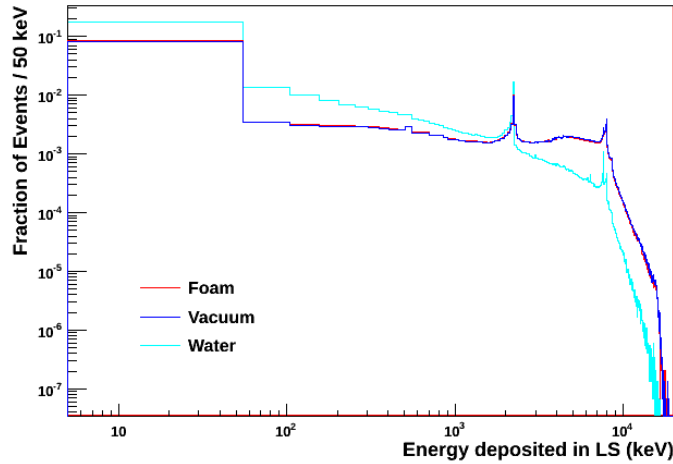


FIGURE 4.1: The distribution of energy deposits in the LS for all neutrons generated for different displacer materials. The peak observed at 2.2 MeV is due to emitted gamma-ray from neutron capture onto hydrogen.

4.1.1 Energy spectra in LS

As first step we studied the energy deposited in LS due to the captures. The simulated energy spectrum of the neutron capture for different displacer materials is reported in Fig. 4.1. All the obtained spectra show the two peaks corresponding to neutron captured by H and Gd, whose energy is ~ 2.2 MeV and ~ 8 MeV, respectively. The spectrum accounts not only for the neutron captures in LS, but also of the energy contribution in LS from neutrons captured elsewhere. Events depositing zero energy in the LS are included in the first bin of the distribution and an energy tail beyond 8 MeV is observed, accounting for elastic scatterings during thermalization or Compton scattered gamma rays.

The energy spectra obtained using foam and vacuum as displacer material are very similar. On the other hand, by using water the energy deposit of the veto severely decreases. Indeed, in this latter case neutrons thermalize in water displacer and then they are easily captured on H in the water buffer before reaching the LS.

In these spectra both the energy deposited by gamma and electrons elastic scattering (ER) and by proton scattering (NR) in the LS have been recorded. However, protons are treated separately with respect to gammas and electrons, because the light yield of NR is reduced with respect to ER due to quenching.

A formalism in which the scintillation-light yield (LY) of highly ionizing particles depends not only on the energy of the particle but also on its stopping power in specific materials was developed by Birks [72]:

$$\frac{dL}{dr} = \frac{A \frac{dE}{dr}}{1 + kB \frac{dE}{dr}} \quad (4.1)$$

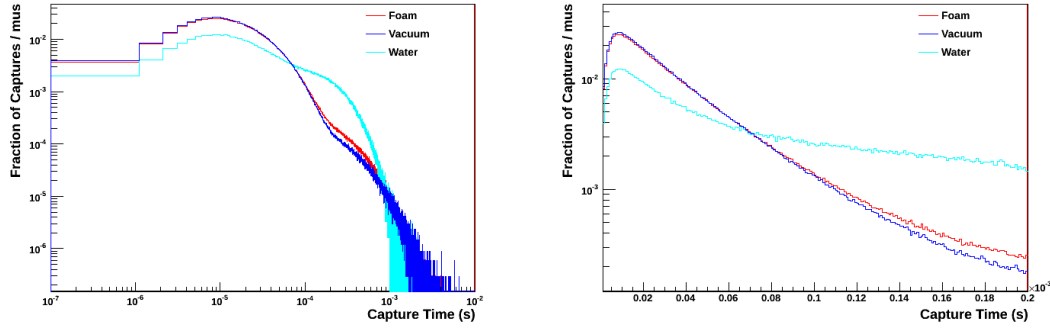


FIGURE 4.2: The simulated distributions in time of the neutron captures in the LS, since the production time of neutrons.

where $\frac{dL}{dr}$ is the scintillation yield per unit path length r , S is the absolute LY, kB denotes the quenching parameter, which varies for different particles and scintillator materials. These losses of linearity in the scintillation response happens when an ionizing particle travels through a scintillator ionizing the molecules in its path. These ionized molecules are considered as damaged and do not participate in the fluorescence process, although there can be light emission when the molecular ion recombines with an electron. To take into account this fact in our simulations, a variation of Birks semi-empirical law has been implemented:

$$\Delta E_{quench} = \frac{\Delta E}{1 + kB \frac{dE}{dx}} \quad (4.2)$$

In each step, the true energy deposited via ionization ΔE is registered and corrected using 4.2 given the quenched step energy deposition. Then, the total quenched energy of the event is determined by summing the quenched energy for all steps. In this study, the Birks' constant for protons is taken equal to $kB = 0.126 \text{ mm/MeV}$, as in [67].

4.1.2 Time and spatial distribution of neutron captures

For the same simulated data set, the neutron capture radial position and time distributions have been extracted and are shown in Fig. 4.2 and Fig. 4.3. The time distributions have been fitted using an exponential function; Table 4.1 reports the obtained mean capture times and radii for different displacers. As can be observed from table the mean time varies from $30 \mu\text{s}$ (foam or vacuum displacers) to $80 \mu\text{s}$ (water displacer).

The fit to the data has been performed excluding the first part of the spectra which does not completely agree with the exponential behavior; the first bins of the spectra are affected by events with an insufficient time for the fastest neutrons reaching the LS to become thermal and get captured.

Concerning the spatial distribution, up to 100 cm the trend is due to the capture that occur in the top and bottom vessels of the LS. The position of the peak indicates that

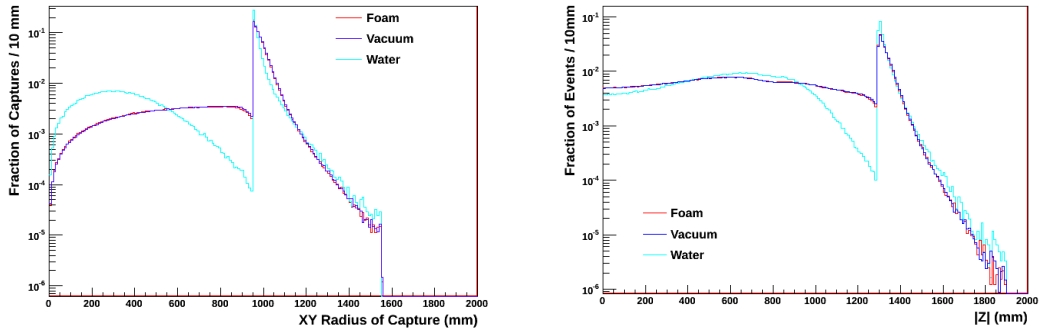


FIGURE 4.3: The simulated distributions in radius and z position of the captures of neutrons in the LS.

most of the capture occur in the sides of the scintillator within a few centimeters. This latter fact has triggered the study of the neutron veto efficiency for smaller thicknesses of the vessels, the results of which are presented at the end of the chapter.

Also here, in the case of water displacer, neutrons spend much time in the buffer to thermalize and when they reach the LS, are captured after few centimeters.

	Time (μs)	xy-Radius (cm)
vacuum	28.8	6.14
foam	29.1	6.02
water	81.2	4.85

TABLE 4.1: Time and radius of the neutron captures obtained from an exponential fit to the simulated data for the three displacers in the ideal geometry LS.

These distributions do not correspond exactly to the observable distributions in the veto event. Two main factor contribute to this difference: first, capturing a neutron does not necessarily result in a veto signal at the point of capture (especially in pure scintillator). Instead, the produced secondary particles, particularly gamma rays travel some distance before depositing a detectable amount of energy in the scintillator. Second, it is possible that the neutron deposits sufficient energy via nuclear recoils to produce a veto signal before being captured. As this recoils occur promptly, the recoil-induced veto signals can occur significantly earlier than the capture signals.

To investigate these effects, some energy deposit thresholds were defined and the time for which this deposit is first achieved in a single event inside the LS was calculated. Fig. 4.4 shows the time at which the first veto trigger associated with each neutron event is recorded. The x-axis has been changed relative to Fig. 4.2 to emphasize the prompt veto events created by nuclear recoils during neutron thermalization.

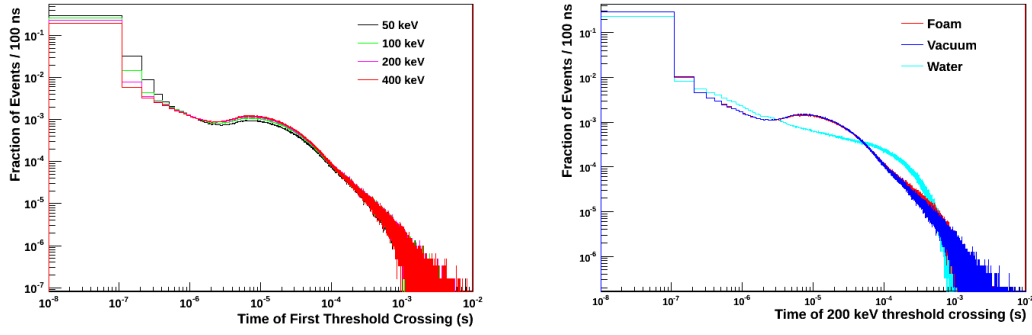


FIGURE 4.4: Distribution of times of first threshold crossing in LS for different thresholds (left) and for a fixed threshold of 200 keV with different displacer materials (right).

An energy deposit of 200 keV in LS could be set as a conservative energy threshold in order to be above the carbon-14 β -decay spectrum (~ 186 keV). By making an exponential fit on the tails of Fig. 4.4 we can evaluate the mean time at which this energy is first achieved for the three displacer materials. We have found that the difference between the mean capture time and times of first cross threshold is almost negligible for all the displacers; this happens when dealing with actual captures in the LS, but becomes relevant when the vetoed event has been captured elsewhere. One of the main channel for this process is the backscatter of neutrons from the LS into other volumes, which produces a delay in the subsequent capture and the ionization of the products reaching the LS.

The obtained results provide us a complete picture of the neutron behavior inside the proposed LS veto system.

4.2 Light Collection Efficiency

Light collection efficiency (LCE) constitutes one of the two building blocks in estimating the detector efficiency. Merged with the map of energy deposition it will define the photoelectron (PE) signal seen in the veto, and thus the capability to effectively detect neutrons in the LS. The calculation has been done through in two separate steps (energy deposition, and light generation) to save computing time, given the large amount of optical photons generated after a neutron capture on Gd (orders of 10^5 per event).

This study has been done with runs of 10^7 optical photons isotropically distributed in the LS volume for each of the veto PMT arrangements specified in the next sections. The LCE is thus calculated over the whole volume as

$$LCE = \frac{N_{detected}}{N_{generated}} \quad (4.3)$$

and for each individual R^2, Z pixel using the axial symmetry of the acrylic vessels around the cryostat:

$$LCE(R^2, Z) = \frac{N_{detected}(R^2, Z)}{N_{generated}(R^2, Z)} \quad (4.4)$$

In this way we can calculate the map of the variations of LCE inside the LS.

In our first investigation, LCE simulations are the combination of three defined thicknesses of the veto vessel (40 to 60 cm) and the addition of 0, 80, 96 or 120 PMTs along with the existing muon veto ones and with the implementation of only one reflective foil on the inner acrylic surface of the LS in contact with the "displacer". The PMTs configuration chosen is the Model 1 in Fig. 3.12 consisting of a cylindrical array of a certain number of columns (adapted accordingly to the total number of PMTs), and a fixed number of 8 rows covering most of the height of the veto along the vertical axis. PMTs are placed only on the side of the vessels and a distance of 70 cm has been set between the PMTs faces and the outer acrylic walls, to shield the LS from the background coming from U, Th and K contamination of the PMT itself. The final efficiency calculations are listed in Table 4.2 and examples of the LCE maps derived in this investigation are shown in Fig. 4.5 for a veto thickness of 60 cm.

Thickness LS	LCE [%]			
	no extra PMTs	80 extra PMTs	96 extra PMTs	120 extra PMTs
40 cm	1.23	4.73	5.36	6.21
50 cm	1.24	4.53	5.13	5.92
60 cm	1.27	4.33	4.89	5.69

TABLE 4.2: LCE as a function of the veto thickness and the number of side veto PMTs (Model 1).

As one can see from Table 4.2, for the configuration with no extra PMTs (it means that only the ones already present in the water tank are used), the LCE over the full volume increases for increasing thickness. It is reasonable since the distance from the center of mass of the individual vessels to the water tank walls decreases. On the other side, light collection is higher for decreasing thicknesses, since the solid angle covered by photodetectors increases.

A second study has been carried out comparing the LCE of the three models with a fixed number of 120 total PMTs, and for a thickness of LS of 60 cm in the *ideal* geometry, by varying the number of the reflective foils. In this configuration, Model 1 consisting of 15 columns and 8 rows satisfying the condition of 85% vertical coverage; in Model 2 and Model 3, PMTs are disposed using 6 x 5 matrix on the lateral faces of the box and 4 x 5 matrix on all the faces of the box, respectively. Model 2 represents the possibility to

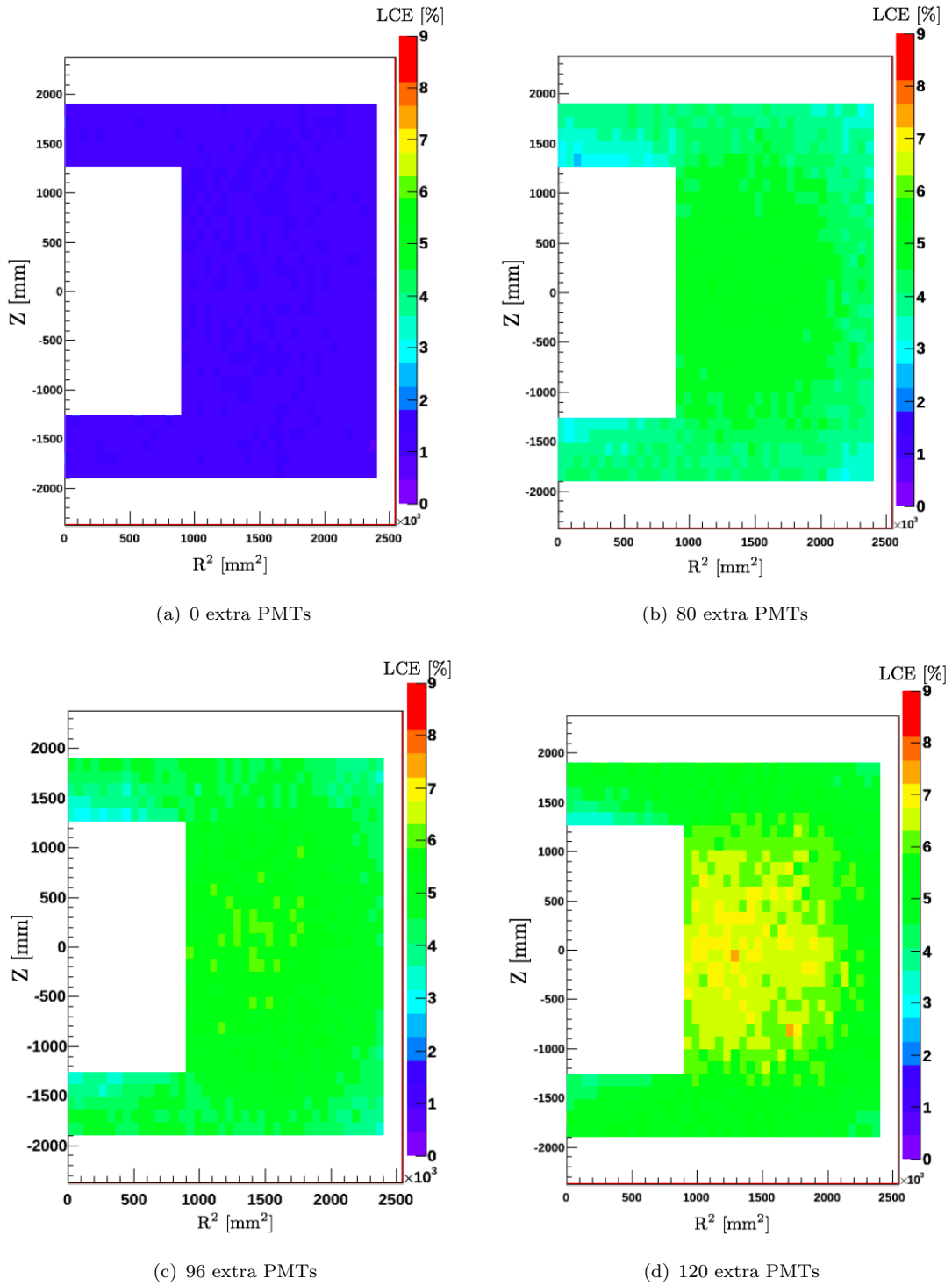


FIGURE 4.5: LCE maps for a veto 60 cm thick in the cylindrical PMT array configuration (Model 1) with one reflective foil.

enclose the neutron veto PMTs in a box fitting the dimensions of the existing support structure.

Results for the averaged LCE in the LS volume for all the inspected models in this study are presented in Table 4.3.

	LCE [%]		
	Model 1	Model 2	Model 3
0 reflector	3.80	3.79	4.25
1 reflector	5.69	5.71	6.37
2 reflectors	7.76	8.16	8.45

TABLE 4.3: LCE as a function of the number of the reflective foils in all the models, for a fixed number of 120 PMTs. In the case of one reflective foil, it is placed on the inner acrylic surface of the LS in contact with the "diplacer"; for a double reflector, we have cladded also the inner surface of the structure containing the PMTs.

In Fig. 4.6 the LCE maps are shown in the cases of one, two or none reflective foils for the Model 2 and Model 3 for a direct comparison.

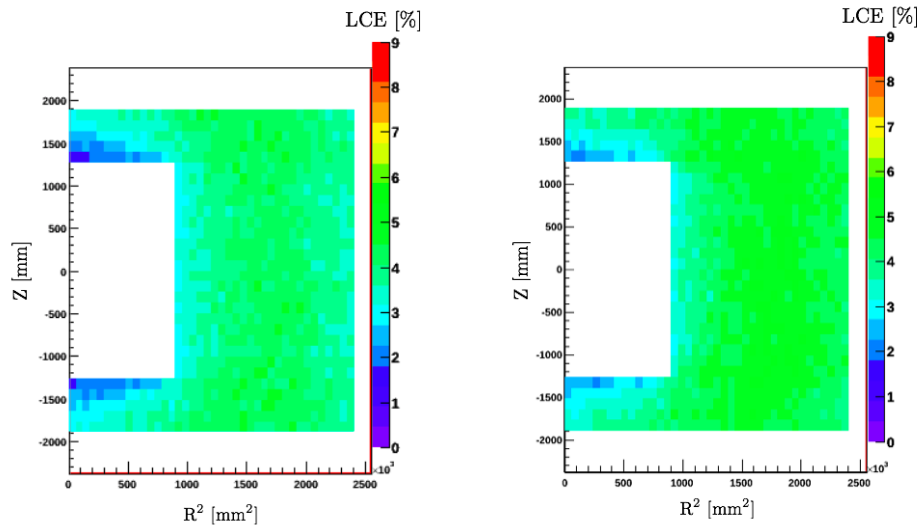
These results indicate that:

- For a fixed geometry of the PMTs array, the LCE increase with the total number of PMTs implemented.
- For a fixed number of PMTs, LCE does not depend on their positioning. Indeed, the cylindrical (Model 1) and box (Model 2) configuration present the same values of LCE. In addition, it was verified that top/bottom PMTs arrays do not improve LCE significantly.
- The best contribution to the efficiency is given by the reflective foils: adding one reflective foil increases the LCE of about 50% in all the configuration shown in Table 4.3 and with two reflectors the LCE doubles.

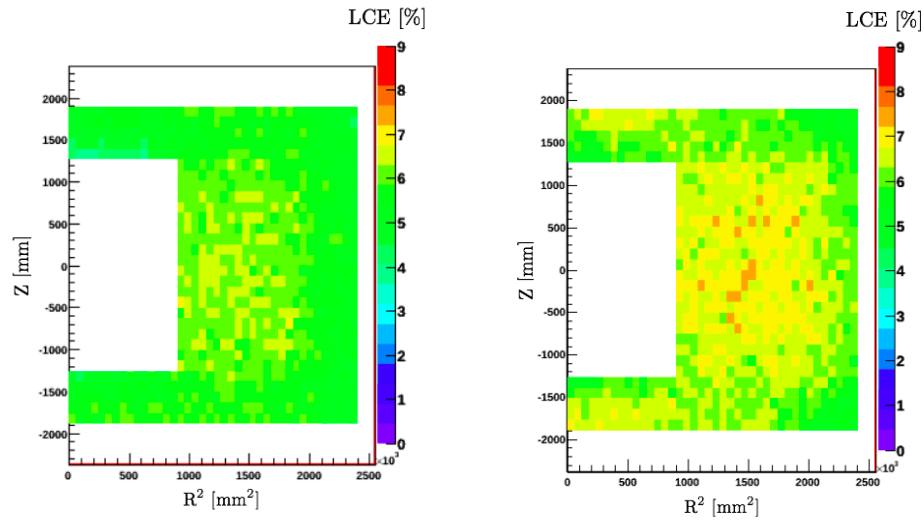
Finally, we have studied the LCE for the *modular* option of the veto system, Fig. 3.13. Four PMTs in each box have been implemented, at a distance from LS vessel of 70 cm and by cladding the inner surface of the box with a reflective foil. In each box the mean value of LCE results to be 6.10%.

4.3 Veto system performance

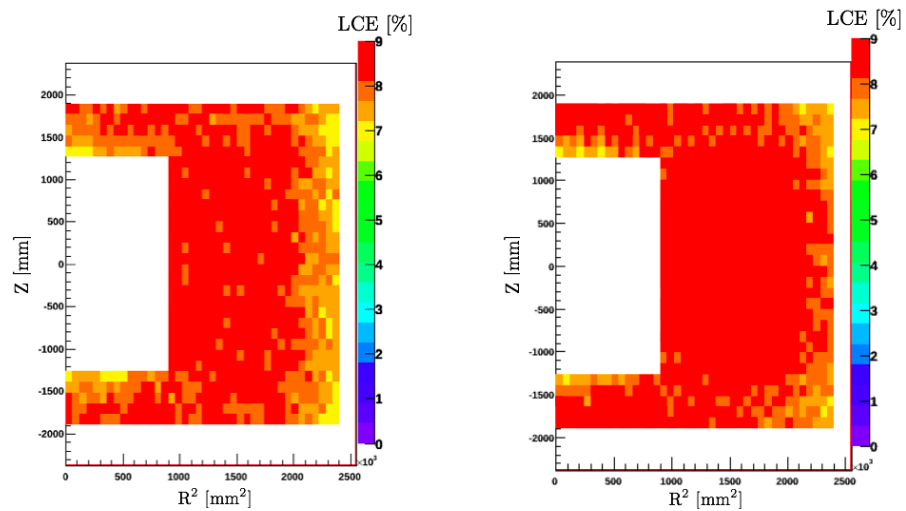
In this section, the response of the three neutron veto configurations is studied. These configurations are:



(a) 0 reflector



(b) 1 reflector



(c) 2 reflectors

FIGURE 4.6: LCE maps for a veto 60 cm thick, a fixed number of 120 PMTs as in Model 2 (left) and Model 3 (right) varying the number of reflective foils.

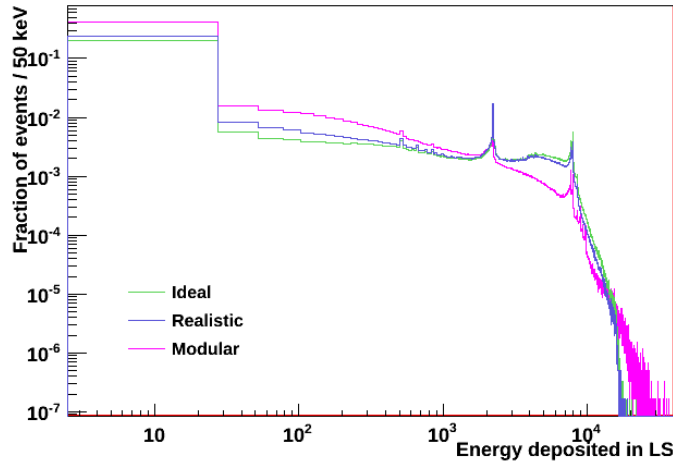


FIGURE 4.7: Energy spectra for the three geometries with foam as displacer.

	% of events depositing energy			
	> 50 keV	> 100 keV	> 200 keV	> 400 keV
Vacuum	91.66	90.85	89.73	88.10
Foam	91.33	90.61	89.26	87.59
Water	67.81	65.60	61.04	55.58

TABLE 4.4: Percentages of background events depositing energy in the LS volume for the different displacer materials for the *ideal* option.

- *Ideal* option for 60 cm thickness of LS and different displacer materials;
- *Realistic* option for 60 cm thickness of LS and foam as displacer;
- *Modular* option for a 60 cm box of LS and foam as displacer;

In this analysis, 10^7 neutrons were generated from TPC PMTs. The results were filtered using the selection criteria described in 3.2.1 to identify the background (WIMP-like events).

The distributions of the energy deposits in LS for these configurations are shown in Fig. 4.7. For a better understanding of the performances of different veto configurations, the percentages of detected events with respect to the total number of events depositing some threshold energies in the LS volume have been calculated. The results are summarized in Table 4.4 for the *ideal* option and in Table 4.5 for the *realistic* and *modular* ones.

These results do not account for the time in which the threshold deposits are produced, although they give an insight into the expected performance of the veto. For the high amount of analyzed statistics, it has been decided to process the energy deposit without fixing an acquisition time window.

	% of events depositing energy			
	> 50 keV	> 100 keV	> 200 keV	> 400 keV
Realistic	86.25	85.14	83.30	81.04
Modular	70.59	67.88	63.77	58.35

TABLE 4.5: Percentages of background events depositing energy in the LS volume for the *realistic* and *modular* option with foam as displacer.

	% of neutron captures		
	Vacuum	Foam	Water
LS	75.3	73.6	20.89
(Gd)	(65.6)	(64.4)	(18.66)
(H)	(9.5)	(8.9)	(2.18)
Cryostat	18.5	18.9	27.28
Acrylic	6.1	6.6	5.2
Displacer	0	0.7	46.44
Water	0.1	0.2	<0.001

TABLE 4.6: Percentages of the neutron captures as a function of the displacer material in every volume for the *ideal* option.

	% of neutron captures	
	Realistic	Modular
LS	66.5	44.2
(Gd)	(58.6)	(39.1)
(H)	(7.6)	(4.9)
Cryostat	18.2	30.8
Acrylic	6.6	6.2
Displacer	1.9	1.2
Water	6.8	17.6

TABLE 4.7: Percentages of the neutron captures as a function of the displacer material in every volume for the *realistic* and *modular* option with foam as displacer.

Therefore, by setting some specific flags in the simulations, one can compute the amount of captures that take place in every volume. The results obtained are summarized in Table 4.6 for the *ideal* option and in Table 4.7 for the other ones.

As reported the water is not a suitable displacer since background neutrons are captured there before reaching the LS veto. For the ideal and realistic option the performances are quite similar: with the realistic option we lose about 7% of neutron captures in LS with respect to the ideal one; on the other hand, neutron captures in other volumes do not vary except the ones in the displacer: this is due to the structure of the realistic option, in which the amount of foam in the displacer would be greater (see Fig. 3.7).

The modular option shows the worst performances. Indeed, in this option the amount of LS is smaller than the others and the neutron is forced to cross several materials before reaching it. In particular, there are several capture on steel of the cryostat and of the

box, in which the LS and PMTs are placed. Also the percentage of captures inside the water increase due to the spaces between the veto modules.

4.3.1 Photoelectron Yield

The number of detected PEs or “PE yield” can be calculated by rescaling the light yield (LY) with the light collection efficiency (LCE of the LS), the quantum efficiency (QE) and collection efficiency (CE) of the PMTs:

$$PE_y(R^2, Z) = LCE(R^2, Z) \cdot CE \cdot QE \cdot LY \quad (4.5)$$

In the case of the *ideal* and *realistic* option, during the simulation the PE yield has been evaluated for each of the individual tracks in LS following these steps:

- The average number of photons produced in each interaction (i.e. in each energy deposit) in LS is calculated as:

$$\langle N_{ph} \rangle = E_d \cdot LY \quad (4.6)$$

- Associating Gaussian statistical fluctuation in the light emitted, the number of photons emitted in each step is

$$N_{ph} = \text{Gauss}(\langle N_{ph} \rangle, \sqrt{\langle N_{ph} \rangle}) \quad (4.7)$$

- Photons are converted into signal, i.e. photoelectrons (PE), by applying the position-dependent light collection efficiency $LCE(R^2, Z)$ from section 4.2.

$$f_{PE}(R^2, Z) = LCE(R^2, Z) \cdot CE \cdot QE \quad (4.8)$$

- Finally, to obtain the detected PEs there is a binomial process involved, to properly consider also the statistical fluctuations:

$$N_{PE} = \text{Binomial}(N_{ph}, f_{PE}(R^2, Z)) \quad (4.9)$$

For the modular option, the PE yield has been calculated according to the equation 4.5 but using the average value of LCE in this configuration, that is 6.10%.

In this study, other reference values are:

- $LY = 9000$ photons/MeV;

- $QE = 30\%$;
- $CE = 85\%$;

For example according to Equation 4.5, the mean PE yield in the scintillator volume for the ideal and realistic option is ~ 178 PE/MeV, taking into account a mean LCE of 7.76%. For the modular option an average value of 6.10% LCE yields ~ 140 PE/MeV. Fig. 4.8 shows the PE yield for the three studied veto arrangements.

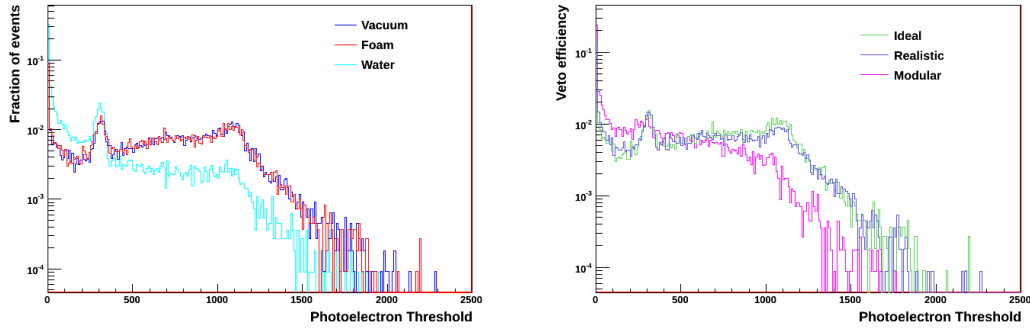


FIGURE 4.8: PE yield distribution in the LS for NR background events of the ideal option as a function of the displacer materials (left) and of the three options all together (right).

Trends for different material displacers and for the three geometries configuration are the same as before. As shown in figure after statistical treatment on the energy conversion, the PE spectra are smeared out with respect to the simulated energy spectra, with the peak equivalent to ~ 2.2 MeV still visible.

4.4 Neutron veto efficiency

The veto efficiency can be described as the ability to tag background events that have deposited energy within the LXe target, such that they would otherwise satisfy the WIMP search criteria. A series of simulations were performed to assess the vetos tagging efficiency for certain signal sizes, i.e. PEs thresholds or energy deposited as well.

Fig. 4.9 (left) represents the efficiency variation as a function of the energy thresholds and for different scintillator thicknesses in the ideal option. Increasing the veto thickness from 40 cm up to 80 cm the improvement on the efficiency is $\sim 1-2\%$ every 10 cm. This analysis has been done for the energy deposits by ER as a first approach. Then we have studied the impact of the quenched NR component in the efficiency. Considering also the energy deposits by NRs with respect to the case of ERs only, Fig. 4.9 (right), the

efficiency improves of about 3% at 50 keV, and at higher energy it keeps constant with a variation of about 2%.

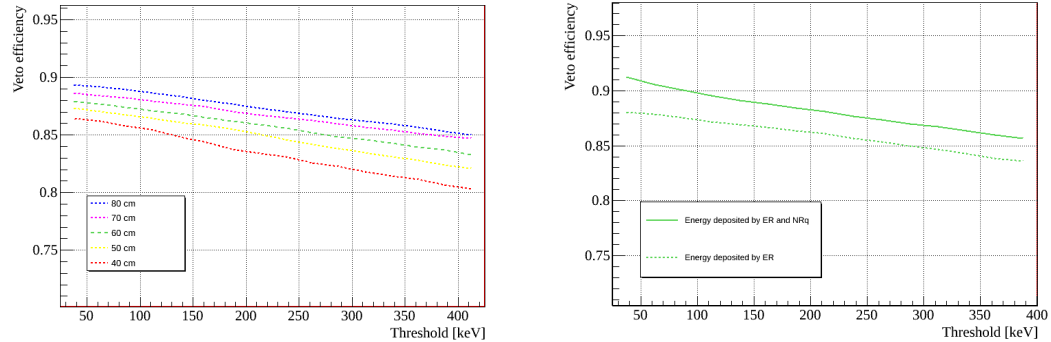


FIGURE 4.9: The tagging efficiency as a function of ER energy deposits for several thickness of LS in the ideal option (left). The tagging efficiency for 60 cm thickness of LS in the ideal option for energy deposited by ER and with the contribution of NRs quenched (right).

The final impact of replacing the foam or vacuum with water is shown in Fig. 4.10; using water the efficiency is considerable lower than the ones obtained with other displacers.

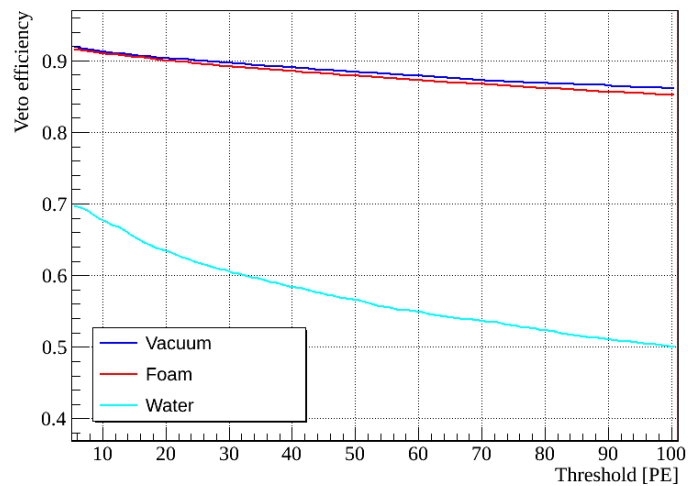


FIGURE 4.10: Veto efficiency for the ideal option varying displacer materials.

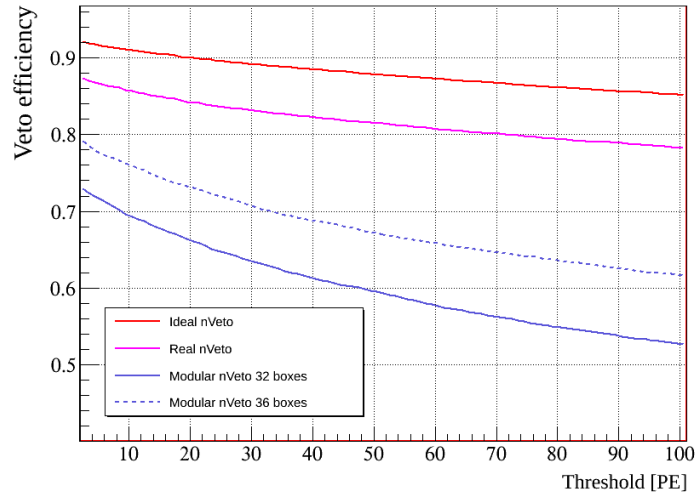


FIGURE 4.11: Veto efficiency for the *ideal*, *realistic* and modular option (with 32 or 36 boxes) of the LS.

Finally, Fig. 4.11 reports the comparison between the tagging efficiency for the baseline configurations presented in section 4.3.1 for the three geometric options of the LS as a function of PE thresholds. In the figure we have also added the modular option in the case of 36 boxes: the four additional boxes with respect to the original configuration are placed just under the displacer, right below the outer cryostat. For a fixed geometry, the efficiency varies very little with the threshold. For a fixed value of the threshold, the loss of efficiency due to the removal of the upper and lower caps of the ideal configuration, is $\sim 5\%$. We have also studied the possibility to remove only the upper cap, leaving the bottom one, and the result is that we have an efficiency loss of about 3% with respect to the ideal option.

On the other hand, the modular option shows a tagging efficiency improvement of about 7% when we arrange the LS volume also on the bottom part of the cryostat. The values of efficiency for various PE thresholds are summarize in Table 4.8.

	% tagging efficiency			
	8 PE	16 PE	32 PE	64 PE
Ideal	91.26	90.44	89.05	87.05
Realistic	86.13	84.76	82.98	80.44
Modular(32)	70.62	67.61	63.18	57.19
Modular(36)	76.92	74.29	70.28	65.40

TABLE 4.8: Tagging efficiency for the *ideal*, *realistic* and the 36-boxes *modular* option.

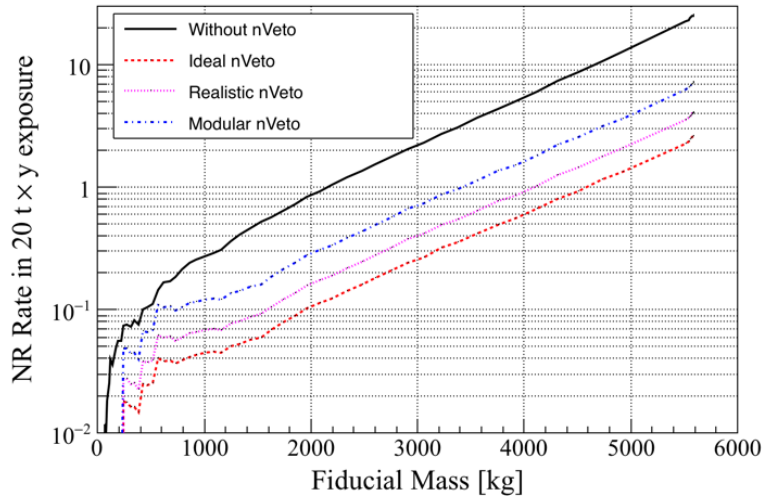


FIGURE 4.12: NR background rate from radiogenic neutrons as a function of the fiducial mass for a LS veto 60 cm thick in the ideal and realistic option and for the 36-boxes modular option. In all the geometries the foam has been chosen as displacer. Solid back line represents the NR background without neutron veto.

4.5 NR Background prediction for XENONnT

As we have seen in section 3.2.2, without a neutron veto system the XENONnT NR radiogenic background rate prediction is 1.1 ev/y in 4 t FV.

In this section we rescale those results, applying the tagging efficiency of the neutron veto system. For a threshold of 32 PE, that corresponds to an energy deposit of about 200 keV in the LS, for the three best configurations obtained, the corresponding efficiencies are:

- 89% for the ideal option in the configuration with a 60 cm thick of LS, foam as displacer, two reflective foils and 120 PMTs;
- 83% for the realistic option with a 60 cm thick of LS, foam as displacer, two reflective foils and 120 PMTs;
- 70% for the modular option with 36 boxes, with one reflective foil and four PMTs for each box, and with foam as displacer;

The results of this evaluation for the total exposure of 20 t·y are shown in Fig. 4.12. The result for the ideal and realistic options is in full agreement with the background goal of the XENONnT experiment, which is < 1 background event in the total exposure of 20 ton-year, while for the modular one this goal is not yet fully achieved, at least in the particular design we have considered so far.

Conclusions

The composition of the Universe is today one of the most challenging open questions in physics. Despite the scientific achievement of the last decades in the astrophysical and cosmological fields, the majority of the Universe energy content is still unknown. Experimental results, based both on the direct and indirect detection of Dark Matter have not yet confirmed any positive signal from such a kind of matter. Due to the very small cross section for WIMP interactions, the number of expected events is very small (~ 1 ev/tonne/year), thus requiring detectors with large target mass and low background level. The use of double phase, LXe/GXe, TPC represents one of the most promising techniques for this kind of search.

XENON1T, currently in data acquisition at LNGS, is the first tonne scale LXe-based detector, its aim is to detect a WIMP-nucleon interaction. At the time of this thesis, XENON1T has derived the most stringent exclusion limits on the spin-independent WIMP-nucleon interaction cross section for WIMP masses above $10 \text{ GeV}/c^2$, with a minimum of $7.7 \times 10^{-47} \text{ cm}^2$ for $35\text{-GeV}/c^2$ WIMPs at 90% confidence level. These first results demonstrate that XENON1T has the lowest low-energy background level ever achieved by a dark matter experiment. In the full nominal 2 t·y exposure, the expected sensitivity is $1.6 \cdot 10^{-47} \text{ cm}^2$.

The future upgrade of the experiment, named XENONnT, is already under study by the collaboration. It will be conceptually identical to XENON1T but with a larger TPC and increased xenon target (~ 6 t), and additional PMTs. All the other sub-systems of the XENON1T experiment, in particular all the LXe handling systems, the detector support structure as well as the outer cryostat, have been already designed for a LXe mass up to 8 t.

In the context of this upgrade, radiogenic nuclear recoil background studies turned out to be crucial in order to effectively define the conditions for the dark matter search operation of the detector. Indeed the expected neutron background for the new designed Time Projection Chamber is ~ 5 events in the 4t fiducial volume in the nominal 20 ton-year exposure. With the goal to decrease the radiogenic neutron background and

optimize the liquid xenon fiducial volume in XENONnT, we studied the performances of a gadolinium-doped liquid scintillator neutron veto.

The veto for the XENONnT detector has been simulated using GEANT4 software. The simulation was used extensively throughout the veto design process, to test geometry, and to guide design decisions such as PMT positioning and number, or the possibility to use reflective foils. The Monte Carlo has provided the means to tune the design to maximise the neutron tagging efficiency. The veto Monte Carlo has subsequently been used to calculate the overall efficiency of the veto for neutron background rejection.

One of the main mechanical challenges for the realization of this neutron veto lies on the ability to fill the buffer between the cryostat and the acrylic liquid scintillator vessels. The most realistic options, are represented by a low-density foam and the water. This latter possibility shows two main disadvantages: first, it results in a decrease of the tagging efficiency of the veto, due to the fact that captures happens mostly inside this water volume; second the presence of a water buffer could also endanger the pressure stability of the acrylic containers, depending on the complexity of the designed geometry.

Simulations to derive the photoelectron yield of the veto outer detector have been also carried out, pointing to the necessity of adding a new array of photomultiplier tubes, placed closer to the detector cryostat with respect to the currently ones of the Muon Veto.

Results indicate that, for a scintillating mixture with 0.1% of gadolinium by weight, and a light collection efficiency of $\sim 7\%$, the veto will reject neutrons that otherwise would meet the WIMP search criteria with an efficiency larger than 80% for a veto threshold of 32 PE. This has been verified for a veto cylindrical structure around the XENONnT outer cryostat and with foam as displacer. On the other hand, when we consider a modular geometry of 36 identical boxes the efficiency decrease up to a 10% with respect the cylindrical one. This behaviour is very similar to that results when we use water as displacer material in the cylindrical configuration.

To conclude, a neutron rejection factor higher than 80% reduces the neutron background by a factor 4-5 with respect to the prediction. This would be in full agreement with the background goal of the XENONnT experiment, which is < 1 background event in the total exposure of 20 ton·year.

Bibliography

- [1] F. Zwicky. The coma cluster of galaxies. *Publications of the Astronomical Society of the Pacific*, pages 61–71, 1951.
- [2] R. H. Sanders K. G. Begeman, A. H. Broeils. Extended rotation curves of spiral galaxies: Dark haloes and modified dynamics. *Monthly Notices of the Royal Astronomical Society*, 249(3):523–537, 1991.
- [3] C. Alcock et al. The macho project: microlensing results from 5.7 years of large magellanic cloud observations. *The Astrophysical Journal*, 542(1):281, 2000.
- [4] M. Markevitch D. Clowe, A. Gonzalez. Weak lensing mass reconstruction of the interacting cluster 1E0657-558: Direct evidence for the existence of dark matter. *The Astrophysical Journal*, 604(2):596, 2004.
- [5] R.W. Wilson A.A. Penzias. A measurement of excess antenna temperature at 4080 mc/s. *The Astrophysical Journal*, 142:419–421, 1965.
- [6] P. A. R. Ade et al. Planck 2013 results. xv. cmb power spectra and likelihood. *Astronomy & Astrophysics*, 571:A15, 2014.
- [7] C. L. Bennett et al. Nine-year wilkinson microwave anisotropy probe (wmap) observations: final maps and results. *The Astrophysical Journal Supplement Series*, 208(2):20, 2013.
- [8] A.R. Liddle O. Lahav. The Cosmological Parameters 2014. *Review of Particle Data Group*, 2014.
- [9] W. de Boer et al. Egret excess of diffuse galactic gamma rays interpreted as a signal of dark matter annihilation. *arXiv preprint astro-ph/0602325*, 2006.
- [10] P. J. Peebles A. M. Ostriker. A numerical study of the stability of flattened galaxies: or, can cold galaxies survive? *The Astrophysical Journal*, 186:467–480, 1973.
- [11] H. R. Quinn R. D. Peccei. Cp conservation in the presence of pseudoparticles. *Physical Review Letters*, 38(25):1440, 1977.

-
- [12] M. S. Turner. Cosmic and local mass density of "invisible" axions. *Physical Review D*, 33(4):889, 1986.
- [13] Mourad Tamazouzt. The primakoff effect at high energy. *Physics Letters B, Volume 211, Issue 4, p. 477-480*, 112(091303), 1988.
- [14] K. Zioutas et al. First results from the cern axion solar telescope. *Physical review letters*, 94(12):121301, 2005.
- [15] E. Zavattini et al. New pvlas results and limits on magnetically induced optical rotation and ellipticity in vacuum. *Physical Review D*, 77(3):032006, 2008.
- [16] E. Aprile et al. (XENON Collaboration). First axion results from the xenon100 experiment. *Physical Review D*, 90(6):062009, 2014.
- [17] K. Griest G. Jungman, M. Kamionkowski. Supersymmetric dark matter. *Physics Reports*, 267(5):195–373, 1996.
- [18] P. Gondolo. Phenomenological introduction to direct dark matter detection. *arXiv preprint hep-ph/9605290*, 1996.
- [19] E. Witten M. W. Goodman. Detectability of certain dark-matter candidates. *Physical Review D*, 31(12):3059, 1985.
- [20] M. Yamaguchi T. Moroi, H. Murayama. Cosmological constraints on the light stable gravitino. *Physics Letters B*, 303(3):289–294, 1993.
- [21] A. Vilenkin V. Berezhinsky, M. Kachelriess. Ultrahigh energy cosmic rays without greisen-zatsepin-kuzmin cutoff. *Physical Review Letters*, 79(22):4302, 1997.
- [22] E. Aprile et al. (XENON100). Dark matter results from 225 live days of xenon100 data. *Phys. Rev. Lett.*, 109(181301), 2012.
- [23] D. S. Akerib et al. (LUX Collaboration). First results from the lux dark matter experiment at the sanford underground research facility. *Phys. Rev. Lett.*, 112(091303), 2014.
- [24] D. Akerib et al. (LUX Collaboration). Results from a search for dark matter in the complete lux exposure. *arXiv.org*, 118(2), 2017.
- [25] E. Aprile et al. (XENON Collaboration). First dark matter search results from the xenon1t experiment. *arXiv:1705.06655*, 2017.
- [26] F. Agostini. Caratterizzazione e calibrazione dei fotomoltiplicatori del sistema di veto di muoni per l'esperimento xenon1t. Master's thesis, Alma Mater Studiorum - University of Bologna, 2013.

-
- [27] R. Bernabei et al. The annual modulation signature for dark matter: Dama/libra-phase1 results and perspectives. *Advances in High Energy Physics*, 2014, 2014.
- [28] K. Blum. Dama vs. the annually modulated muon background. *arXiv preprint arXiv:1110.0857*, 2011.
- [29] R. Bernabei et al. No role for muons in the dama annual modulation results. *European Physical Journal C-Particles and Fields*, 72(7):1, 2012.
- [30] A. Pierce N. Weiner I. Yavin S. Chang, J. Liu. Cogent interpretations. *Journal of Cosmology and Astroparticle Physics*, 2010(08):018, 2010.
- [31] E. Armengaud et al. Search for low-mass wimps with edelweiss-ii heat-and-ionization detectors. *Physical Review D*, 86(5):051701, 2012.
- [32] R. Agnese et al. Improved wimp-search reach of the cdms ii germanium data. *Physical review letters*, 92, 2015.
- [33] G. Angloher and al. Results on light dark matter particles with a low-threshold cresst-ii detector. *The European Physical Journal C*, 76(1):25, 2016.
- [34] G. Angloher et al. Results on low mass wimps using an upgraded cresst-ii detector. *The European Physical Journal C*, 74(12):1–6, 2014.
- [35] R. Agnese et al. Silicon detector dark matter results from the final exposure of cdms ii. *Physical Review Letters*, 111(25):251301, 2013.
- [36] C. E. Aalseth et al. Cogent: A search for low-mass dark matter using p-type point contact germanium detectors. *Physical Review D*, 88(1):012002, 2013.
- [37] A. Gütlein. Feasibility study for a first observation of coherent neutrino nucleus scattering using low-temperature detectors. Master’s thesis, Technische Universität München.
- [38] P. Agnes et al. (DarkSide Collaboration). Results from the first use of low radioactivity argon in a dark matter search. *arXiv:1510.00702*, 2016.
- [39] C. E. Aalseth et al. The darkside multiton detector for the direct dark matter search. *Advances in High Energy Physics*, 2015(541362), 2015.
- [40] E. Aprile et al. (XENON collaboration). Physics reach of the xenon1t dark matter experiment. *JCAP04(2016)027*, 2016.
- [41] E. Aliu et al. Veritas deep observations of the dwarf spheroidal galaxy segue 1. *arXiv preprint arXiv:1202.2144*, 2012.

- [42] K. Choi and al. (Super-Kamiokande Collaboration). Search for neutrinos from annihilation of captured low-mass dark matter particles in the sun by super-kamiokande. *arXiv:1503.04858v1*, 2015.
- [43] S. Ritz P. F. Michelson, W. B. Atwood. Fermi gamma-ray space telescope: High-energy results from the first year. *Rept. Prog. Phys.*, 2010.
- [44] Z. Ahmed et al. Results from a low-energy analysis of the cdms ii germanium data. *Physical Review Letters*, 106(13):131302, 2011.
- [45] S.C. Park C. Rott, K. Kohri. Superheavy dark matter and icecube neutrino signals: bounds on decaying dark matter. *arXiv preprint arXiv:1408.4575*, 2014.
- [46] R. Abbasi et al. Search for dark matter from the galactic halo with the icecube neutrino telescope. *Physical Review D*, 84(2):022004, 2011.
- [47] M. Aguilar et al. Electron and positron fluxes in primary cosmic rays measured with the alpha magnetic spectrometer on the international space station. *Physical review letters*, 113(12):121102, 2014.
- [48] O. Adriani et al. Pamela results on the cosmic-ray antiproton flux from 60 mev to 180 gev in kinetic energy. *Physical Review Letters*, 105(12):121101, 2010.
- [49] T. Gong Q.H. Cao, C.R. Chen. Leptophilic dark matter and ams-02 cosmic-ray positron flux. *arXiv preprint arXiv:1409.7317*, 2014.
- [50] E. Aprile et al. (XENON Collaboration). Design and performance of the xenon10 dark matter experiment. *Astroparticle Physics*, 34(9):679–698, 2011.
- [51] E. Aprile et al.(XENON Collaboration). The xenon100 dark matter experiment. *Astroparticle Physics*, 35(9):573–590, 2012.
- [52] E. Aprile et al. (XENON Collaboration). The xenon1t dark matter search experiment. In *Sources and Detection of Dark Matter and Dark Energy in the Universe*, pages 93–96. Springer, 2013.
- [53] T. Doke E. Aprile. Liquid xenon detectors for particle physics and astrophysics. *Reviews of Modern Physics*, 82(3):2053, 2010.
- [54] P. Majewski K. Ni M. Yamashita E. Aprile, K.L. Giboni. Observation of anticorrelation between scintillation and ionization for mev gamma rays in liquid xenon. *Physical Review B*, 76(1):014115, 2007.
- [55] J. Angle et al. First results from the xenon10 dark matter experiment at the gran sasso national laboratory. *Physical Review Letters*, 100(2):021303, 2008.

-
- [56] D. S. Akerib et al. Limits on spin-independent interactions of weakly interacting massive particles with nucleons from the two-tower run of the cryogenic dark matter search. *Physical review letters*, 96(1):011302, 2006.
- [57] J. Angle et al. Limits on spin-dependent wimp-nucleon cross sections from the xenon10 experiment. *Physical review letters*, 101(9):091301, 2008.
- [58] A. Fowlie et al. Constrained mssm favoring new territories: The impact of new lhc limits and a 125 gev higgs boson. *Physical Review D*, 86(7):075010, 2012.
- [59] Z. Ahmed et al. Search for weakly interacting massive particles with the first five-tower data from the cryogenic dark matter search at the soudan underground laboratory. *Phys. Rev. Lett.*, 102(011301):0802–3530, 2009.
- [60] D. Akimov et al. Wimp-nucleon cross-section results from the second science run of zeplin-iii. *Physics Letters B*, 709(1):14–20, 2012.
- [61] E. Aprile et al. (Xenon Collaboration). Xenon100 dark matter results from a combination of 477 live days. *Phys. Rev. D* 94, 122001 (2016), 2016.
- [62] E. Aprile et al. (Xenon Collaboration). Conceptual design and simulation of a water cherenkov muon veto for the xenon1t experiment. *JINST* 9, P11006 (2014), 2014.
- [63] E. Aprile et al. (Xenon Collaboration). Xenon1t at lngs. *Proposal April*, 2010.
- [64] G. Plante. The xenonnt project. In *Dark Matter 2016 - UCLA - February 19, 2016*, 2016.
- [65] The Geant4 Collaboration. Geant4 user’s guide for application developers. version: geant4 9.6.0, 2012.
- [66] Y. Ding S. Hans K. M. Heeger L. Hu et al. W. Beriguete, J. Cao. Production of a gadolinium-loaded liquid scintillator for the daya bay reactor neutrino experiment. *Nuclear Instruments and Methods in Physics Research*, A(763):82–88, 2014.
- [67] I. S. Yeo W. Q. Choi J. K. Ahn J. H. Choi et al. J. S. Park, J. Lee. Production and optical properties of gd-loaded liquid scintillator for the reno neutrino detector. *Nuclear Instruments and Methods in Physics Research*, A(707):45–53, 2013.
- [68] M. Apollonio et al. Search for neutrino oscillations on a long base-line at the chooz nuclear power station. *arXiv:hep-ex/0301017*, 2003.
- [69] V. M. Novikov A. G. Piepke, S. W. Moser. Development of a gd loaded liquid scintillator for electron anti-neutrino spectroscopy. *arXiv:nucl-ex/9904002*, 1999.
- [70] G. Horton-Smith. Additional gadolinium support for glg4sim.

- [71] Hamamatsu Photonics K.K. Hamamatsu official site.
- [72] J. B. Birks. Scintillations from organic crystals: specific fluorescence and relative response to different radiations. *Proc. Phys. Soc.*, A(64):874, 1951.